Universidad
Carlos III de Madrid
www.uc3m.es

TESIS DOCTORAL

Advances in Navigation and Intraoperative Imaging for Intraoperative Electron Radiotherapy

Autor:

Verónica García Vázquez

Director/es:

Javier Pascau González-Garzón

Tutor:

Javier Pascau González-Garzón

DEPARTAMENTO DE BIOINGENIERÍA E INGENIERÍA AEROESPACIAL

Leganés, enero de 2017

Universidad Carlos III de Madrid
www.uc3m.es

TESIS DOCTORAL

Advances in Navigation and Intraoperative Imaging for Intraoperative Electron Radiotherapy

Autor: *Verónica García Vázquez*

Director/es: Javier Pascau González-Garzón

Firma del Tribunal Calificador:

Firma

Presidente: Joaquín López Herraiz

Vocal: Óscar Acosta Tamayo

Secretario: María Arrate Muñoz Barrutia

Calificación:

Leganés, 20 de enero de 2017

Lucha de gigantes convierte
el aire en gas natural.
Un duelo salvaje advierte
lo cerca que ando de entrar.
En un mundo descomunal,
siento mi fragilidad.
Vaya pesadilla corriendo
con una bestia detrás.
Dime que es mentira todo,
un sueño tonto y no más.
Me da miedo la enormidad,
donde nadie oye mi voz.
Deja de engañar,
no quieras ocultar
que has pasado sin tropezar.
Monstruo de papel,
no sé contra quién voy,
¿o es que acaso hay alguien más aquí?
Creo en los fantasmas terribles
de algún extraño lugar
y en mis tonterías para
hacer tu risa estallar.
En un mundo descomunal,
siento tu fragilidad.
Deja de engañar,
no quieras ocultar
que has pasado sin tropezar.
Monstruo de papel,
no sé contra quién voy.
¿O es que acaso hay alguien más aquí?
Deja que pasemos
sin miedo.

Lucha de gigantes. Antonio Vega
(versión de IZAL)

AGRADECIMIENTOS

Al final todo se puede conseguir… con el esfuerzo de uno mismo y, áun más importante, con el gran apoyo de los demás. Esta tesis no hubiera sido posible si no hubiera estado detrás un gran equipo que va haciendo con sus grandes aportaciones que cada día esté más cerca el que se pueda planificar y registrar el tratamiento de radioterapia intraoperatoria (RIO) con electrones. Además, ha sido también crucial el resto de personas que, aunque no trabajen directamente en este tema, te aportan sus ideas, sus preguntas, su tiempo y/o su gran cariño.

Primero querría agradecer a Javi (Pascau) su gran paciencia conmigo, consejos, correcciones, y la oportunidad que siempre nos brinda de crecer profesionalmente y de poder cacharrear con la última tecnología que hay en el mercado. Esto nos permite que no nos estanquemos nunca y que abramos más la mente. Gracias a que tú creías en esta tesis, al final se ha hecho realidad.

Ese gran equipo que existe en radioterapia intraoperatoria lo encabeza el Dr. Calvo con su enorme ilusión por mejorar y divulgar la RIO. Me gustaría resaltar al Dr. Santos, una persona con ideas muy brillantes que vamos poco a poco incorporando a la línea de investigación de la RIO y también con una alegría que contagiaba a todos. Mencionar al resto de oncólogos radioterápicos (Dr. Miguel Ángel Lozano, Dra. Ana Álvarez, Dra. Marina Gómez, Dra. Ana Calín, Dr. Javier Serrano, Dra. Carmen González, Dr. Eduardo Alvarado [juntos seguimos otra religión…], Dr. Claudio Sole, Dra. Mercedes Muñoz…), cirujanos (Dr. Calvo Haro, Dr. Pérez [dos mentes muy inquietas], Dr. Asencio, Dr. Cuervo, Dr. García Sabrido…), radiofísicos (Miguel Ángel, Ramón, Cristina, Rafa, Susana, Rocío, Rosa…), anestesistas, técnicos de radioterapia (Elena, Juan Antonio, Beatriz, Sandra, Patricia, Ana, Paco, Pilar, Sara, Jorge, Paloma…), el jefe de enfermería (Emilio), enfermeras (Amelia, Lourdes, Feli, Fany…), las secres (Concha y Carmen) y Rosa que aportan su experiencia, consejos y paciencia, y nos dejan poder probar nuestros aparatos dentro del quirófano o en el TAC simulador del Marañón. En la parte técnica relacionada con investigación, mucha gente ha aportado su granazo de arena: Javi, que con sus proyectos de investigación e ideas ha dado continuidad a lo que hacemos, Manolo con sus acertadas sugerencias y Eu

desde el LIM; Chus, Andrés, Pedro, Laura, Subhra, Juan Enrique… desde Teleco de la Politécnica; José Manuel, Joaquín, Elena, Paula… desde Físicas de la Complutense. También la empresa GMV y más concretamente a Carlos, al dios Manlio, Samuel, Raúl y Marta. Gracias a la gente que he ido mencionando en este apartado y las aportaciones de más personas tenemos el planificador de RIO *radiance*, con el que he sacado muchos de los resultados de esta tesis, y otras soluciones con las que obtener más información acerca de los tratamientos de RIO. También me gustaría agradecer a Guadalupe y a la Universidad de Valencia sus enseñanzas acerca de los sistemas de seguimiento óptico; a Ángela Camacho, Iván y María de la Jara por su tiempo ayudándonos con nuestros experimentos; a los radiofísicos (Elisa, Miguel Ángel…) y a los técnicos de radioterapia de la Clínica La Luz por su tiempo con el TrueBeam; a Juan Daniel de Medtronic por lograr que nos dejaran adquirir imágenes con el O-arm en el Hospital La Paz; a Carlos de GMV, a Matt de Neurologica y a la financiación de *Madrid-MIT M+Vision Consortium* porque con su ayuda conseguimos adquirir imágenes con el BodyTom en Danvers (EEUU); a los radiofísicos del Hospital Ramón y Cajal por prestarnos su maniquí de densidad electrónica para hacer nuestros experimentos; y a Vladimir de CIRS por pasarme al final los datos del maniquí de densidad electrónica. Por eso decía que esta tesis ha sido posible gracias al enorme esfuerzo de muchas personas…

También me gustaría agradecer a Manolo (Desco) la posibilidad de formar parte de este gran laboratorio hace ya diez años. Este Laboratorio de Imagen Médica (o LIM) es grande por la gente que lo compone (y, por supuesto, por los exLIMeros) y que te arropa, y porque gracias a este equipo multidisciplicar (como en radioterapia intraoperatoria) se pueden hacer cosas muy chulas y no parar de aprender ni un solo día. Guardo con mucho cariño los inicios con el equipo consolero (el gran Angelote y Alexia, que siempre ha tenido las cosas muy claras) que trataba de hacer más transparente al usuario el hardware/software de unos cracks como Vaquero, Edu, Gus, Álex, Esther, Santi pequeño, Mónica… También quiero agradecer a Joost su generosidad hacia mí. Me alegro muchísimo de que el equipo neuro haya crecido en todos los aspectos tanto con él, Yasser, Javi, David, Susana, Kenia, Luis… Como no olvidar aquellos ratos que pasé con Gonzalo tratando de desentrañar los misterios del

SPM, él hacía que fueran muy divertidos. Gracias también Marisa por confiar en mí. Y como no, las palabras de ánimo de la didáctica Esther, de la inquieta Cristina, de la gran Paula, del doctor Juan, del generoso Marco, de la supertrabajadora María acompañada por el crack Chema, de la graciosa Marina… para que terminara esta tesis. Y también de Sandra y Yolanda que irradian corazón y simpatía por donde van. Muchas gracias también a Elena, no sabes lo mucho que he aprendido de tu experiencia y con tus preguntas. También guardo con mucho cariño el tiempo compartido con Carmen, Aurora (o pajarito), Estefanía, Merche, Irene, Bego y Rafa cuando estaban con sus trabajos fin de carrera/grado/máster. Qué recuerdos con Juanjo pequeño y nuestro pequeño Juanolas, y Carlos con su vitamina L. Y qué decir del equipo materno compuesto por el equipo CT (las *jefas* [en plan cariñoso] Claudia e Inés, Álvaro, Cristóbal, Alba, Ramón, Nerea y Suzanne), el equipo Navegación (Rocío, Mónica, Bego, Rafa y David), el equipo Bio (Ana V., Joaquín, Ana R., Henar, Nico…), el químico Mario, la generosa María, Laura, Marina y María, con ellos fijo que te echas unas risas y desconectas. No quiero tampoco olvidarme de Lorena, Dani, Elena calidad, Bea, Eva, Tati, Marta, Esther, Diego, Mariví, Imke, Arrate y del resto de compañeros del LIM ni de exLIMeros como Javi Sánchez, Santi Peña, Laura Sanz, Ángela Codina, Eva Alarcón, el montañero Mikael, Juan papá, Marisa, Fidel… Y de los que no pertenecen directamente al LIM como Cristina (UNED), Guille y sus *padawans*, que no nos dejan nunca de sorprender con sus impresiones en 3D, Estela que nos malcriaba con sus dulces y Azucena, mi acompañante fija junto con la incombustible secretaria del LIM Trajana en esas tardes largas en el labo. En estos diez años, se nos fueron también otros dos grandes: el generoso Santi que era capaz de quedarse hasta las tantas explicándonos cosas y al que debo los ojos y la conexión con el radiólogo Juan y unas oftalmólogas muy inquietas como Pilar Gómez, Pilar Merino, Olga y Gema; y nuestra querida Carmen que era capaz de ver mucho más allá que cualquiera de nosotros.

I also extend my gratitude to Kirby Vosburgh for his dedication during my stay at Brigham and Women's Hospital and the people that helped me there such as Raúl, Jay, Rivka, Corey, Sila, Karl, Teresa, Carlos and personnel from AMIGO suite. I also appreciated the time spent with Edu, Cleo, Gözde, Yigitcan, Asli and Sarah a lot. Thank you so much, Matt (Neurologica) and Vladimir (CIRS), for your help; and

Majid, Frank and Uwe for their valuable suggestions during IORT German working group meetings.

Mandar un beso muy fuerte a las champiñonas (la *jefa* Aurora, Claudy, la *potter* Inés, la inteligente Elia y la positiva Judit). Gracias por esos momentazos que te cargan de energía. También para los bicivoladores Pedro y Tony, no sabéis como disfruto con esas quedadas. O a mis amigos de la uni (Edu, Silvia, Jesús, Patri, Bea, Nachete, Marta, Antonio, Iván y Cris) con Raquel, Alberto, Yann, Belén, Laura… con los que me une una amistad de más de la mitad de nuestra vida… A los amigos de Víctor, Bea, Óscar, Alberto, Edu, Pilar, Conchi, David, Álex, Nacho, Susi… con los que te partes. Y a la familia de Víctor, por su cariñosa acogida.

Dedico esta tesis a mis padres porque han hecho lo imposible por darnos lo mejor a los tres. Sé que les va a llenar de orgullo saberlo porque les he tenido *engañados* durante mucho tiempo, jeje. Sufristeis mucho con nuestras carreras y no era plan de que siguierais así por nuestros trabajos. Ahora merecéis disfrutar de todo nuestro amor. Y como no mencionar a mi hermano y a mi tío Víctor que siempre tienen ese extra de enseñar las nuevas cosas que aprenden; o a mi tía Carmen (mi vecina del primero) que *no* nos ayuda en *nada*; o a mi hermana; Rodolfo; Marta; mis sobris Sofía, Damián y el que viene en camino (Conan…); mi tío José; mi tía Sara; mis primos Elena y Víctor; la gran familia de mi padre y a los que nos cuidan desde arriba. Todos con personalidades muy distintas pero con un fuerte elemento en común que nos une al final.

Por último, quiero también dedicar esta tesis a mi compañero de viaje. A Víctor por seguirme en mis aventuras y armarse de infinita paciencia mientras yo estaba delante de un ordenador y también a Manuel por regalarme su corazón durante ya casi 20 años.

Sé que me he extendido mucho con los agradecimientos y seguro de que me olvido de alguien pero tened en cuenta que han sido muchos años en el LIM en los que poco a poco se iba haciendo esta tesis aparte de divertirnos con muchas otras cosas…

¡¡Muchas gracias a todos!!

Verónica García Vázquez (o *la Vero*…), noviembre 2016

TABLE OF CONTENTS

RESUMEN

Esta tesis se enmarca dentro del campo de la radioterapia y trata específicamente sobre la radioterapia intraoperatoria (RIO) con electrones. Esta técnica combina la resección quirúrgica de un tumor y la radiación terapéutica directamente aplicada sobre el lecho tumoral post-resección o sobre el tumor no resecado. El haz de electrones de alta energía es colimado y conducido por un aplicador específico acoplado a un acelerador lineal. La planificación de la RIO con electrones es compleja debido a las modificaciones geométricas y anatómicas producidas por la retracción de estructuras y la eliminación de tejidos cancerosos durante la cirugía. Actualmente, no se dispone del escenario real en este tipo de tratamientos (por ejemplo, la posición/orientación del aplicador respecto a la anatomía del paciente o las irregularidades en la superficie irradiada), sólo de una estimación *grosso modo* del tratamiento real administrado al paciente. Las imágenes intraoperatorias del escenario real durante el tratamiento (concretamente imágenes de tomografía axial computarizada [TAC]) serían útiles no sólo para la planificación intraoperatoria, sino también para registrar y evaluar el tratamiento administrado al paciente. Esta información es esencial en estudios prospectivos.

En esta tesis se evaluó en primer lugar la viabilidad de un sistema de seguimiento óptico de varias cámaras para obtener la posición/orientación del aplicador en los escenarios de RIO con electrones. Los resultados mostraron un error de posición del aplicador inferior a 2 mm (error medio del centro del bisel) y un error de orientación menor de 2º (error medio del eje del bisel y del eje longitudinal del aplicador). Estos valores están dentro del rango propuesto por el Grupo de Trabajo 147 (encargo del Comité de Terapia y del Subcomité para la Mejora de la Garantía de Calidad y Resultados de la Asociación Americana de Físicos en Medicina [AAPM] para estudiar en radioterapia externa la exactitud de la localización con métodos no radiográficos, como los sistemas infrarrojos). Una limitación importante de la solución propuesta es que el aplicador se superpone a la imagen preoperatoria del paciente. Una imagen

intraoperatoria proporcionaría información anatómica actualizada y permitiría estimar la distribución tridimensional de la dosis.

El segundo estudio específico de esta tesis evaluó la viabilidad de adquirir con un TAC simulador imágenes TAC intraoperatorias de escenarios reales de RIO con electrones. No hubo complicaciones en la fase de transporte del paciente utilizando la camilla y su acople para el transporte, o con la adquisición de imágenes TAC intraoperatorias en la sala del TAC simulador. Los estudios intraoperatorios adquiridos se utilizaron para evaluar la mejora obtenida en la estimación de la distribución de dosis en comparación con la obtenida a partir de imágenes TAC preoperatorias, identificando el factor dominante en esas estimaciones (la región de aire y las irregularidades en la superficie, no las heterogeneidades de los tejidos).

Por último, el tercer estudio específico se centró en la evaluación de varias tecnologías TAC de kilovoltaje, aparte del TAC simulador, para adquirir imágenes intraoperatorias con las que estimar la distribución de la dosis en RIO con electrones. Estos dispositivos serían necesarios en el caso de disponer de aceleradores lineales portátiles en el quirófano ya que no se aprobaría mover al paciente a la sala del TAC simulador. Los resultados con un maniquí abdominal mostraron que un TAC portátil (BodyTom) e incluso un acelerador lineal con un TAC de haz de cónico (TrueBeam) serían adecuados para este propósito.

ABSTRACT

This thesis is framed within the field of radiotherapy, specifically intraoperative electron radiotherapy (IOERT). This technique combines surgical resection of a tumour and therapeutic radiation directly applied to a post-resection tumour bed or to an unresected tumour. The high-energy electron beam is collimated and conducted by a specific applicator docked to a linear accelerator (LINAC). Dosimetry planning for IOERT is challenging owing to the geometrical and anatomical modifications produced by the retraction of structures and removal of cancerous tissues during the surgery. No data of the actual IOERT 3D scenario is available (for example, the applicator pose in relation to the patient's anatomy or the irregularities in the irradiated surface) and consequently only a rough approximation of the actual IOERT treatment administered to the patient can be estimated. Intraoperative computed tomography (CT) images of the actual scenario during the treatment would be useful not only for intraoperative planning but also for registering and evaluating the treatment administered to the patient. This information is essential for prospective trials.

In this thesis, the feasibility of using a multi-camera optical tracking system to obtain the applicator pose in IOERT scenarios was firstly assessed. Results showed that the accuracy of the applicator pose was below 2 mm in position (mean error of the bevel centre) and 2º in orientation (mean error of the bevel axis and the longitudinal axis), which are within the acceptable range proposed in the recommendation of Task Group 147 (commissioned by the Therapy Committee and the Quality Assurance and Outcomes Improvement Subcommittee of the American Association of Physicists in Medicine [AAPM] to study the localization accuracy with non-radiographic methods such as infrared systems in external beam radiation therapy). An important limitation of this solution is that the actual pose of applicator is superimposed on a patient's preoperative image. An intraoperative image would provide updated anatomical information and would allow estimating the 3D dose distribution.

The second specific study of this thesis evaluated the feasibility of acquiring intraoperative CT images with a CT simulator in real IOERT scenarios. There were no complications in the whole procedure related to the transport step using the subtable and its stretcher or the acquisition of intraoperative CT images in the CT simulator room. The acquired intraoperative studies were used to evaluate the improvement achieved in the dose distribution estimation when compared to that obtained from preoperative CT images, identifying the dominant factor in those estimations (air gap and the surface irregularities, not tissue heterogeneities).

Finally, the last specific study focused on assessing several kilovoltage (kV) CT technologies other than CT simulators to acquire intraoperative images for estimating IOERT dose distribution. That would be necessary when a mobile electron LINAC was available in the operating room as transferring the patient to the CT simulator room could not be approved. Our results with an abdominal phantom revealed that a portable CT (BodyTom) and even a LINAC with on-board kV cone-beam CT (TrueBeam) would be suitable for this purpose.

1 LIST OF ABBREVIATIONS

2D	Two-dimensional
3D	Three-dimensional
AAPM	American Association of Physicists in Medicine
ABS	Acrylonitrile butadiene styrene
ASTRO	American Society for Radiation Oncology
CBCT	Cone-beam computed tomography
CT	Computed tomography
CTV	Clinical target volume
DNA	Deoxyribonucleic acid
DTA	Distance-to-agreement
DVH	Dose-volume histogram
EBRT	External beam radiation therapy
ELIOT	Electron intraoperative therapy
EMTS	Electromagnetic tracking system
FOV	Field of view
FRE	Fiducial registration error
GTV	Gross tumour volume
Gy	Gray
HA	Hydroxyapatite
HDR	High-dose rate
HU	Hounsfield units
ICRP	International Commission on Radiological Protection
ICRU	International Committee for Radiological Units
IMU	Inertial measurement unit
intraCT	Transformed intraoperative CT image
IOERT	Intraoperative electron radiation therapy
IORT	Intraoperative radiation therapy
IR	Infrared

ISIORT	International Society of Intraoperative Radiation Therapy
keV	Kilo-electron volt
kV	Kilovoltage
kVp	Kilovoltage peak
LED	Light-emitting diode
LINAC	Linear accelerator
MOSFET	Metal oxide semiconductor field-effect transistor
MSCT	Multislice CT
MeV	Mega-electron volt
MV	Megavoltage
OAR	Organ at risk
OBI	On-board imager
OR	Operating room
OTS	Optical tracking system
PDD	Percentage of depth dose
PET	Positron emission tomography
PLA	Polylactic acid
PMMA	Polymethyl methacrylate
POM	Polyoxymethylene
preCT	Registered preoperative CT image
$preCT_{air}$	preCT with air gap
$preCT_{water}$	preCT assuming water
PTV	Planning target volume
RMS	Root mean square
ROI	Region of interest
RPM	Real-time position management
SD	Standard deviation
SI	International System of Units
SPECT	Single photon emission computed tomography
SSD	Source-to-surface distance
TDP	Transverse dose profile

TG	Task group
TOF	Time-of-flight
TPS	Treatment planning system
US	Ultrasound
WBI	Whole breast irradiation
WHO	World Health Organization
XVI	X-ray volume imaging

2 MOTIVATION AND OBJECTIVES

2.1 MOTIVATION

Intraoperative electron radiation therapy (IOERT) is a technique that combines surgical resection of a tumour and therapeutic radiation directly applied to a post-resection tumour bed or to an unresected tumour. The procedure involves delivery of a single-fraction, high electron radiation dose [1]. The electron beam is collimated and conducted by a specific applicator docked to a linear accelerator (LINAC). Dosimetry planning for IOERT is challenging owing to the geometrical and anatomical modifications produced by the retraction of structures and removal of cancerous tissues during surgery. Nowadays, radiation oncologists choose the treatment parameters during surgery according to the surgical scenario and clinical experience. Moreover, energy selection is based on dose profiles measured in water phantoms for different electron beam energies, applicator diameters and bevel angles. A further step in IOERT is the use of a specific treatment planning system (TPS) that enables simulating both the surgical procedure and the radiotherapy set-up with a preoperative computed tomography (CT) image [2, 3]. The treatment planning process includes delineating the target volume and organs at risk; simulating the expected incision, tumour resection and organ displacement; adding biological fluid accumulation, bolus materials, shielding discs and the applicator; and estimating the three-dimensional (3D) dose distribution. Patient position, surgical access, tumour resection and IOERT treatment set-up in the actual IOERT field can differ from those simulated in the TPS. Some studies have proposed the use of intraoperative images to check the alignment between the shielding disc, the applicator and the tumour bed in breast IOERT [4-6]. Moreover, in-vivo dosimetry would allow point and two-dimensional (2D) dose measurements [7-11]. However, no data of the actual IOERT 3D scenario is available (for example, the applicator pose in relation to the patient's anatomy or the irregularities in the irradiated surface) and consequently only a rough approximation of the actual IOERT treatment administered to the patient can be estimated. For instance, some tissues in the

surgical cavity may interfere with applicator placement making the electron beam oblique to the irradiated surface and creating air gaps. A recent study has shown that curved irradiation surfaces caused dose distributions to be curved and deeper than those with flat surfaces [12]. Additionally, a cavity smaller than the applicator produced hot spots (high-dose regions) close to the surface followed by a fast dose reduction. Intraoperative CT images of the actual scenario during the treatment would be useful not only for intraoperative planning but also for registering and evaluating the treatment administered to the patient. This information is also essential for prospective trials. These CT studies would allow quantifying the improvement achieved in the dose distribution estimation when compared to that obtained from preoperative CT images.

2.2 OBJECTIVES

The main objective of this thesis is to propose and evaluate new approaches to improve the existing information on the actual IOERT treatment delivered to the patient.

The specific objectives of this thesis are as follows:

1. To study the feasibility of using a multi-camera optical tracking system (OTS) to obtain the applicator pose in IOERT scenarios.
2. To assess the feasibility of acquiring intraoperative CT images in real IOERT scenarios and to evaluate the improvement achieved in the dose distribution estimation when compared that obtained from preoperative CT images.
3. To evaluate several kilovoltage (kV) CT technologies that could acquire intraoperative images for estimating IOERT dose distributions.

2.3 STRUCTURE OF THE DOCUMENT

This document is divided in eleven chapters. Chapter 1 provides a list of abbreviations used throughout the document. Chapter 2 presents the motivation and the objectives of this thesis. Chapter 3 introduces IOERT with special attention to its limitations related to acquiring the actual treatment administered to the patient and also some other

concepts used throughout this thesis (for example, tracking systems). Chapter 4 focuses on the study about the feasibility of using a multi-camera OTS to obtain the applicator pose in IOERT scenarios (first specific objective of this thesis). Chapter 5 presents the study that assessed the feasibility of acquiring intraoperative CT images in real IOERT scenarios, and the difference between dose distributions estimated with intraoperative images (*gold standard*) and preoperative images (second specific objective of this thesis). Chapter 6 focuses on the evaluation of several kV CT technologies other than CT simulators to acquire intraoperative images for estimating IOERT dose distributions (third specific objective of this thesis). Chapter 7 presents a general discussion. Chapter 8 focuses on the main conclusions drawn from the studies presented in this thesis. Chapter 9 introduces some possible future lines of research derived from this thesis. Chapter 10 shows the author's main publications. Finally, chapter 11 provides the references used throughout the document.

3 INTRODUCTION

This chapter introduces intraoperative electron radiation therapy (IOERT), beginning with the interaction of electrons and its secondary particles with matter, the principles of IOERT, its characteristic dose distributions measured in water phantoms, some special considerations for dose estimation in patients (surgical cavity and heterogeneous tissues) and the advantages and limitations of a treatment planning system specifically designed for this radiotherapy treatment. Finally, some other concepts used throughout this thesis are also described, namely how to compare dose distributions, stoichiometric calibration and tracking systems.

3.1 IOERT

According to the World Health Organization (WHO), cancer was the second cause of death (8.2 million, 21.7%, in 2012 worldwide) among chronic diseases after cardiovascular diseases (46.2%) and followed by respiratory diseases (10.7%) and diabetes (4%) [13]. Moreover, the incidence was 14.1 million during 2012. The most common sites of those new cancer cases were lung, prostate, colorectum, stomach and liver cancer in men; and breast, colorectum, lung, cervix and stomach cancer in women. The tendency is that the number of new cancer cases will increase to 22 million by 2022. Uncontrolled proliferation of cancer cells and their propagation to nearby tissues and, at the latest stages, to distant tissues is caused by an accumulation of deoxyribonucleic acid (DNA) alterations in genes that control cell division, cell growth, programmed cell death (apoptosis) and DNA repair [14]. DNA is the molecule that contains the genetic information to synthetise proteins with a specific cellular function. That growth of cancer cases is directly related to recent increase in life expectancy due to the accumulation of mutations in the DNA over time as a person gets older. According to WHO, prevention, early detection and patients' management are the key factors to reduce and control cancer disease.

Traditional cancer treatments include surgical resection, chemotherapy and radiotherapy. The latter is based on applying ionizing radiation (radiation that has enough energy to eject electrons from atoms), usually in the form of photons (X-rays and gamma rays) or electrons. Radiobiological damage is caused by DNA ionization or by ionization of water contained in the cellular medium which in turn releases free radicals that react with DNA [15]. If damaged DNA cannot be repaired, cell death is produced mainly by mitotic catastrophe or apoptosis. Radiosensitivity is related to cell proliferation. Rapid cell division is a typical behaviour of cancer cells but also of bone marrow cells, intestinal tissues, hair follicles and nails [16]. Therefore, radiotherapy does not differentiate between cancer cells and healthy cells.

Intraoperative electron radiation therapy (IOERT) is a technique that combines surgical resection of a tumour and therapeutic radiation directly applied to the post-resection tumour bed or to the unresected tumour. The procedure involves delivery of a single-fraction, high electron radiation dose [1]. That radiation is collimated and conducted by a specific applicator docked to a linear accelerator (LINAC) (Figure 1). IOERT is not the only approach in intraoperative radiation therapy (IORT) as other alternatives are high-dose rate [HDR] brachytherapy (radioactive sources that emit gamma radiation) and low-kilovoltage (kV) X-ray technologies such as Intrabeam system (50 kV, Carl Zeiss Meditec AG, Germany) and Axxent MPX system (20–50 kV, Xoft Inc., USA, electronic brachytherapy). However, IOERT allows treating deeper volumes than HDR brachytherapy or low-kV X-ray technologies (up to 0.5–1.0 cm from applicator surface for the latter technologies) with a more homogeneous dose distribution [17].

IOERT enables direct visualization of the target volume. In addition, shielding or displacement of adjacent tissues and organs makes it possible to increase the dose to the target volume (range of 10–20 Gy) while minimizing the risk of irradiating healthy tissue [18]. The target volume in IOERT is the tumour bed (that presents high probability of residual cancer cells) or the macroscopic residue in the case of an unresected tumour. IOERT may also act against the mechanism of accelerated repopulation of tumour cells after surgery [1]. Moreover, after a surgery, tissues are more sensitive to radiation effect due to rich vascularization (oxygen effect) [19].

Figure 1. IOERT with a dedicated mobile LINAC.

The first IOERT cases were performed at the University of Kyoto in 1965 after the installation of a betatron, which generated electron beams, in an operating room (OR) [1]. The interest for this technique has waxed and waned over the years. For example, IOERT became popular in Japan, United States and Europe in the late 1970s and early 1980s. After that, its interest waned and then waxed again in the late 1990s with the development of mobile LINACs and the use of IOERT in breast cancer cases [20]. One reason why IOERT has not been widely adopted is its complexity, which challenges the involved multidisciplinary team of surgeons, radiation oncologists, anaesthesiologists, medical physicists, nurses, radiotherapy technicians and pathologists. This technique requires a close coordination between professionals of different disciplines to understand each other's requirements [21].

Breast and rectum represent the most common IORT sites (63.8% and 15.9% respectively, database registry of the European section of the International Society of Intraoperative Radiation Therapy [ISIORT-Europe] up to 2011 [22]). Other sites include, for example, retroperitoneal and limb soft tissue sarcomas, prostate, pancreas, or oesophagus. The aim of IOERT is to improve control of the tumour site (local control) [23]. IORT combined with other cancer treatments such as external beam radiation therapy (EBRT) and chemotherapy seems to improve local control in many cancer sites compared to not including IORT in those scenarios [24].

IOERT is used in conjunction with fractionated EBRT (photons) or as a single dose. The former corresponds to a boost on the target volume for local dose escalation. For instance, in early-stage breast cancer, an IOERT single dose (an accelerated partial breast irradiation approach) enables reducing radiotherapy time (from 5–6 weeks for postoperative whole breast irradiation (WBI) with EBRT to a single high dose with IOERT) [25] and patient's travel. Regarding disease control in this scenario, a randomised trial (electron intraoperative therapy [ELIOT] trial) revealed a significant difference of 5-year recurrence rates between postoperative WBI and IOERT single dose (0.4% and 4.4% respectively, ipsilateral breast tumour recurrences) while overall survival was identical (96.9% and 96.8% respectively) [26]. These results do not show that IOERT is as effective as postoperative WBI. The authors pointed out the difficulty when delimiting the suitable coverage of the tumour bed for those IOERT cases. On the other hand, the 5-year recurrence rates were better (1.5%) with a specific subset of patients (low-risk ELIOT group) [27]. Therefore, IOERT could be an alternative to postoperative WBI but with a proper selection of patients. Long-term results will allow assessing late side effects and outcome.

3.2 INTERACTIONS OF ELECTRONS WITH MATTER

Electrons may interact with atomic orbital electrons or atomic nuclei when passing through matter due to Coulomb forces. These interactions can be inelastic collisions (loss of kinetic energy) or elastic collisions (negligible loss of kinetic energy). A high-energy electron undergoes multiple interactions with matter compared to a high-energy photon (for example, approximately 100000 interactions for an electron beam of 3 mega-electron volt [MeV]). In this process, its trajectory changes (scattering) and it slows down following a convoluted path until all its kinetic energy is released and the surrounding atoms capture it [28]. In fact, electron range is much shorter than its path length.

When an electron interacts with an orbital electron, it changes its direction and gives up kinetic energy to that orbital electron, which can jump to a shell further from the nucleus (excitation) or be removed from the atom (ionization). In an excitation event,

the atom usually returns to stability after one or more electron transitions, emitting characteristic X-rays. In an ionization event, the ejected electron is known as secondary electron if it has enough kinetic energy to further ionise. If the orbital electron is in an outer shell, its binding energy is very low and the loss of kinetic energy in that interaction is negligible (thus the total kinetic energy of the scattered electron and the ejected electron is equal to the kinetic energy of the incident electron before the interaction). In this case, the collision is considered as elastic.

When an electron interacts with a nucleus, the electron is deflected due to proton attraction. In the case of an inelastic interaction (more probable electron-nucleus interaction [28]), the total kinetic energy of the scattered electron and the *recoil* nucleus differs from the electron kinetic energy before the interaction. The loss of electron kinetic energy involved in this slowing-down process is converted to a photon. This mechanism is known as bremsstrahlung or "braking radiation". The photon energy varies from 0 to the energy of the incident electron. This electromagnetic radiation mainly follows a right angle to the electron direction in the case of lower electron energies while the angle decreases for higher electron energies.

In a medium of low atomic number (for example, water or tissue) electrons lose its kinetic energy mainly by excitation and ionization. By contrast, in a medium of high atomic number (for example, lead or tungsten) bremsstrahlung production is a more likely interaction. For example, in photon radiotherapy, high-energy X-rays are usually generated by bombarding materials of high atomic number with a beam of high-energy electrons. The mass stopping power (the average energy loss per traversed distance and per material density) includes the energy loss due to ionization and excitation (collisional loss) and the energy loss due to bremsstrahlung (radiation loss). The mass stopping power due to collisional losses increases for materials of low atomic number because materials of high atomic number have fewer electrons per gram (electron density) and those electrons are more tightly bound. On the other hand, the mass stopping power due to radiation losses increases with atomic number and electron kinetic energy (Figure 2). The rate of energy loss is about 2 MeV/cm in water or soft tissue [29].

The electron beam is scattered by, mainly, interactions with the nuclei [29]. The mass scattering power is the mean square scattering angle per traversed distance and per material density. This parameter increases with atomic number and decreases with higher electron kinetic energy [30]. Low-energy electrons are more likely to deflect following larger scattering angles.

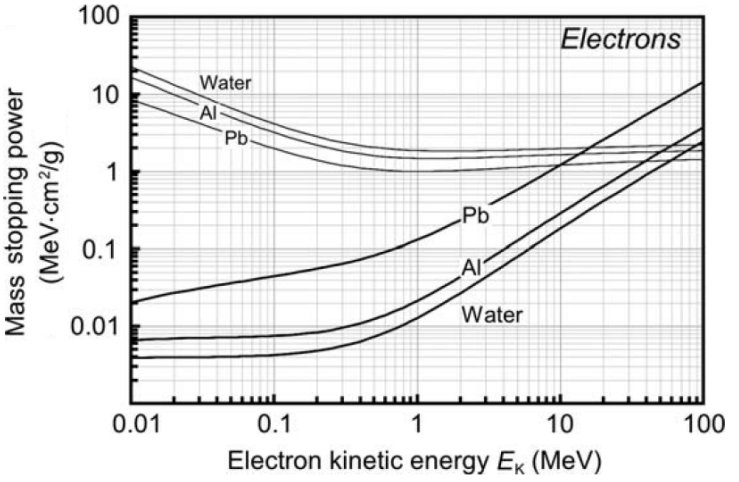

Figure 2. Mass stopping power for water, aluminum and lead materials. Values for collisional losses (narrow lines) and values for radiation losses (thick lines). Source [30].

As previously mentioned, the interaction of high-energy electron beams with matter produces ionizations (free electrons apart from those of the electron beam) and photons (characteristic X-rays and bremsstrahlung). This electromagnetic radiation, in turn, also interacts with matter by means of the following processes: coherent (Rayleigh) scattering, photoelectric effect, incoherent (Compton) scattering, pair production and photodisintegration. In Rayleigh scattering, photoelectric effect and Compton scattering, the incident photon interacts with an atomic orbital electron while in pair production and photodisintegration the photon interaction is with the electromagnetic field of an atomic nucleus. The details of these processes are as follows:

- In Rayleigh scattering, the atom absorbs an incident photon, emitting afterwards a second photon with the same energy as the incident photon but in a different direction. This interaction is more common in materials of high

atomic number and with photons of very low energy (not enough to ionise the atom).

- In photoelectric effect, the atom absorbs an incident photon with enough energy to ionise it. The kinetic energy of the ejected electron (called photoelectron) is equal to the difference between the photon energy and the electron binding energy. The vacancy created in the involved inner shell is filled by an electron of an outer electron shell. The electron energy lost in that process is emitted as characteristic X-rays. Photoelectric effect is predominant in materials of high atomic number and with photons of low energy (kilo-electron volt [keV] range).
- Compton scattering is similar to photoelectric effect but, in this case, the ejected electron is located in an outer shell. Another scattered photon of less energy is also emitted since the electron binding energy is much lower than the incident photon energy. This interaction is independent of the atomic number and is more common at intermediate energies (high keV to low MeV range).
- In pair production interaction, the atom absorbs an incident photon creating an electron and a positron. Both particles share the energy of the incident photon minus the energy needed to create the electron-positron pair (1.02 MeV, twice the rest mass energy of an electron). A positron is the electron antiparticle (same mass as the electron but opposite charge) and loses its kinetic energy as an electron does. The difference is that, at the end of its range, the positron collides with an electron of an outer shell and both particles are destroyed, emitting two 511 keV gamma rays which travel in opposite directions (annihilation process). Pair production is more common at higher energies (high MeV range) [15].
- In photodisintegration, the nucleus suddenly absorbs the incident photon emitting neutrons, which in turn also ionise matter, and gamma rays. This is the main reason for neutron contamination in high-energy accelerators for radiotherapy. This interaction occurs at very high photon energies (greater than 10 MeV) with materials of high atomic number.

Charged particles (for example, electrons and protons) are directly ionizing radiation since many ionization events occur along a particle path while uncharged particles (for example, photons and neutrons) are indirectly ionizing radiation since these particles do not produce multiple ionization events. In fact, their secondary charged particles generated are responsible of this process.

3.3 ELEMENTS OF AN IOERT PROCEDURE

The electron beam is accelerated to the high energies used in IOERT (4–20 MeV [17]) in a LINAC. The electrons gain energy by interacting with high-frequency electromagnetic waves (microwave range) in a linear tube. The high-energy electron beam is a narrow pencil beam (about 3 mm in diameter) when exiting the window of the accelerator tube. Then, the electron beam is spread with an electron scattering foil located in the treatment unit head (Figure 3). This device is a thin metallic foil of high atomic number to reduce the X-ray contamination (bremsstrahlung) of the electron beam. The electron scattering foil is also used to get uniform electron fluence in the treatment field (cross section). After that, the electron beam strikes an ion chamber to monitor dose delivery. Collimators and the electron applicator attached to the treatment unit head are used to confine the electron beam towards the treatment field within the surgical area since electrons easily scatter in air at energies lower than 15 MeV [31]. These devices are designed to, at least, maintain the beam flatness. The different elements in the treatment unit head, the applicator, air and the patient interact with the electron beam spreading its almost monoenergetic spectrum showed before exiting the window of the accelerator tube and contaminating it with X-rays (bremsstrahlung) [32].

IOERT is carried out with a conventional LINAC routinely used for EBRT or with a dedicated mobile LINAC. In the former case, the X-ray target (material of high atomic number where the high-energy electron beam strikes to produce Bremsstrahlung X-rays) used in the photon mode of the LINAC operation is removed during IOERT. In addition, the flattening filter (device to get a uniform photon beam intensity across the field) is replaced with the electron scattering foil (Figure 3). In such IOERT scenario, the anaesthetised patient is transferred from OR to the LINAC room (bunker) for

irradiation and after that, to the OR again for surgical closure. Moreover, EBRT treatments must be interrupted during radiation delivery in IOERT. Dedicated mobile LINACs eliminate the need of patient's transportation as these devices can be moved inside the OR for patient's irradiation (Figure 1). LIAC, Novac (Sordina IORT Technologies S.p.A, Italy) and Mobetron (IntraOp Medical Corporation, USA) are examples of such devices. These miniaturised LINACs generate only electron beams (up to 12 MeV) and do not include bending magnets (required when the direction of the electron beam coming from the accelerator tube must be modified) that would produce X-ray leakage. X-ray and neutron leakage from the accelerator head, electron leakage from the applicator and bremsstrahlung produced in the patient are low enough according to radiation protection requirements to use these machines inside an OR without permanent shielding [20]. In these devices, the dose rate is high because their source-to-surface distance (SSD) is shorter than those in conventional LINACs, so irradiation time is considerably reduced (about 10 times faster, less than 1 minute for a dose of 21 Gy) [4, 33].

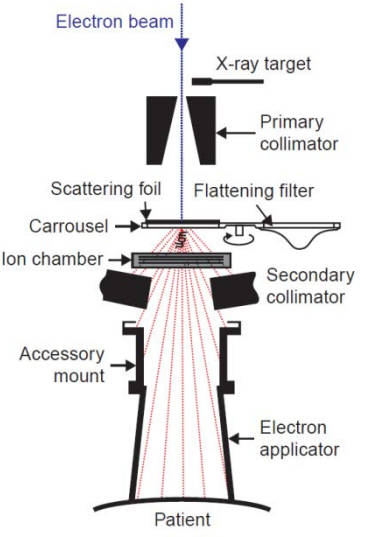

Figure 3. Treatment unit head configuration of a LINAC. Source [29].

In a hard-docking device, the applicator system consists of two parts that are rigidly connected before the delivery of the radiotherapy treatment:

- Cone: a hollow cylinder that is attached to the treatment unit head.
- Bevel: another hollow cylinder (same diameter as the cone) with a flat-end or bevelled end that is in contact with the patient's surface (over the tumour bed or the residual tumour). This part also functions as a retractor of healthy tissues [34].

On the other hand, Mobetron IOERT LINAC is a soft-docking system, where the applicator consists of one part with circular, elliptical or rectangular section to better fit the irradiated surface. Central axes of both applicator and LINAC are aligned with lasers [20].

In IOERT, internal shielding plates are used to minimise the risk of irradiating critical tissues that cannot be displaced enough. For example, in breast IOERT scenarios a shielding disc is placed between the pectoralis major muscle and the mammary gland to protect the underlying structures (ribs, lungs, heart) during irradiation (Figure 4). The thickness of this protection and its area depend on the electron beam energy to be absorbed and the field size respectively. Shielding discs are commonly made of lead. However, this material produces bremsstrahlung and backscatter electrons due to its high atomic number, and, in turn, enlarges the dose at the interface between tissue and lead in the upstream direction of the incident beam. This overdosage may cause unnecessary complications to the mammary gland above the shielding disc. Electron backscatter increases with materials of higher atomic number and decreases with higher energies. A two-layered disc approach is preferred to avoid this problem, where another shielding disc of low atomic number (*first disc*, for example, aluminum, polymethyl methacrylate [PMMA] or Teflon) is positioned above the disc of high atomic number (*second disc*, for example, lead, copper or stainless steel) and towards the residual breast to absorb the backscattering radiation (Figure 4). The alignment between the shielding discs and the tumour bed is partially checked with a needle when measuring the thickness of the target volume due to the lack of direct visual disc inspection.

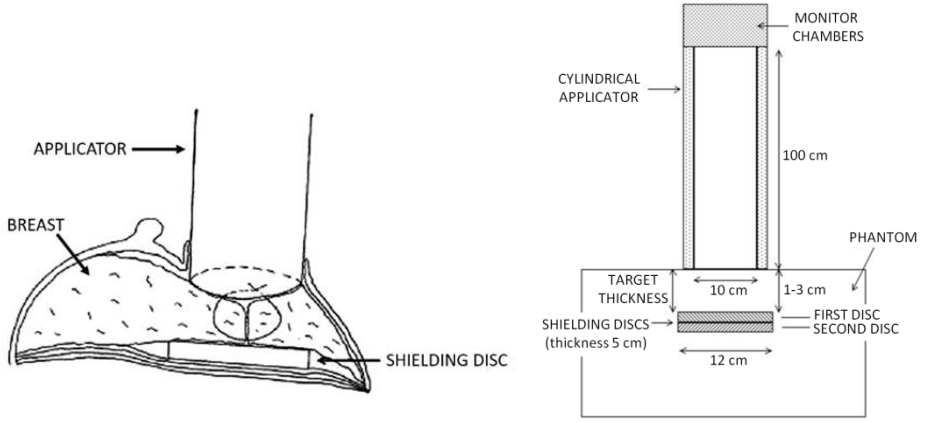

Figure 4. Breast IOERT set-up with the margins of the tumour bed temporarily approximated with sutures (left, adapted from [25]) and an example using a two-layered disc approach (right, adapted from [35]).

3.4 DOSE DISTRIBUTIONS FOR ELECTRON BEAMS

The dose is defined as the energy absorbed from the radiation beam per unit mass of the irradiated tissue and is measured in Gray (Gy, International System of Units [SI]), which is the absorption of one joule of radiation energy per kilogram of matter. It includes the energy involved in ionization and excitation processes. Dose estimation is commonly based on ionization measurements. The amount of cell killing increases when a tumour receives a higher dose [18]. Maximum IOERT doses tolerated by normal tissues are tissue dependent. For example, peripheral nerve tolerates less dose than bones.

Percentage of depth dose (PDD) profiles, their transverse dose profiles (TDPs) at certain depths (also called off-axis profiles or cross plane profiles) and isodose curves are commonly used to represent three-dimensional (3D) dose distributions. PDD is the profile along the clinical axis (the vector normal to the irradiated surface that intersects the bevel centre [Figure 5]) [21]. This axis is clinically important because the depth from the irradiated surface is relevant in IOERT. The clinical axis matches the geometric axis of the applicator (the central axis or longitudinal axis of the applicator) for non-bevelled applicators (bevel angle 0º).

Dose distributions are measured in water phantoms and depend on the electron beam energy, the treatment machine (for example, due to the elements to flatten and collimate the beam), the applicator diameter and its bevel angle.

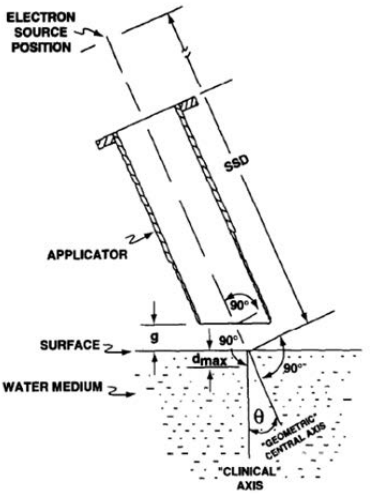

Figure 5. Clinical and geometric axes of the applicator. Thickness of the air gap between the bevel and the irradiated surface (g), depth at which the dose is maximum (d_{max}), bevel angle of the applicator (θ) and source-to-surface distance (SSD). Adapted from [21].

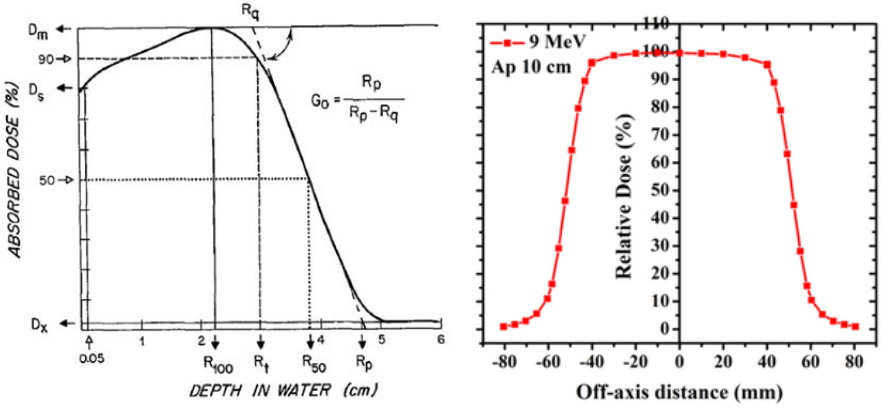

Figure 6. Dose profiles for an electron beam in water medium. PDD (left, adapted from [36]) and TDP (right, source [37]). Ap (applicator diameter).

Figure 6 displays a PDD of an electron beam in water medium. This curve shows a typical sharp falloff of dose at distances beyond a certain depth. A PDD is characterised by the following parameters [36]:

- D_s is the dose measured at 0.5-mm depth (surface dose).
- D_m is the maximum dose and is measured at depth R_{100}. The *build-up region* is the region between the surface and depth R_{100}.
- D_x is the dose due to X-ray contamination (bremsstrahlung tail). This parameter increases with the energy of the electron beam (Figure 7).
- R_t or *therapeutic range* is the clinically useful range. According to the recommendations of Task Group 25 (TG–25) of the Radiation Therapy Committee of the American Association of Physicists in Medicine (AAPM), R_t is the depth of the deepest 90% dose. In a water medium, this value (in mm) is roughly one-fourth of the nominal energy of the electron beam (in MeV) [32].
- R_p or *practical range* is the intersection between the bremsstrahlung tail and the tangent to the PDD curve (falloff portion) at the inflection point. The most probable energy of the radiation beam at the surface depends on R_p. The maximum range of the electrons is the intersection between the bremsstrahlung tail and the PDD curve.
- Finally, G_o or normalised dose gradient measures the steepness of the falloff portion, where R_q is the depth at which the previous tangent is intersected by the level D_m.

Surface dose, bremsstrahlung dose and therapeutic range become larger when increasing the energy of the electron beam (less scattering in the surface and the electron beam penetrates deeper). An opposite effect occurs with the dose gradient (Figure 7). Moreover, surface dose is larger for an electron beam than for a photon beam (Figure 7). Dose gradient has that same behaviour as surface dose due to scattering and the continuous energy loss of the electrons. PDD also depends on the field size (applicator diameter) as depicted in Figure 8 due to lateral scattering of electrons. This effect is more pronounced when increasing the energy of the electron beam. The depth of maximum dose moves towards the surface when the field size decreases.

Figure 6 shows a TDP in water medium with a typical region of homogeneous dose. The flatness and symmetry of the beam are also measured over the central 80% of this dose profile at a stated depth (water phantom). The physical penumbra is commonly determined as the distance between the 80% and 20% dose, measured in TDP at depth $R_{85}/2$ where R_{85} is the depth of the deepest 85% dose on the electron beam central axis (International Committee for Radiological Units [ICRU] recommendation) [32]. A higher energy of the electron beam decreases the penumbra at the surface as the electron beam is less scattered in air. The air gap between the bevel and the irradiated surface affects less in this case. The opposite behaviour occurs at the therapeutic range due to multiple scattering: a higher energy increases the penumbra at that depth [36].

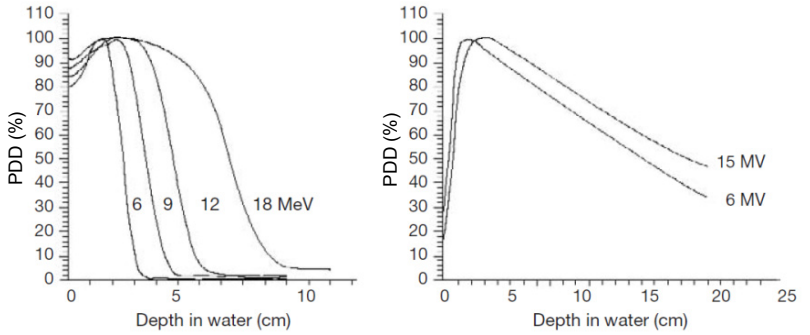

Figure 7. Comparison of the PDD of an electron beam (left) and the PDD of a photon beam. In both cases, reference field size for clinical electron beam dosimetry (10 × 10 cm) and SSD of 100 cm. Adapted from [32].

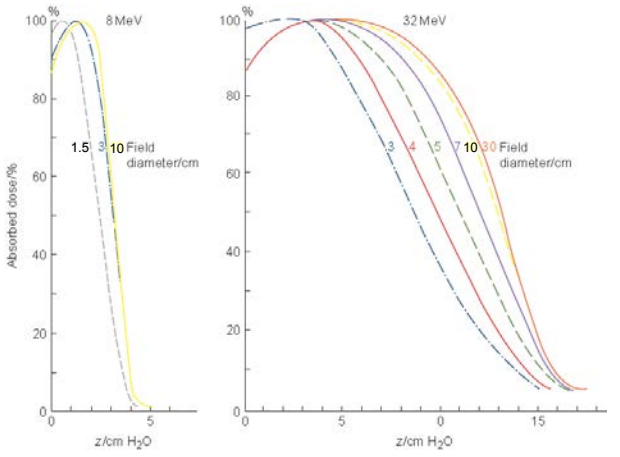

Figure 8. Variation of PDDs of an electron beam with field size and energy. Source [29].

An isodose chart is a set of lines passing through points of the same dose (isodose curves) and represents the dose variation as function of depth and off-axis distance. The isodose curves spread with depth and curves of a isodose level lower than 20% swell due to scattering [32]. Figure 9 shows the different shape of the isodose curves when using a bevelled applicator. The beam obliquity moves the depth of maximum dose towards the surface, increases the latteral scattering at that depth and decreases the depth of the 80% dose [29].

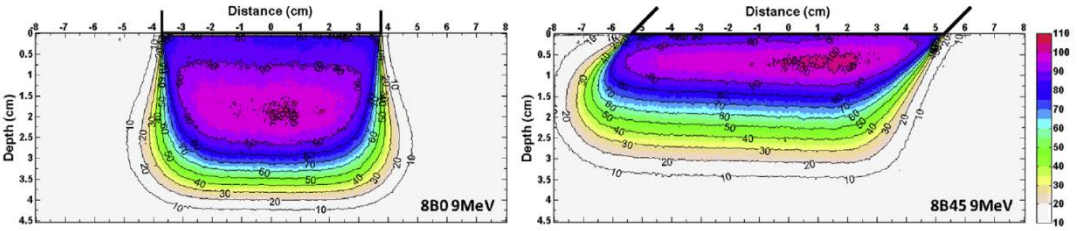

Figure 9. Isodose curves measured in solid water phantom with Gafchromic film (9 MeV electron beam). Applicator diameter of 8 cm and bevel angle of 0° (left) and of 45° (right). Source [12].

3.5 COMPARISON OF DOSE DISTRIBUTIONS

A quantitative comparison of two dose distributions (namely a reference dose distribution or *gold standard* and an evaluated dose distribution) may be carried out by means of calculating the dose difference between both distributions. However, regions of high dose gradient may lead to wrong conclusions as small spatial errors may produce large dose differences. An alternative approach is the gamma distribution that combines dose differences with the distance-to-agreement (DTA) concept that is the distance between a point from the reference dose distribution and the nearest point in the evaluated dose distribution with the same dose as that of the reference point. This method is based in calculating for each point in the reference dose distribution (3D coordinates $\boldsymbol{r}_r$) the following quality index gamma (γ) [38]:

$$\gamma(\boldsymbol{r}_r) = min\{\Gamma(\boldsymbol{r}_r, \boldsymbol{r}_e)\} \quad \forall\, \boldsymbol{r}_e \tag{1}$$

where $\boldsymbol{r}_e$ are the 3D coordinates of a point in the evaluated dose distribution and

$$\Gamma(\boldsymbol{r}_r, \boldsymbol{r}_e) = \sqrt{\frac{\left(D_r(\boldsymbol{r}_r) - D_e(\boldsymbol{r}_e)\right)^2}{\Delta D^2} + \frac{|\boldsymbol{r}_r - \boldsymbol{r}_e|^2}{\Delta d^2}} \quad (2)$$

where $D_r(\boldsymbol{r}_r)$ is the dose in the reference dose distribution at the point $\boldsymbol{r}_r$, $D_e(\boldsymbol{r}_e)$ is the dose in the evaluated dose distribution at the point $\boldsymbol{r}_e$, and ΔD and Δd are the passing criteria for dose and distance respectively. At point $\boldsymbol{r}_r$, the evaluated dose distribution is similar to the reference dose distribution if $\gamma(\boldsymbol{r}_r) \leq 1$. For two-dimensional (2D) dose distributions, this criterion is equivalent to draw an ellipsoid (semi-principal axes of length ΔD, Δd and Δd) centred at coordinates (D_r, x_r, y_r) and check if there is at least one evaluated point of coordinates (D_e, x_e, y_e) that is inside or on that ellipsoid (Figure 10).

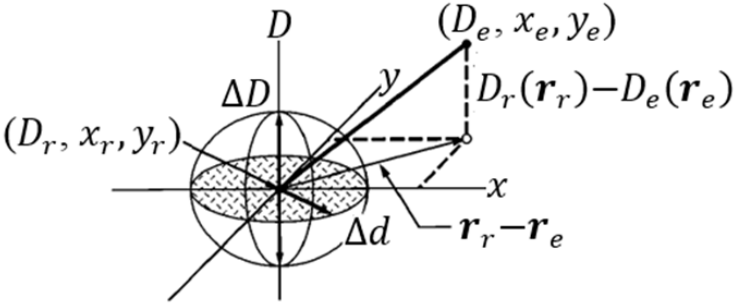

Figure 10. Geometric representation of $\gamma(r_r) \leq 1$. Adapted from [38].

Gamma distribution is the mainstay of dose distribution comparisons in medical physics. An acceptance criteria of 3% dose difference (ΔD) and a 3-mm DTA (Δd) (commonly referred to as *gamma criteria of 3%/3 mm*) for dose values greater than 10% is widely used in intensity-modulated radiation therapy [39]. The disadvantages of gamma index are that is dimensionless (for example, a dose difference is more clinically intuitive), signless (thus no information about if the reference dose distribution at point $\boldsymbol{r}_r$ is higher or lower than the evaluated dose distribution), and sensitive to dose grid resolution and to interchange between reference and evaluated dose distributions. An alternative approach is proposed in [40] where the authors introduce a dimension and sign index to compare dose distributions. That index

corresponds to a 3D dose difference weighted by dose gradient and previous passing criteria (ΔD and Δd).

3.6 SPECIAL CONSIDERATIONS IN IOERT

In IOERT treatment, radiation oncologists choose the treatment parameters (applicator diameter, bevel angle, applicator pose [position and orientation] and prescribed dose at a certain depth) during surgery according to the surgical scenario and clinical experience. The applicator diameter is selected to include the whole tumour bed or the residual tumour plus a safety margin while the bevel angle allows maximising dose homogeneity in sloping surfaces. The dose depends on the amount of residue [41]. For instance, in breast cancer treatments, the radiation oncologist usually measures the thickness of the target volume with a needle and a ruler. This process is done after firstly, placing the shielding disc and then, temporarily approximating the margins of the tumour bed with sutures. This information is given to medical physicists that choose an appropriate beam energy so that a certain percentage isodose (commonly, 90% isodose line), at which dose is prescribed, encompasses the target volume. Energy selection is based on dose profiles measured in water phantoms for different electron beam energies, applicator diameters and bevel angles.

IOERT treatments are based on several assumptions: the irradiated tissue is equivalent to water in both stopping power and scattering power, and the bevel is in contact with the patient's surface (thus the end of the applicator is parallel to the surface). However, the patient's anatomy includes heterogeneous tissues such as air, lung and bone that are not water-equivalent. Moreover, some tissues in the surgical cavity may interfere with applicator placement making the electron beam oblique to the irradiated surface and creating air gaps. Furthermore, surfaces may be irregular and biological fluid can accumulate in the surface as a result of the surgical procedure after resecting the tumour. These factors alter the dose distribution typical of water medium as follows:

- The penetration of the electron beam is larger in lungs, having higher doses than expected.

- In a small (related to field size) low-density heterogeneity, electron scattering towards this inhomogeneity is more probable than the opposite. Hot spots are produced in the dose distribution immediately under the heterogeneity and cold spots are also created lateral to that inhomogeneity due to the fluence perturbation. An opposite effect occurs in the case of a small high-density heterogeneity [42].
- Scatter produced by sharp irregularities in the irradiated surface also produces hot or cold spots in the underlying tissues, having overdose or underdose in some tissues respectively (Figure 11). In these surfaces, the electrons are mainly scattered outwards by steep projections [29]. A bolus may be placed on the area to be irradiated to try to reduce these problems as it can smooth sharp edges and flatten an irregular surface in addition to increase surface dose. Bolus requirements are flexibility to shape into the patient's surface and tissue equivalence in both stopping power and scattering power.
- An underdosage of the target volume may result from, for example, a fluid accumulation of 1.0–1.5 cm. Suction is recommended for reducing fluid build-up [20].

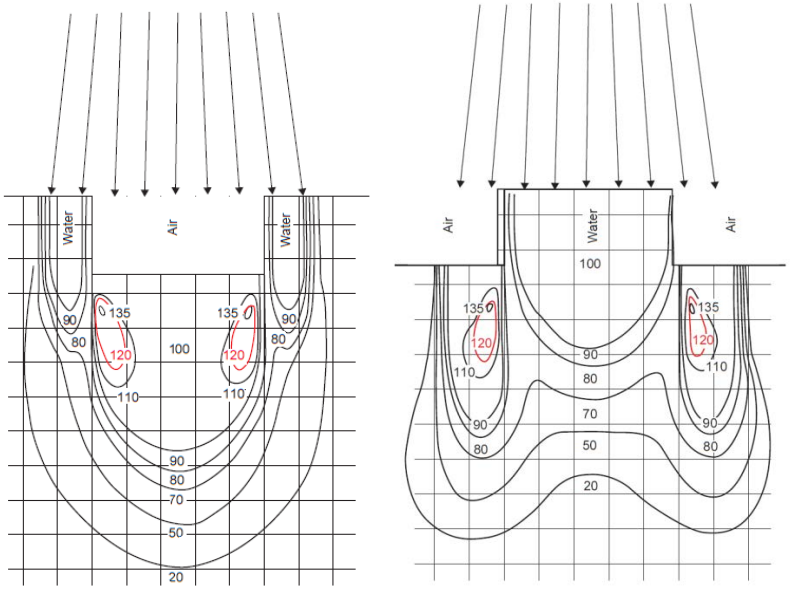

Figure 11. Isodose curves for an electron beam and sharp surface irregularities. Adapted from [29].

There are some dose corrections for air gaps (such as that displayed in Figure 12) and for specific tissue inhomogeneities that are applied in electron EBRT [29]. However, these corrections are not suitable for IOERT as a surgical cavity is more complex and its actual surface shape is unknown. Moreover, estimation of the dose distribution is difficult to achieve when having small heterogeneities due to electron scattering [29].

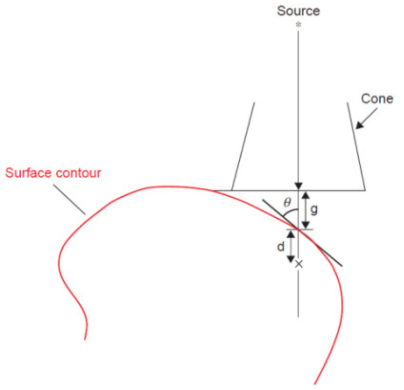

Figure 12. Example of an air gap between the applicator end and the irradiated curve surface. Dose of a point at depth *d* is corrected based on the air gap of height *g* and the angle *θ*. Adapted from [29].

AAPM Radiation Therapy Committee TG–72 pointed out that, in IORT, further research is needed to evaluate "the effects of beam misalignment, gaps, bolus, changes of penumbra and tissue inhomogeneities in realistic patient geometries" [43]. Following that recommendation, in [44] the authors showed the effect of the misalignment between the shielding disc and the applicator. The dose distribution in the target volume did not significantly vary with disc translation and disc rotation of up to 10º. However, a translation of the shielding disc equal to or greater than the difference between its radius and the internal radius of the applicator or a disc rotation of above 20º resulted in irradiation of healthy tissues. On the other hand, in [12] the authors simulated some characteristic pelvic IOERT scenarios (rectal cancer) with solid water slabs and radiotherapy bolus. The bevel commonly used in these cases is 45º while a non-bevelled applicator is mainly used in breast IOERT [22]. The irradiation surface is commonly irregular and/or concave in rectal IOERT. In addition, flatten pelvic IOERT surfaces is not easy compared to this task in breast cases. In that study, the authors showed that curved irradiation surfaces caused dose distributions to be curved and deeper than those with flat surfaces. Moreover, a cavity smaller than the

applicator produced hot spots close to the surface followed by a fast dose reduction (Figure 13). That group presented in vivo 2D dose distributions for pelvic IOERT with Gafchromic EBT3 films (radiochromic films), showing different results along the irradiated surface which did not correspond to expected values (Figure 14) [10]. The authors also underlined the influence of fluid build-up and the presence of surface hotspots due to step-like irregularities. Therefore, the actual scenario is important in IOERT to calculate doses more accurately.

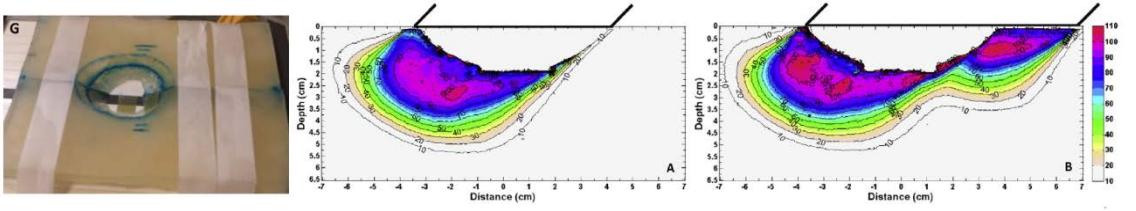

Figure 13. IOERT dose distributions for curved irradiation surfaces measured with Gafchromic EBT3 film (9 MeV electron beam). Simulated surgical cavity with solid water slabs and radiotherapy bolus (left), isodose curves for an applicator of 6-cm diameter and bevel angle of 45° (centre) and isodose curves for an applicator of 8-cm diameter and bevel angle of 45° (right). Adapted from [12].

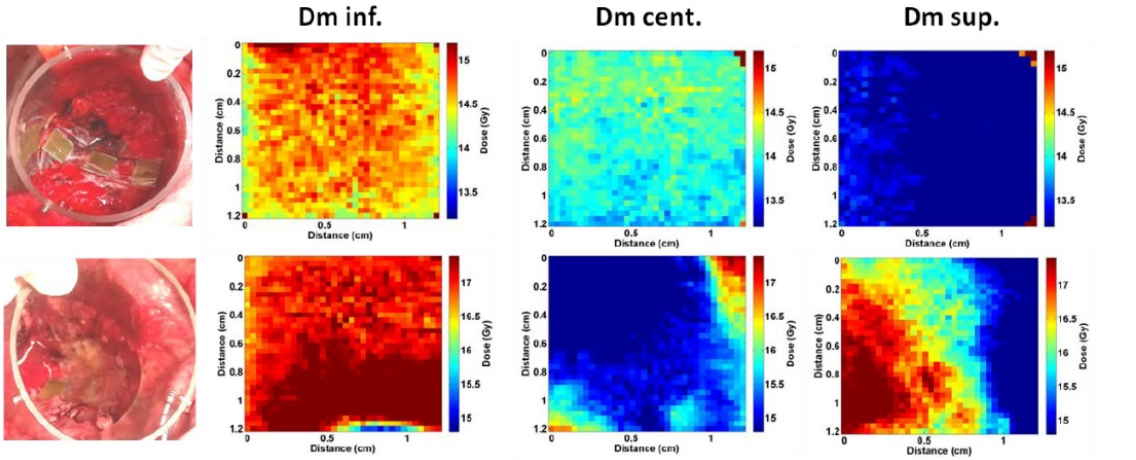

Figure 14. In vivo 2D dose distributions for pelvic IOERT measured with three Gafchromic EBT3 films located on each irradiation surface. From left to right, IOERT scenario and results from Gafchromic EBT3 films placed on the surface at *R*-3.4cm (*Dm inf.*), R (*Dm cent.*) and *R*+3.4cm (*Dm sup.*), where *R* is the bevel centre. Expected positioning uncertainty of ± 1 cm. The left side in the photograph corresponds to the longest edge of the applicator (deeper position [inf.]). From top to bottom, case 1 with an applicator diameter of 8 cm and bevel angle of 0° (expected surface dose at *R*: 13.9 Gy) and case 2 with an applicator diameter of 9 cm and bevel angle of 45° (expected dose at *R*: 13.8 Gy). In both treatments, the energy of the electron beam was 9 MeV. Case 1 was identified as the only flat surface in this study with good agreement between the dose of the central film and its expected value. *Dm sup.* (case 1) was likely in the penumbra region. The higher dose in *Dm inf.* (case 2) was probably due to fluid build-up. Adapted from [10].

3.7 TREATMENT PLANNING SYSTEM

The first step in EBRT (photons) is the simulation step where a specific patient's computed tomography (CT) image is acquired in a CT simulator. That device is a dedicated radiation oncology CT scanner with a larger bore than a conventional diagnostic CT scanner, a flat table similar to that of a radiotherapy treatment machine and a laser positioning system. A CT simulator enables acquiring the patient in the same position as during the radiotherapy treatment (for example, including special immobilization devices). The treatment planning process starts loading that study and other patient's useful images (prior CT, magnetic resonance or positron emission tomography [PET] studies) into a treatment planning system (TPS) to delineate the gross tumour volume (GTV, i.e. the visible tumour volume), the clinical target volume (CTV, i.e. GTV plus a margin for subclinical tumour spread), the planning target volume (PTV, i.e. CTV plus a margin that takes account of set-up inaccuracy and organ movements) and organs at risk (OARs) [45]. After that, the optimal treatment parameters (patient's position relative to the radiation source, number of treatment fields, collimator shape and photon energy) are selected in the TPS. Then, the dose delivered to target and critical volumes is estimated based on the study acquired in the CT simulator, the conversion between Hounsfield units (HU) and density, and the knowledge of the interactions of photon beams with body tissues (forward planning). Finally, the estimated dose distribution can be visualised directly on the patient's anatomy (for example, CT image) and dose information such as cumulative dose-volume histograms (DVHs) is also displayed. DVHs show the percentage of volume of a specific structure (target or OAR) that absorbs at least a certain dose (Figure 15).

During every EBRT treatment session, patients are positioned in the treatment room by aligning skin tattoos or immobilization devices marked during the simulation step with in-room laser beams. Image guidance technologies such as orthogonal megavoltage (MV) or kV portal images, MV or kV cone-beam CT (CBCT), in-room CT, and ultrasound (US) are used to improve beam alignment with respect to the target volume [46].

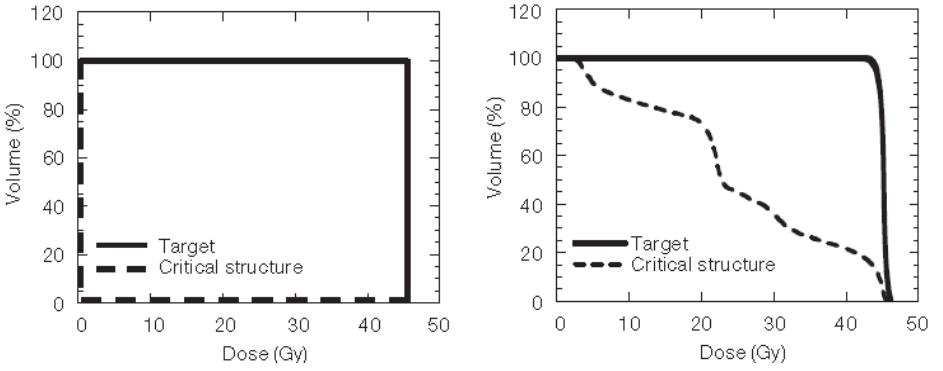

Figure 15. Ideal cumulative DVH (left) and a cumulative DVH for a prostate treatment plan (right). Ideally, the 100% of the target volume would receive the prescribed dose and the 0% of the critical structure volume would receive a dose different to 0 Gy. Source [47].

A further step in IOERT is the use of a specific TPS (RADIANCE, GMV, Spain) [2, 3] which allows estimating the IOERT dose distribution from a preoperative CT study. This software was developed in collaboration with Hospital General Universitario Gregorio Marañón (Madrid, Spain). This TPS enables delineating GTV, CTV (the tumour bed) and OARs on that CT image (Figure 16). PTV makes no sense in IOERT. Surgical access (the expected incision area), tumour resection and organ displacement can be simulated by filling these regions with air in the preoperative CT study. Moreover, biological fluid accumulation, bolus materials and shielding discs may also be incorporated in the IOERT plan. After that, the user selects a specific applicator diameter, bevel angle and energy of the electron beam, adjusting the pose of a virtual applicator with those specifications with the help of the orthogonal views (sagittal, coronal and axial) and the volume rendering view of that CT study. Then, the 3D dose distribution is estimated, taking account of tissue heterogeneities or assuming all tissues equivalent to water. Finally, the user can visualise isodose curves superimposed on patient's preoperative image and further evaluate information from the 3D dose distribution such as PDD, TDPs and cumulative DVHs (Figure 16). This process allows the radiation oncologist to assess the changes in dose distribution when modifying the surgical cavity or IOERT parameters (energy of the electron beam, applicator pose, applicator diameter and bevel angle). The objective is to maximise the dose delivered to the target volume and minimise its effect on the OARs.

In IOERT TPS, 3D dose distributions are estimated by pencil beam [48, 49] or Monte Carlo algorithms [50] specifically adapted to this setting. Pencil beam is an analytical method based on the Fermi-Eyges theory that assumes that a broad electron beam consists of many pencil beams and the dose at a certain point is the combination of their contributions. The lateral spread of each pencil beam follows, approximately, a Gaussian function whose width increases with depth (Figure 17) [32]. This theory only takes account of small angle multiple Coulomb scattering [30]. A modified Hogstrom's pencil beam used in EBRT, which takes account of other effects shown in the electron interaction with matter, was implemented in the IOERT TPS [3, 48, 49]. However, this method is subject to limitations with small irradiated volumes owing to the semi-infinite layer approximation (Figure 17) and does not model backscatter radiation [49]. On the other hand, Monte Carlo is a more accurate statistical method that simulates the propagation step by step for each electron and its secondary particles produced according to electron-matter interactions. A fast parallel version of a Monte Carlo algorithm (dose planning method, DPM) that calculates dose distributions of photon and electron beams in radiotherapy was implemented in the IOERT TPS [3, 50].

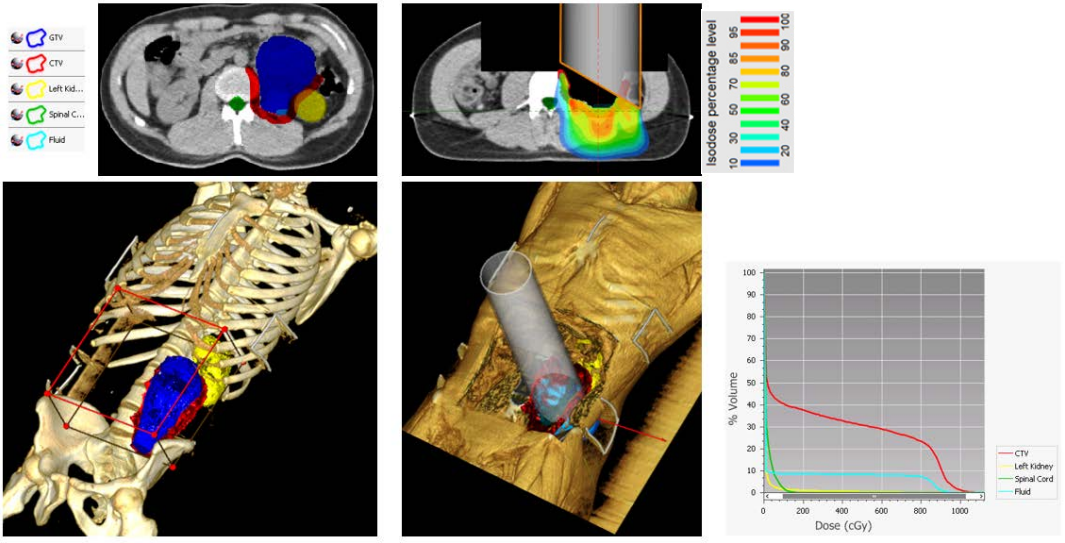

Figure 16. Example of an IOERT planning (tumour in the abdominal area). From left to right, IOERT simulation (segmentations of tumour [GTV], tumour bed [CTV] and OARs [left kidney and spinal cord], and simulation of fluid accumulation and surgical access), virtual applicator and 3D dose distribution superimposed on patient's anatomy, and DVH (CTV, left kidney, spinal cord and fluid). From top to bottom, axial view and volume rendering view.

In that TPS, the IOERT dose distribution takes account of patient's anatomy (heterogeneous tissues), the surgical cavity, biological fluid accumulation in the surface, bolus and shielding discs. This TPS enables the radiation oncologist (with close interaction of the surgeon) to plan an IOERT treatment beforehand and to adapt it to intraoperative findings and manoeuvres during surgery. However, IOERT planning is based on a simulation of both the surgical procedure and the radiotherapy set-up with the preoperative CT image.

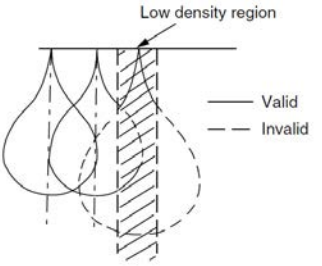

Figure 17. Effect of the semi-infinite layer approximation (pencil beam algorithm). The lateral spread of each pencil beam is estimated from the material along its main axis at each depth. Some portions of the centred and right pencil beams are wrong due to the different density region. Source [51].

Several studies have proposed the acquisition of intraoperative images to check the alignment between the shielding disc and the applicator/tumour bed in breast IOERT. These intraoperative approaches included 2D portal films (MV) [4], US images (also for measuring target depth) [6], X-ray images (acquired with a C-arm) [5] or Gafchromic films placed on shielding discs (for a posteriori analysis) [44]. On the other hand, in-vivo dosimetry with silicon diodes, metal oxide semiconductor field-effect transistors (MOSFETs), microMOSFETs and radiochromic films allows point and 2D dose measurements in an IOERT procedure [7-11]. However, no data of the final IOERT 3D scenario is available (for example, the applicator pose in relation to the patient's anatomy or the irregularities in the irradiated surface) and consequently only a rough approximation of the real IOERT treatment administered to the patient can be estimated. In [52], the authors pointed out several breast IORT limitations including the lack of intraoperative imaging to check applicator placement and to calculate 3D dose distributions before radiation delivery. For instance, in IORT HDR brachytherapy, an in-room CT-on-rails was used to acquire patient's CT images (after tumour resection

and placing a multicatheter brachytherapy balloon) to overcome those limitations [53]. Acquiring intraoperative CT images of the actual IOERT scenario may be necessary to evaluate the improvement achieved in the dose distribution estimation when compared to that obtained from preoperative CT images.

Regarding IOERT documentation, the patient's medical record includes applicator diameter; bevel angle; prescribed dose; its percentage isodose; electron beam energy (depth of prescribed dose); and, if used, characteristics of shielding plates and bolus. In addition, photographs of the IOERT scenario such as beam's eye view are also taken. However, no intraoperative 3D images of the actual IOERT scenario are routinely acquired for accurate reconstruction of the irradiated volume. This information is essential for the assessment of clinical results [24]. For instance, underdosage or overdosage of the target volume and the OARs may produce local recurrence or side effects.

3.8 STOICHIOMETRIC CALIBRATION

Dose distribution is estimated based on a patient's CT image (with all IOERT simulations such as surgical access, tumour resection, organ displacement, bolus and shielding dics), the conversion from HU to density and tissue/material type (specific for each CT simulator and acquisition parameters), the physical properties of the electron beam (specific for each treatment unit, energy and applicator), and tissue/material parameters.

The calibration curve for the transformation of HU to density is estimated from images of an electron density phantom acquired in the same CT simulator and with the same acquisition parameters that will be later used when obtaining patient's images. This phantom is made of tissue-equivalent materials that represent the densities of tissues but do not usually replicate their chemical composition. These differences lead to large dose deviations (for example, more than 30% for an 18-MeV electron beam [54]). Stoichiometric calibration is an approach to overcome this problem [55, 56]. Before explaining this method, some related concepts are detailed as follows.

The mean value of the linear attenuation coefficient μ of a tissue for an incident photon beam with a typical mean energy of 50–100 keV (diagnostic radiology) follows this expression [56]:

$$\bar{\mu} = \rho N_a \sum_{i=1}^{N} \left[\frac{w_i}{A_i} (Z_i \overline{K}^{KN} + Z_i^{2.86} \overline{K}^{sca} + Z_i^{4.62} \overline{K}^{ph}) \right] \quad (3)$$

where ρ is the (physical) density of the tissue, N_a is the Avogadro constant (6.022045 x 10^{23} mol^{-1}), N is the number of chemical elements that tissue contains, w_i is the weight proportion of the element i, A_i is its mass number (number of neutrons and protons in its nucleus), Z_i is its atomic number (number of protons in its nucleus), $\overline{K}^{KN}$ is the Klein-Nishina coefficient (related to incoherent scattering [Compton]), $\overline{K}^{sca}$ is a term related to coherent scattering (Rayleigh) and the binding correction for Compton, and $\overline{K}^{ph}$ is a term related to photoelectric absorption [56]. These three last terms are spectral dependent. The mean value of the linear attenuation coefficient ($\bar{\mu}$) is converted to HU scale (the X-ray attenuation of distilled water and attenuation of air at standard pressure and temperature are defined as 0 HU and –1000 HU respectively) by applying the following equation:

$$H = 1000 \left(\frac{\bar{\mu}}{\bar{\mu}_{H_2O}} - 1 \right) \quad (4)$$

where $\bar{\mu}_{H_2O}$ is the mean value of the linear attenuation coefficient for water. Therefore,

$$H = 1000 \left(\frac{\rho}{\rho_{H_2O}} \times \frac{\sum_{i=1}^{N} \left[\frac{w_i}{A_i} (Z_i + Z_i^{2.86} k_1 + Z_i^{4.62} k_2) \right]}{\frac{w_H}{A_H}(1 + k_1 + k_2) + \frac{w_O}{A_O}(8 + 8^{2.86} k_1 + 8^{4.62} k_2)} - 1 \right) \quad (5)$$

where ρ_{H_2O} is the density of water, H represents hydrogen, O is oxygen, $k_1 = \frac{\overline{K}^{sca}}{\overline{K}^{KN}}$ and $k_2 = \frac{\overline{K}^{ph}}{\overline{K}^{KN}}$ [56].

The stoichiometric calibration allows obtaining a conversion from HU to density adjusted to a set of *tissues* whose density and chemical composition are known. The first step of this method concerns computing the constants k_1 and k_2 of equation (5) by a constrained least squares fit of the HU measured in a CT image of the electron

density phantom. The following expression is minimised with the constraints $0 \leq k_1 \leq 1$ and $0 \leq k_2 \leq 1$:

$$f(k_1, k_2) = \sum_{j=1}^{M} \left[\frac{\bar{\mu}_j(k_1, k_2)}{\bar{\mu}_{H_2O}(k_1, k_2)} - \left(\frac{\bar{H}_j}{1000} + 1 \right) \right]^2 \quad (6)$$

where M is the number of regions of interest (ROI) measured in the CT image of the electron density phantom and $\bar{H}_j$ is the mean HU measured in that ROI j. The density and chemical composition (and also weight proportion of each element) of the phantom materials are provided by the phantom manufacturer. Once constants k_1 and k_2 are estimated for the specific CT simulator and certain CT acquisition parameters, the expected HU of each *tissue* is calculated by applying equation (5). Finally, a calibration curve (density as function of HU) is obtained with a linear interpolation of those *tissue* data and then, is entered into the TPS for dose estimation.

3.9 TRACKING SYSTEMS

Tracking systems are used in clinical applications to determine the localization of the patient and specific tools inside the treatment room. This information is necessary for the navigation system to update the 3D pose of the corresponding virtual tools relative to the patient's virtual anatomy (specifically, preoperative images and anatomical models) during an image-guided procedure. Preoperative images and anatomical models provide valuable information to identify a target in the patient. After a registration step that relates both real and virtual worlds, the navigation system helps the physician to reach that target with a specific tool, gives intraoperative orientation when no anatomical references are available and allows avoiding risk areas. By analogy with a GPS (global positioning system) navigation system, patient's virtual anatomy is the road map, the target is the destination, the tracking system is the GPS, the specific tool is the car and the driver is the physician [57].

Tracking technologies include acoustic tracking, mechanical tracking, inertial tracking, electromagnetic tracking and optical tracking. The best choice of tracking system depends on the clinical application, the working volume, whether or not it is necessary

to track inside the body, the tools to be tracked, the accuracy requirements, the update rate and space restrictions. Current commercial acoustic tracking systems are based on time-of-flight (TOF) where the distance is estimated from the time sound needs to travel from the transmitter to the receivers. Their disadvantages are inaccuracy and environmental dependence (for example, noise, reflections, media density, temperature and humidity). An example of mechanical tracking system would be a robotic arm that has a motor in each translational or rotational joint (or degree of freedom) and where the pose of the end effector is estimated with robot kinematics [58]. These systems are highly accurate and stable. Their disadvantages are motion interference and limited range due their dimensions. Moreover, one device cannot track multiple objects. An inertial measurement unit (IMU) can include three-axis accelerometers, three-axis gyroscopes and three-axis magnetometers [59]. Pose is estimated with double integration of acceleration and integration of angular velocity. This device has no range limitations but accumulates error over time. In an electromagnetic tracking system (EMTS), each sensor (specifically, coils) measures the magnetic field generated by a transmitter. The tracking system estimates the sensor pose based on the theoretical knowledge of the transmitted field. Finally, videometric and infrared (IR)-based tracking systems belong to optical tracking category. The former systems rely on identifying unique patterns or target objects in video image sequences captured with one or more digital cameras. On the other hand, IR-based systems use at least two cameras (stereo vision) to calculate the 3D coordinates of optical markers (active or passive) through triangulation. Each camera includes an IR pass filter in front of its lens to remove visible light. This modification makes marker identification easier than with a videometric tracking system. Active markers are light-emitting diodes (LEDs) that emit near-IR light and require a wire or battery to operate. Passive markers, on the other hand, are spheres with retro-reflective coatings that reflect near-IR light (coming from a ring of LEDs in every camera) back into the cameras. A specific pattern (called *rigid body*) of at least three non-collinear optical markers whose different relative distances do not vary over time is attached to the tracked tool so that the optical tracking system (OTS) can estimate its 3D pose. OTS is a popular tracking approach and offers a larger working volume and higher accuracy than EMTS. The difference in

accurary between both tracking technologies has been reduced. For example, the specifications of Aurora V2 EMTS (Northern Digital Inc. [NDI], Canada) point out an error of 0.48 mm root mean square (RMS) in position and 0.30º RMS in orientation (volume 50 x 50 x 50 cm, without electromagnetic disturbances) while those of Polaris OTS (NDI) detail an error of 0.30 mm RMS (extended pyramid, up to 1.9 x 1.5 x 3 m), (http://www.ndigital.com). EMTS sensors are smaller (up to 0.3 mm in diameter) but this type of tracking system is commonly wired and is potentially affected by large ferromagnetic objects [60-62]. On the other hand, OTS has the limitation of the required line-of-sight between the specific pattern of optical markers and the cameras. Near-IR light is also used in Microsoft Kinect (USA) to calculate depth images. That information is used to identify human shapes for skeletal tracking. Kinect version 1 obtains that depth through the deformation of a known IR structured light pattern projected onto the scenario and acquired by an IR camera. In contrast, Kinect version 2 depth is based on TOF of intensity-modulated near-IR light sent by a laser projector [63].

Clinical applications of tracking systems include neurosurgery, orthopedic surgery, thoracoabdominal interventions and cardiovascular interventions [64]. In EBRT, tracking systems are used as follows:

- To verify patient set-up (OTS with two passive markers and several laser spots) [65].
- To assess internal organ motion during the treatment of, for example, prostate cancer. Organ displacements are tracked by implanting wireless electromagnetic transponders that are excited by an electromagnetic array (Calypso system, Varian Medical Systems, USA). This solution also includes an OTS for tracking that array [66].
- To activate the radiation beam based on either organ motion obtained from Calypso system [67] or respiratory phase acquired with real-time position management (RPM, Varian Medical Systems). In this last solution, a specific object with several passive markers (from two up to six) is placed on the patient's abdomen/thorax to obtain respiratory movements (OTS) [68, 69].

Finally, radioactive sources have been localised with an EMTS for real-time planning of IORT HDR brachytherapy [70].

4 FEASIBILITY OF INTEGRATING A MULTI-CAMERA OPTICAL TRACKING SYSTEM IN IOERT SCENARIOS

This chapter presents the specific study that assessed the feasibility of using a multi-camera optical tracking system to obtain the applicator pose in IOERT scenarios. This research was related to the first specific objective of this thesis and was published in *Physics in Medicine and Biology* journal [71].

4.1 INTRODUCTION

As previously mentioned in section 3.7, the actual IOERT treatment administered to the patient is not completely characterised. One of the unknown variables is the applicator pose in relation to the patient's anatomy that can be provided by a tracking system (section 3.9). An appropriate choice for IOERT scenarios (operating room [OR] with a multidisciplinary team) is an optical tracking system (OTS) due to its accuracy, wireless system, freedom of movements and working volume. To our knowledge, no studies have proposed this approach previous to the acceptance of our corresponding article [71]. Most OTSs make use of a relatively small number of cameras (two or three) [72, 73], thus reducing calibration requirements but limiting their practical use in complex clinical scenarios, where the required line-of-sight between the tracked objects and the cameras is easily obstructed. To overcome this limitation, we propose the use of a multi-camera OTS to ensure correct tracking of the applicator in a real IOERT setting, in which several actors and objects are moving around. Moreover, the applicator pose in relation to the patient's anatomy can be integrated in the treatment planning system (TPS) in order to generate an accurate description of the IOERT scenario.

This specific study had two objectives: first, to integrate a multi-camera OTS in the IOERT process, including the interaction with the IOERT planning system, and

second, to estimate the accuracy of the applicator pose in a phantom experiment that simulates three representative IOERT scenarios (breast, abdomen and rectum).

4.2 MATERIALS AND METHODS

This section describes the steps followed to obtain the position and orientation of the applicator in the treatment room with a multi-camera OTS (section *System description*) and the experiment designed to estimate the accuracy of the applicator pose (section *Experiments*). The tracking system was installed in the computed tomography (CT) simulation room, with a camera distribution similar to that used during a real treatment procedure. The gold standard for each IOERT scenario was generated by obtaining a CT study of the phantom, which simulated the patient's bone structure, and the applicator.

System description

This section describes the multi-camera OTS and the tools required for its integration in the IOERT planning system.

Optical tracking system

The OTS OptiTrack (NaturalPoint Inc., USA) provides real-time position and orientation (six degrees of freedom) of *rigid bodies* with passive optical markers (section 3.9) (Figure 18).

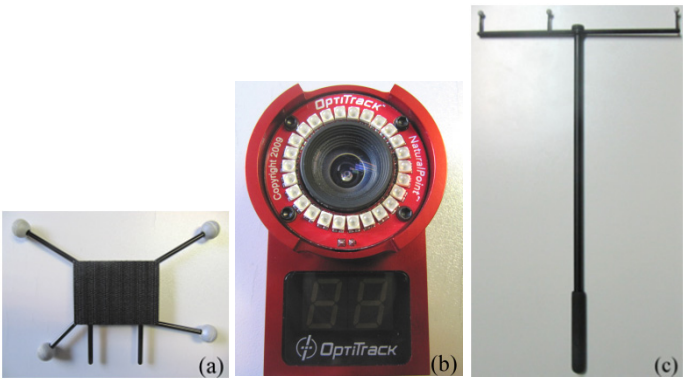

Figure 18. OTS: (a) rigid body with four spherical optical markers, (b) infrared (IR) camera, (c) three-marker 400-mm OptiWand used to calibrate camera parameters.

Eight synchronised cameras (model OptiTrack FLEX:V100R2, NaturalPoint Inc., Figure 18) with a resolution of 640 x 480 pixels (VGA) and maximum frame rate of 100 fps were placed around the scenario. This multi-camera approach covers a large working volume, thus making it well suited to the IOERT procedure.

Tracking Tools software (NaturalPoint Inc.) processes information captured by the near-IR cameras in order to determine the pose of any rigid body in the real world (*physical space*). We developed a software application that receives the data sent by Tracking Tools software via the virtual-reality peripheral network protocol [74] and determines the pose of any object to which a specific rigid body is attached.

Extrinsic camera parameters (physical position and orientation) and intrinsic camera parameters (focal length and lens distortion) were calibrated with a three-marker OptiWand (NaturalPoint Inc., Figure 18) and the three marker calibration algorithm (Tracking Tools software). The optical coordinate system is established by detecting a right scalene triangle on a flat surface with planar retro-reflective markers (area 1 x 1 cm) in its three corners (area 16 x 21 cm) placed in the working volume.

Pointer

To obtain the spatial position of landmark points in the physical space, we designed a specific tool called a pointer, which was a pencil-shaped rigid body made of polyoxymethylene (POM) (Figure 19) with a sharp tip (diameter 1 mm). Six spherical optical markers (diameter 1.2 ± 0.2 cm, mean ± standard deviation [SD]) were asymmetrically arranged around this tool in such a way that the distances between all the markers were pairwise different (at least the diameter of the markers). These conditions are required by the OTS to unequivocally recognise this rigid body [75].

The coordinates of the pointer tip in the physical space is obtained from equation (7),

$$\begin{bmatrix} x \\ y \\ z \end{bmatrix}_{tip} = R_{pointer} \begin{bmatrix} x \\ y \\ z \end{bmatrix}_{offset} + \begin{bmatrix} x \\ y \\ z \end{bmatrix}_{geometric\ centre} \quad (7)$$

where $R_{pointer}$ is a 3x3 matrix which specifies the rotation from the initial orientation of the pointer to its current one. The *offset* from the *geometric centre* of the six optical

markers to the pointer tip is obtained with a manual calibration procedure involving continuous recording of tracking data ($R_{pointer}$ and *geometric centre*) while the pointer is pivoted over its tip, which is inserted into a small hole. The *offset* and *tip* position are calculated by solving a system of equations which comes from re-writing equation (7) with the data collected [76].

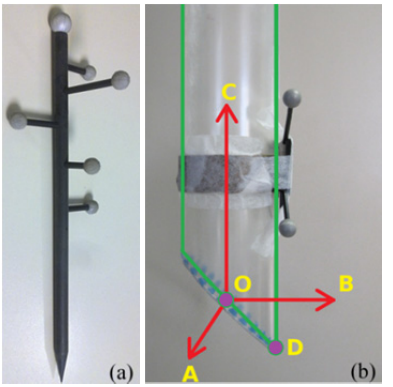

Figure 19. Optical tools: (a) pointer; (b) applicator, showing the trirectangular trihedron (vectors **OA**, **OB** and **OC**) used to fully characterise its pose. Point O is the bevel centre and point D represents the intersection of the bevel and the longer edge of the applicator. Vector **OC** is parallel to the longitudinal axis of the applicator, vector **OB** (bevel axis) points to the longer edge of the applicator and is perpendicular to vector **OC**, and vector **OA** is parallel to the cross product of vectors **OB** and **OC**. In order to unequivocally recognise the orientation of the trirectangular trihedron, the magnitude of **OB** is half of vector **OC**, and the magnitude of **OA** is a third of vector **OC**.

IOERT applicator

Another rigid body with a configuration of four spherical optical markers (diameter 1.1 cm, Hand Rigid Body, NaturalPoint Inc.) different from that of the pointer was attached to the IOERT applicator. The applicator pose in the physical space can be determined by applying an expression analogous to equation (7) to each point of the trirectangular trihedron OABC that fully characterises the applicator (Figure 19). It is also necessary to calibrate the applicator to obtain the *offset* from the *geometric centre* of the four optical markers to each point of the trirectangular trihedron (O, A, B and C). This calibration procedure is performed by using the pointer to locate the points O and D, and several small holes along the longitudinal axis of the applicator. Points A, B and C are determined by geometry. Each offset is then calculated by substituting the

position of each point (O, A, B and C) and the current pose of the rigid body in an expression analogous to equation (7).

Physical-to-image space registration

To integrate the OTS in the IOERT planning system, it is necessary to establish spatial concordance between the patient pose in the IOERT treatment room (real world or *physical space*) and the preoperative CT image in the IOERT planning system (virtual world or *image space*). The applicator pose from the physical space is converted into the image space by applying a transformation matrix calculated with a landmark rigid registration algorithm based on singular value decomposition [77]. This procedure requires at least three fiducial markers attached to the patient around the area of interest and visible on the CT image (Figure 20). Coordinates in the physical space are obtained by placing the tip of the pointer over each landmark. Coordinates in the image space are obtained from the patient's CT image with the aid of the orthogonal views and the volume rendering view of the IOERT planning system.

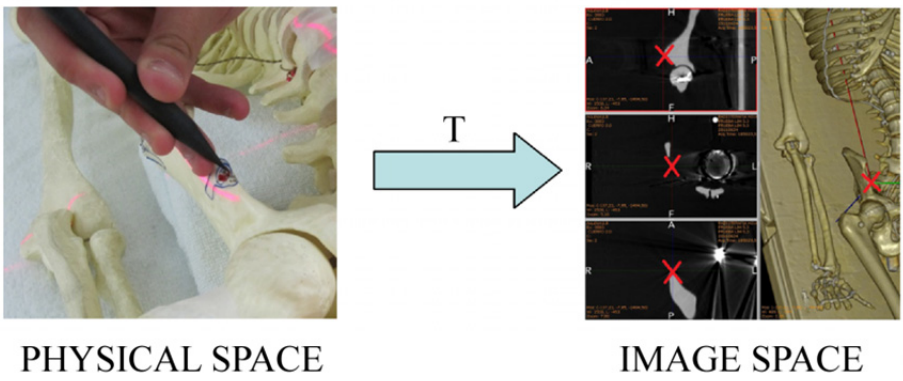

Figure 20. Physical-to-image space registration (transformation matrix *T*): selection of fiducial points in both spaces.

Experiments

This section describes the experiment carried out in the CT simulator room to estimate the accuracy of the applicator pose calculations. Three representative IOERT scenarios (breast, abdomen and rectum) were simulated using a plastic skeleton to simulate the patient's bone structure. The actual position and orientation of the applicator (gold

standard) for each scenario was obtained by performing a CT study of the phantom and the applicator together. Pointer accuracy was evaluated in a separate experiment.

Optical tracking system set-up

The cameras were statically attached to eight STOLMEN posts (Inter IKEA Systems B.V., Netherlands) around the table of a clinical CT system, following a U-shape configuration (Figure 21, area 6.84 m^2, mean height 2.65 m and mean distance between adjacent cameras 1.26 m). This distribution simulated the position of the cameras in the IOERT treatment room. The experiment was carried out in the CT room in order to be able to generate the gold standard or actual applicator pose from the CT acquisition.

Figure 21. OTS set-up for the experiment: IR cameras and three-marker OptiWand used to calibrate the cameras.

IOERT applicator set-up

The IOERT applicator used in this study was a polymethyl methacrylate (PMMA) tube measuring 7 cm in diameter with a bevel angle of 45º. Depending on the IOERT scenario, this device was placed on the region of interest (ROI) using an articulated arm that firmly attached the applicator to the CT scanner bed (Figure 22, Figure 23 and Figure 24).

Metallic wires measuring 0.8 mm in diameter (SL-W8, The Suremark Company, USA) were attached to the longitudinal axis of the applicator and the contour of the bevel in

order to better determine its position and orientation from the CT image. The actual applicator pose in the image space was calculated by segmenting those metallic wires from the CT image by histogram thresholding. The metallic wire over the longitudinal axis was then adjusted to a line parallel to the vector **OC** (Figure 19) using a method based on principal component analysis [78], and an ellipse was adjusted to the coordinates of the metallic wire on the contour of the bevel using an algorithm based on least squares fit [79]. The quality of the fitting was assessed by calculating the root mean square (RMS) error between the coordinates of the segmented points and the closest points in the adjusted line and ellipse. Finally, points O, A, B and C (Figure 19) were determined by geometry.

Phantom

The plastic skeleton was placed on the table of the clinical CT system in the same position for all the IOERT scenarios, and close to the centre of the field of view (FOV) of the cameras. Six metallic nipple markers (diameter 1.5 mm, SL–15, The Suremark Company), which are routinely used to identify reference landmarks in CT scans, were placed on the skeleton around each ROI and used as fiducial points for the physical-to-image space registration. The coordinates of these markers in the physical space were obtained by placing the pointer on the marker surface and in the image space by calculating the centroid of each one. Five spherical optical markers (diameter 1.1 cm, NaturalPoint Inc., same locations for the three IOERT scenarios) were also attached to the skeleton. The physical positions of these landmarks are not affected by pointer or operator error, as their centroids were obtained directly from the OTS.

CT acquisition

CT studies were acquired on a CT simulator (Toshiba Aquilion™ Large Bore scanner, Japan) with the acquisition parameters shown in Table 1.

Evaluation

- *Pointer accuracy*

Pointer accuracy was estimated by placing the tip of the pointer in 17 different locations on a millimetre board (17 x 17 cm), located at the centre of the FOV of the

cameras and 1 m away from that centre. Pointer accuracy was assessed as the RMS error between the position of the pointer tip provided by the OTS and its actual position from the millimetre board.

Table 1. CT acquisition parameters.

	Voltage (kVp)	Exposure (mAs)	Matrix size	Voxel size (mm)
Breast	120	21 ± 2[a]	512 x 512 x 363	1.5 x 1.5 x 2.0
Abdomen	120	20 ±1[a]	512 x 512 x 448	1.6 x 1.6 x 2.0
Rectum	120	30	512 x 512 x 462	1.3 x 1.3 x 2.0

[a] Mean ± SD.

- *IOERT applicator pose accuracy*

The accuracy of the applicator pose was assessed by comparing the actual value obtained from the CT image with the virtual one provided by the OTS. The experiment was designed to evaluate two sources of error in the physical space: the pointer and the operator. For this purpose, two groups of measurements were taken: one where the operators manually selected the metallic markers and the other automatically tracking the optical markers.

The details of the protocol used in each IOERT scenario (breast, abdomen and rectum) are as follows:

1. The metallic markers were attached to the skeleton around the ROI (different distribution for each IOERT scenario) and the applicator was placed close to the phantom.
2. The applicator and both metallic and optical markers were located in the physical space with the OTS. The position of the metallic markers was identified with the pointer three times by different operators in order to assess operator variability (reproducibility component). The applicator pose was also collected three times with the OTS (repeatability component).

3. A CT scan was acquired with a FOV covering the volume of the skeleton under study, ensuring that it included the metallic and optical markers, and the applicator.
4. Step 2 was repeated after the CT scan in order to check the stability of the experiment.
5. The centroids of both metallic and optical markers were calculated from the CT image, and their coordinates were matched to those obtained from the OTS, thus providing a rigid registration from the physical space to the image space. The fiducial registration error (FRE [80]) of each registration was calculated as the RMS distance between the transformed markers of the physical space and the markers of the image space (homologous markers after registration).
6. The actual pose of the applicator related to the skeleton was estimated from the CT image (section *IOERT applicator set-up*). Its virtual pose was calculated by applying each registration (step 5) to the corresponding data of the applicator in the physical space (steps 2 and 4).
7. The positioning error was estimated by the Euclidean distance between the coordinates of the bevel centre of the actual applicator and the virtual applicator. The orientation errors were assessed by the angle between the bevel axis **OB** (and the longitudinal axis **OC**) of the actual applicator and the virtual applicator.

4.3 RESULTS

The estimation of the extrinsic and intrinsic camera parameters yielded an overall OptiWand error of 0.173 ± 0.024 mm (mean ± SD, data provided by the Tracking Tools software).

Pointer accuracy

The RMS error of the pointer tip was 1.7 mm (SD of the error 0.5 mm) at the centre of the FOV of the cameras and 2.2 mm (SD of the error 0.3 mm) at a distance of 1 m.

This error was close to the diameter of the tip (1 mm) and was significantly higher 1 m away from the centre of the FOV ($p < 10^{-3}$, Student's t-test, paired sample, N=17).

IOERT applicator pose accuracy

As no statistically significant differences were detected in the results depending on whether the position of the markers was obtained before or after the CT scan, both data sets were pooled. Table 2 shows the FRE of the rigid registration between the transformed markers of the physical space and the markers of the image space. The metallic wires of the applicator (longitudinal axis and contour of the bevel) were adjusted yielding an RMS error of 1.4 ± 0.3 mm (calculated as described in section *IOERT applicator set-up* [section 4.2]).

Table 3 shows the pose errors between the actual applicator and the virtual applicator. The mean errors were 1.8 mm for the bevel centre, 1.6º for the bevel axis and 0.7º for the longitudinal axis. Figure 22, Figure 23 and Figure 24 illustrate the applicator pose in the physical space for the breast, abdomen and rectum IOERT scenarios respectively, and also the pose of the actual applicator and the virtual applicator in the IOERT planning system. Most of the variance of the applicator error (without factor scenario) can be attributed to the inter-observer variability of the marker locations in the physical space (reproducibility component) while the repeatability component related to the OTS was negligible (data not shown). As an example, the variance components analysis of the bevel axis error yielded an estimated variance of the repeatability component of 3.5 x 10^{-6} mm^2 for the abdomen scenario and using the data collected after the CT scan.

Table 2. FRE[a] between homologous markers after registration.

	FRE (mm)
Metallic markers[b]	1.3 ± 0.4[*]
Optical markers[b]	0.8 ± 0.2[*]

[a] Mean ± SD.
[b] Average of breast, abdomen and rectum scenarios.
[*] $p < 0.001$ (Student's t-test, paired sample).

Table 3. Positioning and orientation errors[a] between homologous markers after registration.

	Bevel centre (mm)	Bevel axis (º)	Longitudinal axis (º)
IOERT scenarios[b]	1.8 ± 0.5	1.6 ± 0.5	0.7 ± 0.3
Breast[c]	1.4 ± 0.3	2.0 ± 0.3	0.4 ± 0.2
Abdomen[c]	2.0 ± 0.5	1.4 ± 0.1	1.0 ± 0.1
Rectum[c]	1.9 ± 0.4	1.1 ± 0.2	0.9 ± 0.2
Metallic markers[d]	1.9 ± 0.5*	1.6 ± 0.5	0.7 ± 0.3
Optical markers[d]	1.4 ± 0.3*	1.5 ± 0.3	0.6 ± 0.2

[a] Mean ± SD.
[b] Average of all data.
[c] Average of metallic and optical markers data.
[d] Average of breast, abdomen and rectum scenarios.
* $p < 0.03$ (Student's t-test, paired sample).

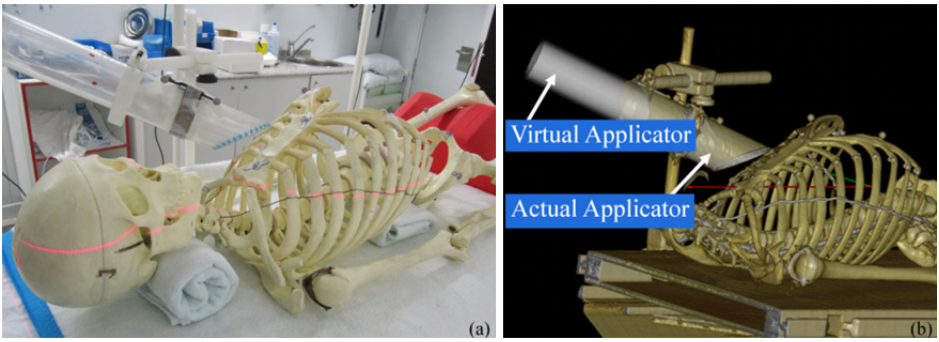

Figure 22. Breast IOERT scenario: (a) applicator and skeleton (physical space), (b) actual applicator and virtual applicator on the volume rendering of the skeleton (image space).

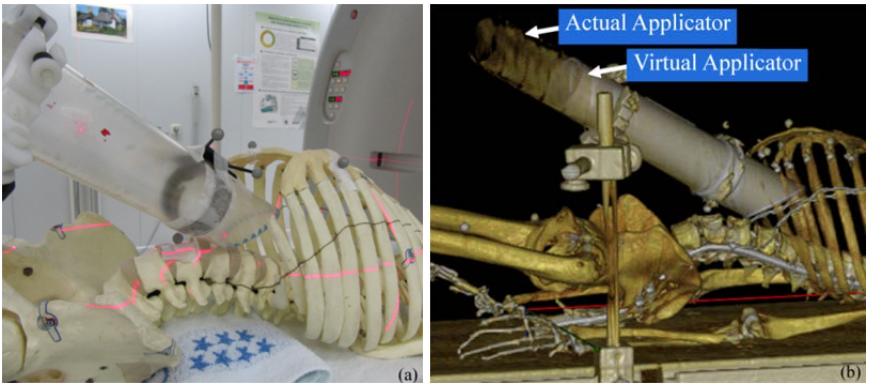

Figure 23. Abdomen IOERT scenario: (a) applicator and skeleton (physical space), (b) actual applicator and virtual applicator on the volume rendering of the skeleton (image space).

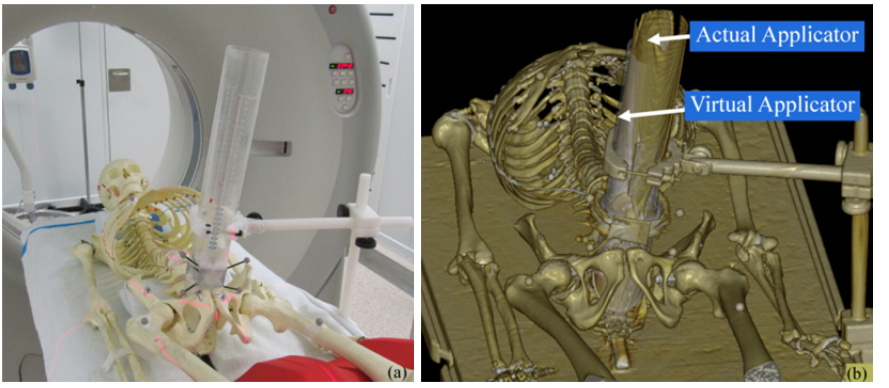

Figure 24. Rectum IOERT scenario: (a) applicator and skeleton (physical space), (b) actual applicator and virtual applicator on the volume rendering of the skeleton (image space).

4.4 DISCUSSION

In this study, a multi-camera OTS was integrated for the first time in the IOERT procedure, specifically into the radiance TPS, in order to further evaluate the actual dose distribution in the patient. We assessed the accuracy of the IOERT applicator pose in an end-to-end experiment resembling real treatment scenarios that were selected according to the most common intraoperative radiation therapy (IORT) sites (breast 31.8%, abdomen 29% and rectum 19.6% [18], this tendency has recently been confirmed by European expert institutions [22]) (Figure 25). Our results included

several sources of error involved in the real process: calibration of the optical tools, intrinsic optical system limitations and point-to-point registration with user interaction.

The IOERT multidisciplinary staff and the use of several surgical support devices might easily obstruct the line-of-sight between tracked objects and the OTS if few cameras are used, thus seriously degrading tracker performance. Our solution makes use of more cameras to overcome these occlusion problems, as they are arranged around the working volume. In [81], the authors reported the use of the Vicon MX visual-tracking system (Vicon Motion Systems, USA) with five near-IR cameras on the walls of a single photon emission computed tomography (SPECT) room. This study showed sub-millimetric accuracy for motion tracking during cardiac SPECT imaging, with every optical marker on the patient localised at least 84% of the time, and emphasised the flexibility of camera placement to improve marker viewing.

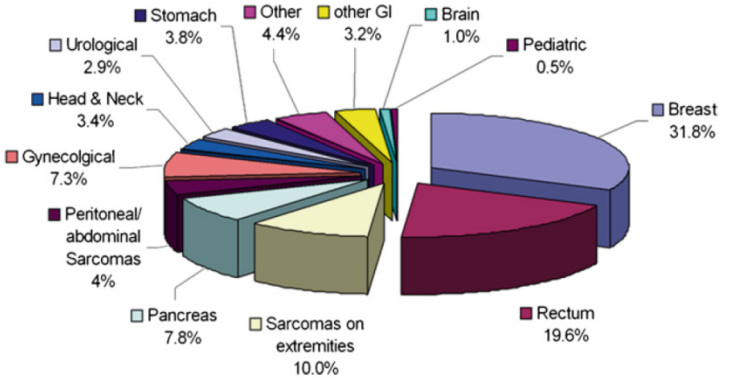

Figure 25. Frequency of IORT sites in Europe (ISIORT-Europe 2004 survey). GI (gastrointestinal). Source [18].

As the pointer is a key tool in this experiment, we first estimated its accuracy (between 1.7 and 2.2 mm). In [72], the authors reported that the accuracy of the location of individual optical markers with OTSs (typically 0.25 mm) is better than when using tool tips (up to 2 mm), in accordance with our results. Although the use of a pointer to manually select reference positions could seem suboptimal, it is essential in practice for registration and navigation in certain scenarios, such as the tumour bed, where placing a marker might not be feasible.

Regarding the articulated arm that attached the applicator to the CT scanner bed, we demonstrated that the applicator was held steady throughout the process, including the CT acquisition, since errors before and after the acquisition were statistically equivalent.

The physical-to-image space registration was performed with an FRE of 1.3 ± 0.4 mm. This result includes inter-operator variability. FRE was also calculated for registrations with optical markers, which are not affected by pointer error, and proved to be 0.8 ± 0.2 mm. This latter error was slightly better, although both results are within the slice thickness of the CT images. Both solutions could be used in the IOERT scenarios we describe, although the pointer and the metallic markers (or other anatomical landmarks) are a more flexible solution, given the limitations in the radio-surgical treatment theatre. The physical-to-image space registration for this solution was obtained using six metallic markers. In external beam radiation therapy (EBRT), the patient is commonly positioned by aligning three skin markers (minimum number to establish spatial concordance) with in-room lasers [82]. If one of these three markers is mislocated, the registration becomes biased. In our case, we would recommend the use of a minimum number of four markers. A large FRE in any marker may indicate a local displacement in that area, and in that case the best three markers could be selected for the alignment. Another source of error is the uncertainty in the localization of the marker centroids in the CT image. However, decreasing voxel size might not significantly improve the results as the registration error is also affected by the pointer accuracy, and consequently the increase in radiation dose for the patient would not be justified.

The integration of the OTS in the IOERT planning system is illustrated in the figures that show the fusion of the actual applicator and the virtual applicator. Our accuracy results for the applicator pose could be evaluated using the recommendations from Task Group 147 (TG–147, commissioned by the Therapy Committee and the Quality Assurance and Outcomes Improvement Subcommittee of the AAPM to study the localization accuracy with non-radiographic methods such as IR systems in EBRT [73]). According to TG–147, when the phantom used to perform the daily quality assurance is positioned at the treatment isocentre based on the room lasers, the non-

radiographic system should localise the phantom within 2 mm of that location [73]. In our experiment, the accuracy of the applicator pose was below 2 mm in position (mean error of the bevel centre) and 2º in orientation (mean error of the bevel axis and the longitudinal axis), which corresponds to 1.8 mm (the arc length along the bevel of the 7-cm–diameter applicator [83]). These measurements are small when compared to the diameter of the IOERT applicator (7 cm), and within the acceptable range proposed in the TG–147 recommendation. The fact that the positioning error of the applicator is slightly higher with the metallic markers than with the optical ones suggests that this discrepancy could be due to pointer error. This difference (0.5 mm on average) is similar to the FRE between both types of markers. However, the coordinates of the metallic and optical markers in the physical space were obtained following a different methodology, namely, by placing the pointer on the surface of each metallic marker and by assessing the centroid of each optical marker. Therefore, the discrepancy may also be attributed to the procedure of the marker location in the physical space, since the radius of the metallic markers (0.75 mm) is close to the difference in the positioning error of the applicator.

Our results represent a major step towards the use of this approach in IOERT. However, some issues still need to be addressed. Although the experiment described makes use of one post for every camera, the final set-up in the IOERT treatment room could take advantage of a tubular structure hanging from the ceiling to which the cameras could be easily attached in positions similar to those evaluated. Moreover, the rotation of the cameras would be adjusted in order to better cover the FOV of the IOERT treatment. The clinical installation would be checked by means of repeating the experiments described in this work. The whole setting (the phantom and the applicator) would be carefully transferred from the IOERT treatment room to the CT simulator room by means of a CT compatible transport bed [84] in order to acquire the gold standard. Accuracy of the applicator pose would be similar in the IOERT room, except for the occlusion problems caused by, for instance, operating theatre personnel and anaesthetic and laparoscopic instruments. This limitation has been partially evaluated because our results were obtained in a scenario in which the operator blocked the view of some cameras while using the pointer. Degradation of tracker performance in the

IOERT treatment room is likely to be low, since the applicator is correctly tracked if its rigid body is well designed and at least three optical markers are seen by at least two out of the eight cameras in the OTS (stereo vision). In fact, the cameras are placed surrounding the scenario in order to reduce occlusions. Nevertheless, a figure of merit of the tracking process would be useful for the interactive assessment of the data collected by the multi-camera OTS. SD of the collected position, the number of optical markers of the pointer or the applicator actually seen and the number of cameras occluded would be taken into account in this figure of merit. On the other hand, as the skeleton phantom represents an idealised and simplified patient, the accuracy of the applicator pose achieved in our experiment may be considered to be a lower limit. The real treatment procedure will introduce several factors, such as retraction of structures, removal of affected tissues, internal organ displacement and placement of protections, which require further study. In addition, these issues could modify the geometry of the surgical site and increase the difference with the preoperative image used to plan the radiation treatment. Conventional preoperative CT imaging of the patient in a position resembling the surgical operation could decrease these dissimilarities. A better solution would be to use intraoperative imaging, which offers updated anatomical information [85]. To this end, a mobile C-arm that provides cone-beam CT (CBCT) imaging capability, but with a limited FOV, has been proposed [86, 87]. Such a solution would enable IOERT dosimetry planning to be more easily adapted to a real scenario after physical-to-image space registration. Regarding the protections, the tip of a sterilised pointer could be used to delimit the contour of the shielding plates in the surgical site in order to obtain its position in relation to the applicator pose, provided the handle of the pointer where the optical markers are placed is visible.

4.5 CONCLUSIONS

We evaluated the accuracy of IOERT applicator pose with a multi-camera OTS by means of a phantom study. The results of this experiment, which was designed to simulate real treatment scenarios, reveal positioning and orientation errors below 2 mm. This lower limit encourages us to evaluate the feasibility of this approach in

further clinical studies. The virtual applicator integrated in an IOERT planning system allows the radiation oncologist to better estimate the real IOERT dose delivered to the patient during the procedure and, consequently, will benefit the radiotherapy response assessment.

5 COMPARISON OF PREOPERATIVE AND INTRAOPERATIVE CT IMAGES FOR IOERT DOSE ESTIMATION

This chapter introduces the specific study that assessed the feasibility of acquiring intraoperative computed tomography images in real IOERT scenarios. These intraoperative studies were used to evaluate the improvement achieved in the dose distribution estimation when compared to that obtained from preoperative CT images, identifying the dominant factor in that estimation. This research was related to the second objective of this thesis. Preliminary results of this study were presented in the *American Society for Radiation Oncology (ASTRO)* conference [85].

5.1 INTRODUCTION

Patient position, surgical access, tumour resection and IOERT treatment set-up in the actual IOERT field can differ from those simulated in the treatment planning system (TPS). Intraoperative images of the actual scenario during the treatment would be useful not only for intraoperative planning but also for registering and evaluating the treatment administered to the patient. Actual IOERT dose distributions would also enable calculating dose accumulation when external beam radiation therapy (EBRT) is applied after an IOERT boost.

As previously mentioned in section 3.6, surface irregularities can significantly affect the IOERT dose distribution. In [12], the authors simulated some characteristic pelvic IOERT scenarios (rectal cancer) with solid water slabs and radiotherapy bolus and showed that curved irradiation surfaces caused dose distributions to be curved and deeper than those with flat surfaces. Moreover, a cavity smaller than the applicator produced hot spots close to the surface followed by a fast dose reduction. In a previous work [85], our group evaluated the difference between the 3D dose distributions obtained with preoperative computed tomography (CT) images and their corresponding

intraoperative CT images acquired during the IOERT. An average dose difference of 5% was found after applying some preprocessing in the preoperative images, namely removal of the tumour and its surrounding tissues as expected during surgery and then deformable registration to the intraoperative studies. The average dose difference increased to 10% when using rigid alignment instead of deformable registration. This evaluation was carried out just in two clinical cases (Ewing and undifferentiated sarcoma) and did not take account of distance-to-agreement (DTA) concept as does the gamma index [38], which is the mainstay of dose distribution comparisons in medical physics (section 3.5).

In this specific study, we aimed to assess the feasibility of acquiring intraoperative CT images in real IOERT scenarios extending the number of cases and IOERT sites presented in [85]. We also compared the 3D dose distributions estimated with intraoperative CT images (gold standard) to those obtained under the assumption of having just water at the end of the applicator (conventional assumption), tissue heterogeneities (data from their corresponding preoperative CT images) or adding an air gap at the end of the applicator. The comparisons were done in terms of gamma criteria. With this approach, we assessed if dose estimation on preoperative images is a good predictor of the intraoperative case, identifying the dominant factor in that estimation.

5.2 MATERIALS AND METHODS

In this section, we describe the IOERT cases evaluated in this study, the protocol used to acquire the preoperative and intraoperative CT images, the processing done in these images and the details of the dose distribution estimation with the comparisons carried out.

IOERT cases

Six patients undergoing IOERT were enrolled for this study. Informed consent was obtained from all patients. The diagnosis of each patient and the parameters of their radiotherapy treatment are detailed in Table 4. The study included several IOERT sites.

In both breast cancer cases, a shielding disc was used to protect intrathoracic organs during irradiation. These shielding discs were made of lead with a diameter of 6 cm (1 cm larger than the applicator diameter) and thickness 3 mm. Surgical retractors made of stainless steel were included in the retroperitoneal case.

Table 4. IOERT parameters.

	Applicator diameter (cm)	Bevel angle	Energy (MeV)	90% isodose (Gy)
Patient 1 (Ewing sarcoma)	8	15º	6	10
Patient 2 (Rhabdomyosarcoma)	12	30º	8	12.5
Patient 3 (Breast cancer, right)	5	30º	6	10
Patient 4 (Breast cancer, left)	5	0º	6	10
Patient 5 (Retroperitoneal sarcoma)	10	30º	8	12.5
Patient 6 (Chondrosarcoma)	7	30º	8	12.5

Protocol description

The conventional IOERT protocol included patient's transfer from the operating room (OR) to the LINAC room (bunker) for irradiation. This transfer was necessary since a dedicated mobile LINAC to be used inside the OR was not available. In this study, preoperative CT images for those six patients were acquired on an Aquilion™ Large Bore CT simulator (Toshiba, Japan; Patient 1, 2 and 6), on an MX8000 CT (Philips, The Netherlands, Patient 3 and 4) and on a Brilliance 16 CT (Philips, Patient 5). The IOERT protocol was modified as follows in order to incorporate the acquisition of an intraoperative CT image of the actual IOERT scenario:

1. The patient lay on a rigid radiotransparent subtable that was placed over the operating table during the surgery. The use of this subtable did not allow removing or individually moving the different segments of the surgical table.
2. After tumour resection, the IOERT applicator was placed on the tumour bed and was firmly attached to that radiotransparent subtable with an articulated arm.
3. The patient was covered to maintain asepsis of the surgical field during the transfer to the CT simulator room and the treatment room. A subtable stretcher, similar to that presented in [84], allowed carrying the subtable from the operating table to the CT/LINAC table. The radiotransparent subtable and the subtable stretcher were manufactured for this study.
4. An intraoperative CT image of the whole setting (patient and applicator) was acquired on a Toshiba Aquilion™ Large Bore CT simulator.

After these steps, the conventional protocol was followed: the patient was transferred to the LINAC room for tumour bed irradiation and then to the OR for surgical closure.

All the involved facilities (OR, CT simulator and LINAC treatment unit) were located in the Radiation Oncology Service at Hospital General Universitario Gregorio Marañón (Madrid, Spain). Patients were under general anaesthesia during the whole procedure. No decisions regarding IOERT parameters (beam energy and prescribed dose) were taken based on this intraoperative data. Table 5 includes the CT acquisition parameters of the preoperative images and intraoperative images, and the temporal interval between both image studies.

Image processing

Image registration

Each preoperative image was rigidly registered to its corresponding intraoperative image. This enabled us to calculate the dose distribution in both preoperative and intraoperative images under the assumption of having the same applicator pose in relation to the patient's anatomy. This step focused on aligning bones to facilitate the registration process and was done after the following preprocessing. Firstly, all

preoperative and intraoperative images were resampled to 1.5-mm isotropic voxel size to facilitate further comparisons. After that, all images were translated to place the region of interest (ROI), namely the tissues close to the applicator bevel, in the image centre and were also cropped to remove tissues that could hinder the registration. Then, masks were obtaining by segmenting the bones close to the applicator bevels using region growing method and manual frontiers. Finally, segmented images were created by using those masks so that the background was set to zero and bones were set to their original CT values. Each segmented preoperative image was rigidly aligned with its corresponding segmented intraoperative image using normalised mutual information as cost function. Each registration parameters (3 translations and 3 rotations) were then applied to the corresponding translated and cropped preoperative image.

Table 5. CT acquisition parameters.

	Days between images	Voltage (kVp)	Exposure (mAs)	Matrix size	Voxel size (mm)
Patient 1 (Ewing sarcoma)	6	120	35 ± 7[a,b] 125[c]	512 x 512 x 117[b] 512 x 512 x 201[c]	1.3 x 1.3 x 5.0[b] 1.3 x 1.3 x 2.0[c]
Patient 2 (Rhabdomyosarcoma)	1	120	125	512 x 512 x 238[b] 512 x 512 x 227[c]	1.1 x 1.1 x 2.0[b] 1.6 x 1.6 x 2.0[c]
Patient 3 (Breast cancer, right)	17	120	100[b] 127 ± 66[a,c]	512 x 512 x 221[b] 512 x 512 x 129[c]	0.6 x 0.6 x 1.6[b] 1.3 x 1.3 x 3.0[c]
Patient 4 (Breast cancer, left)	9	120	100[b] 114 ± 27[a,c]	512 x 512 x 238[b] 512 x 512 x 58[c]	0.7 x 0.7 x 1.6[b] 1.1 x 1.1 x 5.0[c]
Patient 5 (Retroperitoneal sarcoma)	1	120	196 ± 22[a,b] 217 ± 7[a,c]	512 x 512 x 630[b] 512 x 512 x 218[c]	0.7 x 0.7 x 1.0[b] 1.4 x 1.4 x 2.0[c]
Patient 6 (Chondrosarcoma)	0	120	132 ± 62[a,b] 144 ± 54[a,c]	512 x 512 x 435[b] 512 x 512 x 193[c]	1.2 x 1.2 x 2.0[b] 0.9 x 0.9 x 2.0[c]

[a] Mean ± standard deviation (SD).
[b] Preoperative CT image.
[c] Intraoperative CT image.

Air gap segmentation

From the point of view of the electron beam (beam's-eye view), a difference between preoperative images and intraoperative images is the air between the end of the applicator and the tumour bed. Another preoperative image was created following the subsequent steps to take account of this aspect in the comparison of IOERT dose distributions. Firstly, the air gap between the end of the applicator and the tumour bed was segmented in each transformed intraoperative CT image (the one translated and cropped) using region growing method (maximum limit –500 HU) and manual frontiers. This segmentation was restricted to the bevel and along the geometric axis of the applicator since excision cavities could be larger. Then, each inverted mask was applied to its corresponding registered preoperative image so that the background (air) was set to the CT value of air (–1000 HU) and tissues were set to their original CT values.

Applicator pose identification

The transformed intraoperative CT images enabled us to estimate the applicator pose (position of the bevel centre and rotation of the applicator relative to its initial orientation in the TPS) as their field of view (FOV) covered the irradiated tissues and the applicator. The drawback is that CT values of the applicator are similar to those of soft tissues so the following semiautomatic method was used to estimate the applicator pose in each transformed intraoperative image. Firstly, some specific regions of the applicator were segmented using region growing method and manual frontiers. These masks were used to calculate the two angles that aligned the geometric axis of the applicator with the axial axis of each transformed intraoperative CT image. This is the initial orientation of the applicator in the TPS except for the rotation around the geometric axis of the applicator. After that alignment, a short cylinder of the applicator was segmented using region growing method. The coordinates X and Y of the bevel centre were estimated by averaging the centres of the circumferences adjusted to every axial slice of that mask. Next, the end of the shorter edge (applicator) was manually located in the corresponding axial slice of each transformed intraoperative CT image and this information was used to calculate the coordinate Z of the bevel centre. After

that, a virtual applicator with the diameter and bevel angle specific to that IOERT case and with the initial orientation in the TPS was superimposed on each transformed intraoperative image. Its position was set according to the bevel centre estimated. Then, this virtual applicator was manually rotated around its geometric axis until matching the one depicted in each transformed intraoperative image. This step provided the third rotation of the applicator. Finally, the coordinates of the bevel centre and the three rotations obtained in the whole process were accordingly transformed to build the matrix that defined the pose of the virtual applicator in the TPS related to the initial one.

IOERT dose distributions

IOERT cases were simulated with radiance TPS (GMV, Spain) [3] using the registered preoperative images (without air gap [preCT] and with air gap [$preCT_{air}$]) and the transformed intraoperative images of each patient (intraCT).

The relationship between HU and density was entered into the IOERT TPS before calculating any dose distribution. This calibration curve was obtained by using a CT of an electron density phantom (model 062, CIRS Inc., USA) acquired in the same scanner as in the case of the preoperative/intraoperative images. The stoichiometric calibration [55, 56] was done to take account of that the electron density phantom is made of tissue-equivalent materials that represent the densities of tissues but do not usually replicate their chemical composition (section 3.8 and section *Conversion of the CT number to physical density* [section 6.2]).

The IOERT parameters (applicator diameter, bevel angle and energy) shown in Table 4 were introduced in the TPS. The energy of the sixth IOERT case (8 MeV) was replaced with 9 MeV as the TPS did not include this energy for the applicator used in that treatment (diameter 7 cm and bevel angle 30º). In each image, a virtual applicator was placed in the same pose as depicted in the intraCT by using the transformation matrix obtained in section *Applicator pose identification*. The tissue inside the applicator was set to the CT value of air automatically by the TPS. Dose distributions were calculated with the registered preoperative images (preCT and $preCT_{air}$) and the transformed intraoperative images (intraCT) of each patient using pencil beam algorithm (resolution

1.5 mm) [49, 88] and Monte Carlo algorithm (error tolerance 1%, resolution 1.5 mm) [50] specifically adapted for IOERT. Another dose distribution was also estimated from each registered preoperative image (without air data) by selecting Water option ($preCT_{water}$). This choice allows calculating the dose without taking into account tissue heterogeneities, just assuming water at the end of the applicator. Doses were not scaled to a normalised value (100% corresponded to the maximum dose along the clinical axis when using a water phantom, the same applicator diameter, bevel 0º, the same energy and a specific source-to-surface distance [measurements for modelling treatment unit]).

Dose distributions calculated from preoperative images ($preCT_{water}$, preCT and $preCT_{air}$) were compared with that estimated with their corresponding intraoperative image (intraCT) in terms of the gamma index (section 3.5). Since no values have been established for IOERT, we used a 3D gamma criteria of 3%/3 mm and 5%/2 mm for dose values greater than either 10% or 70% (to focus on high dose regions). The acceptance criteria 5%/2 mm includes a tighter distance tolerance that could be more appropriate for the characteristic dose distribution of electron beams (mainly dose decreases below 10% after only a few centimetres). The dose distributions obtained from the intraoperative images were considered the gold standard as these images represented the patient anatomy just before the irradiation. A mask obtained by segmenting the tissue in each intraCT with region growing method (minimum limit –700 HU for Patient 1 and –625 HU for Patient 2 and Patient 6) and manual frontiers was applied in the 3D gamma analyses to remove dose differences of regions not belonging to each patient.

5.3 RESULTS

The six patients underwent IOERT following the described protocol and there were no complications in the whole procedure related to the transport step using the subtable and its stretcher or the acquisition of intraoperative CT images (for example, anaesthetic stability or other clinical relevant observations).

Dose distributions were not calculated in three cases (Patient 3, 4 and 5) since there were metal artefacts (severe streaking) that substantially modified the HU of the

intraoperative images. These artefacts were due to metallic objects such as the shielding discs in the breast cancer cases (Figure 26 and Figure 27) and surgical retractors in the retroperitoneal case (Figure 28). In the intraoperative images of both breast cancer cases, there were dark streaks along the radial axis of the shielding discs and bright streaks along its perpendicular axis. For instance, the bright streak in Figure 27 was about 36 mm, one order of magnitude larger than the thickness of the shielding disc. The contralateral breast allowed checking the proper range of CT values corresponding to the involved tissues. In the case of the third patient, the applicator was not firmly attached and it moved during the transfer to the CT room. Its intraoperative image showed that the shielding disc was not aligned with the applicator (Figure 26). The applicator pose was corrected before irradiation in that IOERT case.

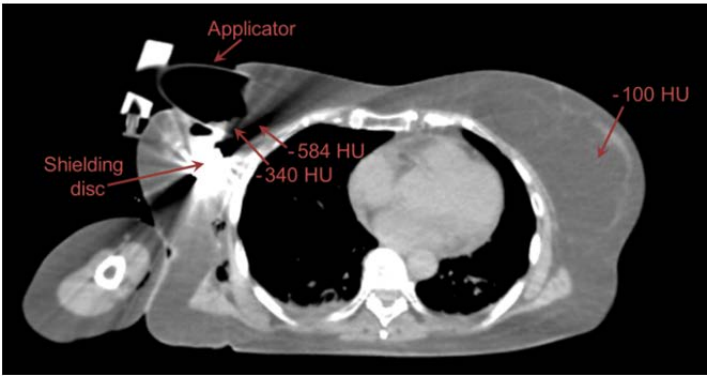

Figure 26. Patient 3's intraoperative image (breast cancer, right).

Figure 27. Patient 4's intraoperative image (breast cancer, left).

Figure 29, Figure 30 and Figure 31 illustrate the alignment between the preoperative CT images and the intraoperative CT images. The registration was focused on aligning the bones close to the applicator bevel and this step was checked by visual inspection. The other bones and some soft tissue did not perfectly match due to the rigid registration. Figure 32 shows the alignment between the virtual applicator and that shown in each intraoperative image. The pose of the virtual applicator was obtained following the semiautomatic method explained in section *Applicator pose identification* (section 5.2). The maximum distances from the end of the applicator to the tumour bed were 30.5 mm (Patient 6), 14.5 mm (Patient 1) and 8.5 mm (Patient 2), (Figure 33).

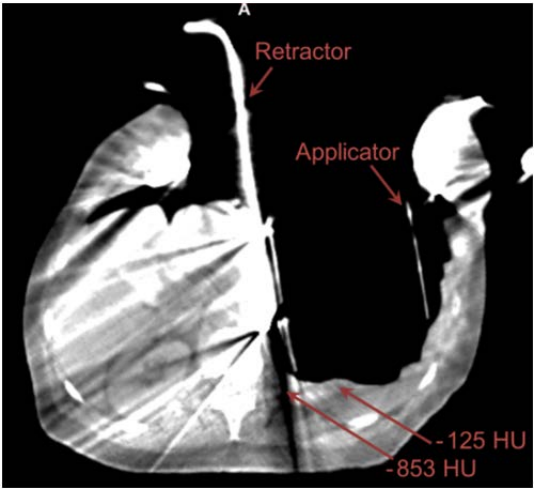

Figure 28. Patient 5's intraoperative image (retroperitoneal sarcoma).

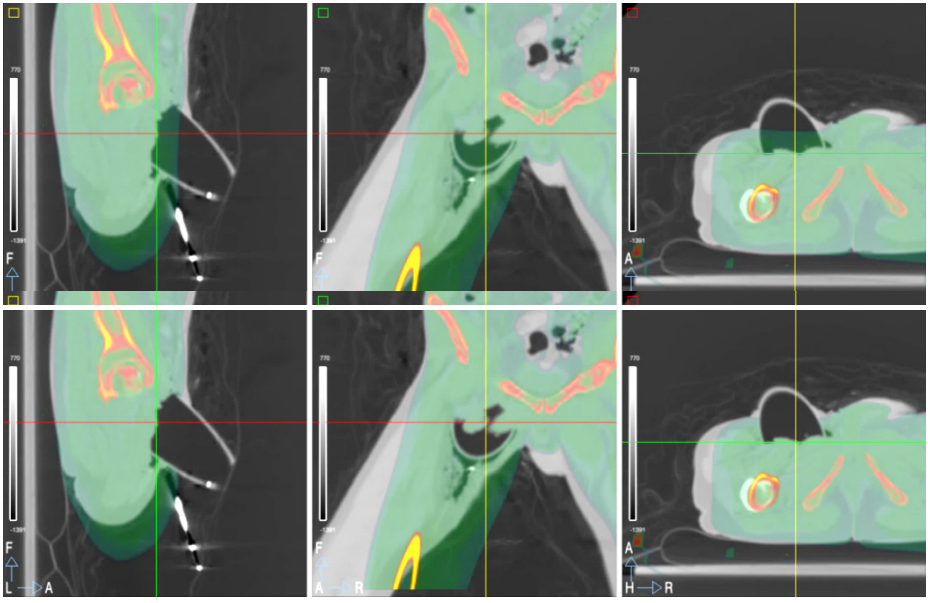

Figure 29. Registered images (Patient 1, Ewing sarcoma). Preoperative image (colour) superimposed on its intraoperative image (greyscale). PreCT (top) and preCT$_{air}$ (bottom). From left to right, sagittal view, coronal view and axial view.

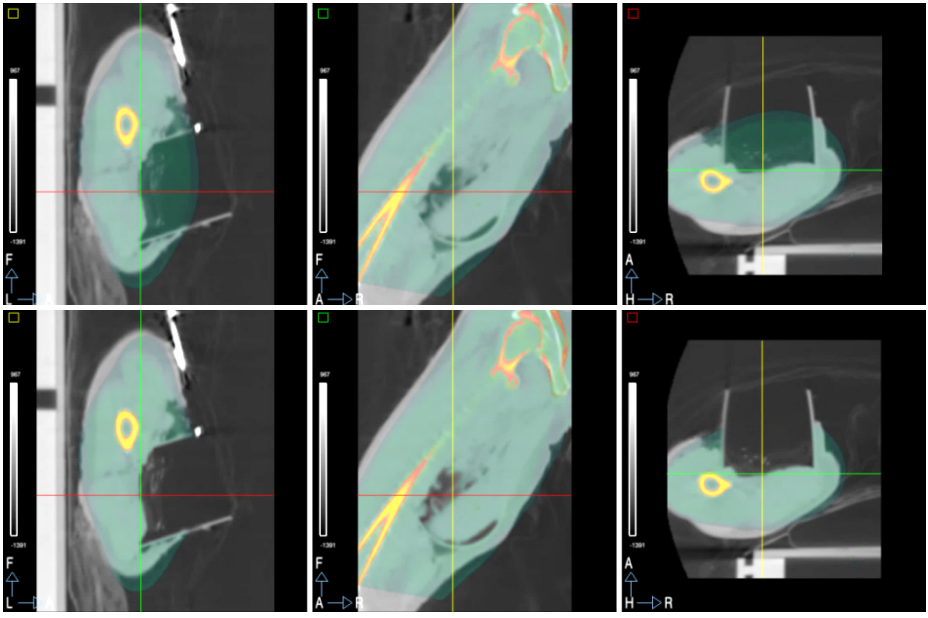

Figure 30. Registered images (Patient 2, rhabdomyosarcoma). Preoperative image (colour) superimposed on its intraoperative image (greyscale). PreCT (top) and preCT$_{air}$ (bottom). From left to right, sagittal view, coronal view and axial view.

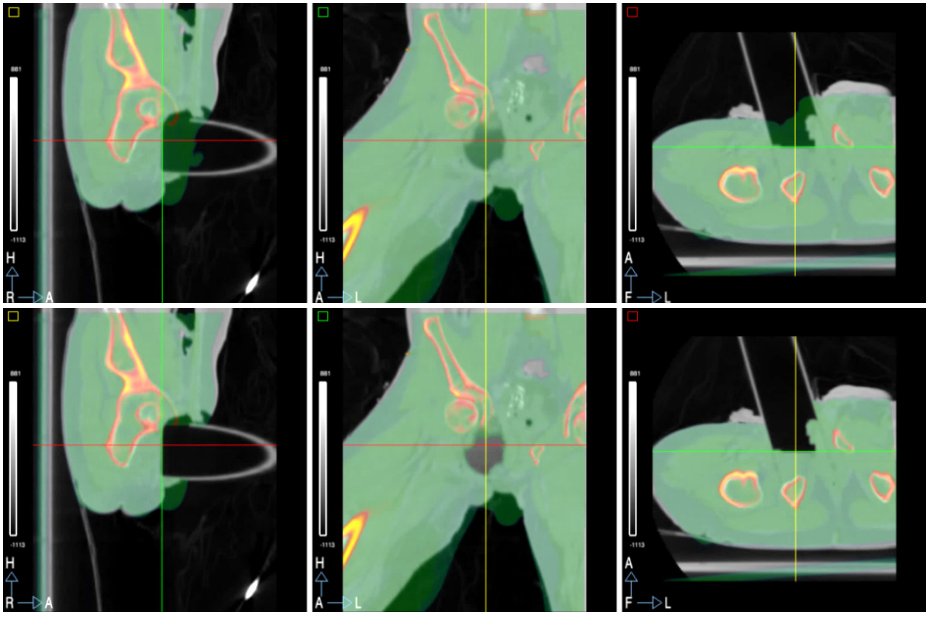

Figure 31. Registered images (Patient 6, chondrosarcoma). Preoperative image (colour) superimposed on its intraoperative image (greyscale). PreCT (top) and preCT$_{air}$ (bottom). From left to right, sagittal view, coronal view and axial view.

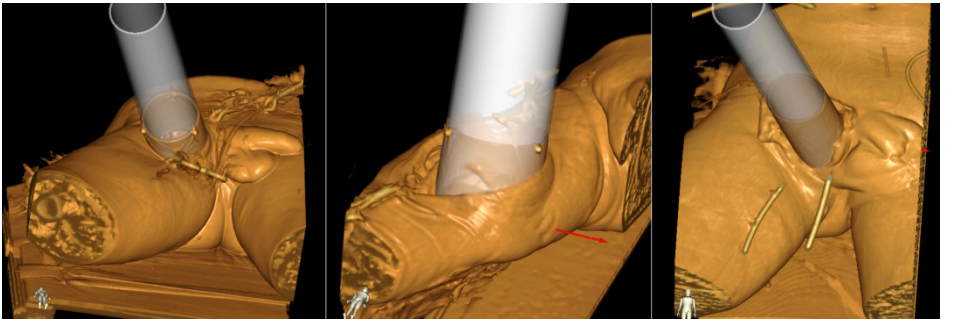

Figure 32. Virtual applicator (greyscale) superimposed on the volume rendering of each intraoperative CT image (colour). From left to right, Patient 1 (Ewing sarcoma), Patient 2 (rhabdomyosarcoma) and Patient 6 (chondrosarcoma).

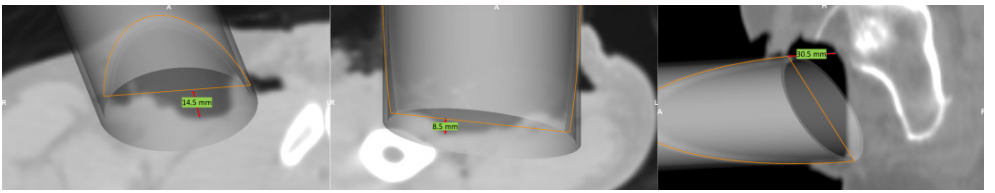

Figure 33. Maximum distance from the applicator bevel to the tumour bed. From left to right, Patient 1 (Ewing sarcoma, 14.5 mm), Patient 2 (rhabdomyosarcoma, 8.5 mm) and Patient 6 (chondrosarcoma, 30.5 mm).

For each IOERT case, the dose distributions from its intraoperative image and preoperative images ($preCT_{water}$, preCT and $preCT_{air}$) can be compared in Figure 34 (Patient 1), Figure 35 (Patient 2) and Figure 36 (Patient 6). The dose distribution from $preCT_{air}$ closely follows that from the intraCT image, more than using $preCT_{water}$ or preCT. The percentage of voxels fulfilling the gamma criteria is detailed in Table 6, Table 7 and Table 8. The values are less restrictive when calculating the dose distribution with pencil beam algorithm than with Monte Carlo algorithm in most cases. Dose distributions using $preCT_{air}$ showed values above 95% in all cases except in three comparisons (gamma pass rates of 94.4%, 94.6% and 93.7% respectively in those specific cases), yielding better results than when using $preCT_{water}$ (just two out of 24 comparisons were above 95%) or preCT (just four out of 24 comparisons were above 95%).

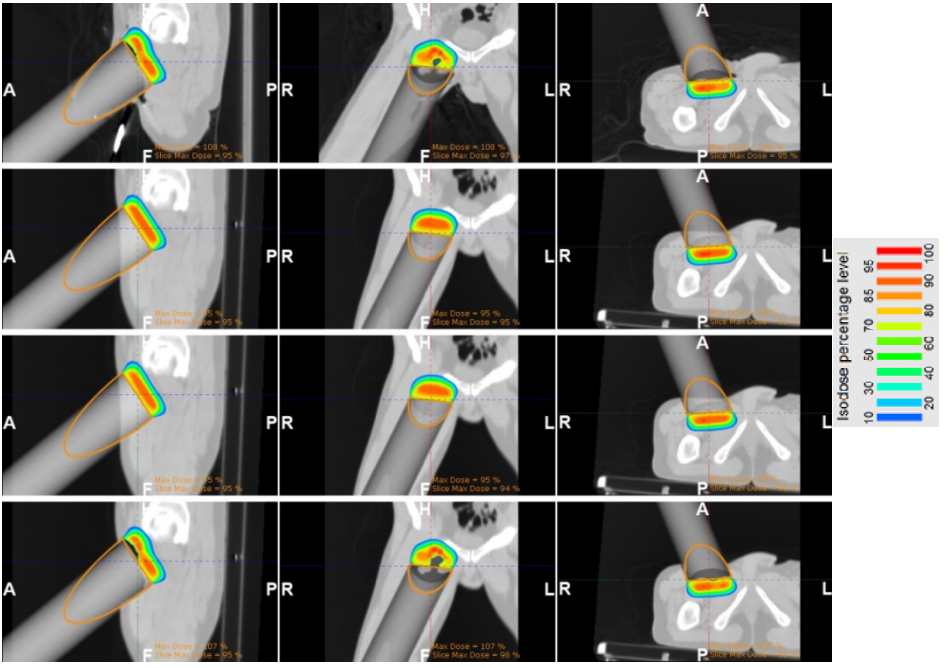

Figure 34. Dose distributions estimated with Monte Carlo algorithm (Patient 1, Ewing sarcoma). From top to bottom, the dose distribution corresponding to intraCT, preCT$_{water}$, preCT and preCT$_{air}$. From left to right, sagittal view, coronal view, axial view and dose scale. R (right) and L (left).

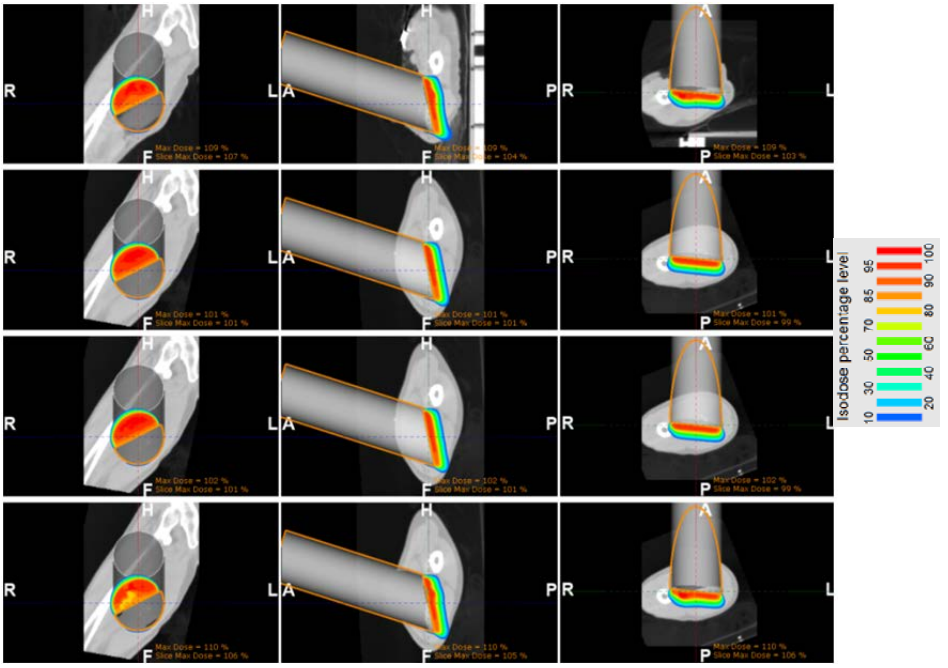

Figure 35. Dose distributions estimated with Monte Carlo algorithm (Patient 2, rhabdomyosarcoma). From top to bottom, the dose distribution corresponding to intraCT, preCT$_{water}$, preCT and preCT$_{air}$. From left to right, sagittal view, coronal view, axial view and dose scale. R (right) and L (left).

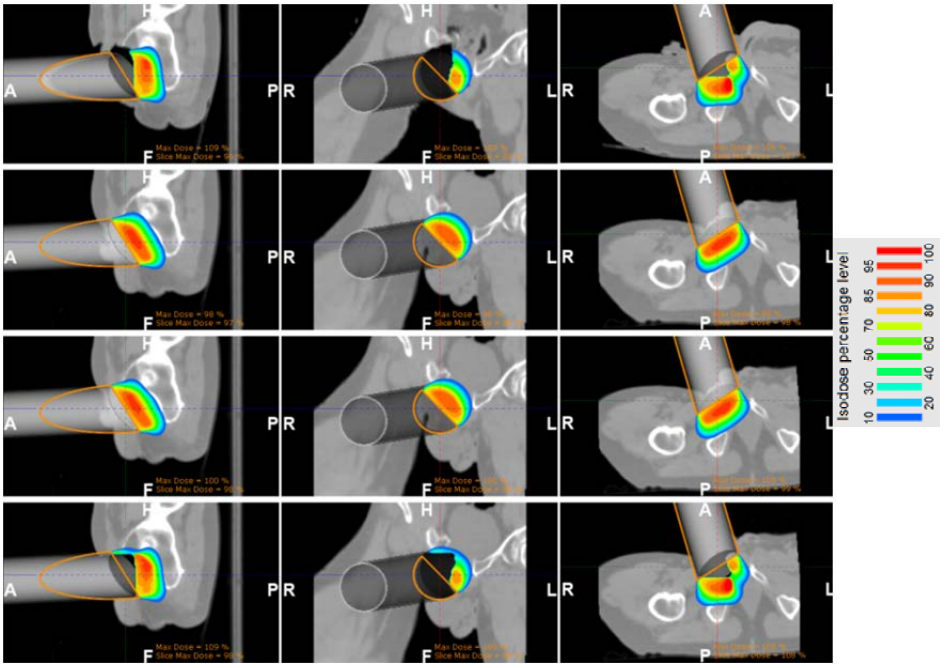

Figure 36. Dose distributions estimated with Monte Carlo algorithm (Patient 6, chondrosarcoma). From top to bottom, the dose distribution corresponding to intraCT, $preCT_{water}$, preCT and $preCT_{air}$. From left to right, sagittal view, coronal view, axial view and dose scale. R (right) and L (left).

Table 6. Percentage of voxels fulfilling the gamma criteria for the case of $preCT_{water}$.[a]

	3%/3 mm				5%/2 mm			
	Dose > 10%		Dose > 70%		Dose > 10%		Dose > 70%	
	PB	MC	PB	MC	PB	MC	PB	MC
Patient 1 (Ewing sarcoma)	87.1	82.3	86.9	80.1	85.2	80.2	85.5	78.9
Patient 2 (Rhabdomyosarcoma)	93.6	90.0	**95.3**	92.0	92.9	89.8	**95.2**	92.9
Patient 6 (Chondrosarcoma)	60.4	52.6	56.1	41.5	56.3	48.3	50.7	38.9

[a] Percentages of voxels fulfilling the gamma criteria higher than 95% are highlighted in bold. PB (pencil beam) and MC (Monte Carlo).

Table 7. Percentage of voxels fulfilling the gamma criteria for the case of preCT.[a]

	3%/3 mm				5%/2 mm			
	Dose > 10%		Dose > 70%		Dose > 10%		Dose > 70%	
	PB	MC	PB	MC	PB	MC	PB	MC
Patient 1 (Ewing sarcoma)	86.9	82.2	86.9	80.3	84.7	80.0	85.4	79.6
Patient 2 (Rhabdomyosarcoma)	**95.9**	92.2	**95.4**	92.1	**95.9**	92.7	**95.4**	93.0
Patient 6 (Chondrosarcoma)	60.7	53.6	56.8	41.7	56.7	49.8	51.5	39.0

[a] Percentages of voxels fulfilling the gamma criteria higher than 95% are highlighted in bold. PB (pencil beam) and MC (Monte Carlo).

Table 8. Percentage of voxels fulfilling the gamma criteria for the case of $preCT_{air}$.[a]

	3%/3 mm				5%/2 mm			
	Dose > 10%		Dose > 70%		Dose > 10%		Dose > 70%	
	PB	MC	PB	MC	PB	MC	PB	MC
Patient 1 (Ewing sarcoma)	**99.9**	**99.5**	**99.9**	**99.8**	**100.0**	**99.6**	**100.0**	**99.9**
Patient 2 (Rhabdomyosarcoma)	**99.9**	**99.4**	**99.8**	**99.1**	**99.9**	**99.7**	**100.0**	**99.7**
Patient 6 (Chondrosarcoma)	**95.4**	94.4	**97.1**	**97.4**	94.6	93.7	**96.2**	**96.2**

[a] Percentages of voxels fulfilling the gamma criteria higher than 95% are highlighted in bold. PB (pencil beam) and MC (Monte Carlo).

5.4 DISCUSSION

This is the first study to compare 3D dose distributions estimated with intraoperative CT images of patients during IOERT (gold standard) to those obtained under the assumption of having just water at the end of the applicator (conventional assumption), tissue heterogeneities (data from their corresponding preoperative CT images) or adding an air gap at the end of the applicator. The comparisons were done in terms of gamma criteria. In our research, we assessed the feasibility of acquiring intraoperative CT images in real IOERT scenarios extending the number of cases and IOERT sites presented in [85]. There were no complications by applying the modified protocol mainly due to the trained multidisciplinary team (namely surgeons, radiation oncologists, anaesthesiologists, nurses and radiotherapy technicians) used to carry out the conventional protocol that involved transferring the anaesthetised patient from the OR to the LINAC room for patient irradiation.

Dose distributions were not calculated in three cases since there were metal artefacts that substantially modified the HU of the intraoperative images due to the shielding discs in the two breast cancer cases and the retractors in the retroperitoneal sarcoma. A two-layered disc such as the one presented in [89] would decrease, but not remove, the metal artefacts in intraoperative images, thanks to the lower attenuation coefficient of copper compared to lead. In the case of retractors, a possible approach would be to remove these devices just before the CT acquisition or to use a non-metallic version of them, although this is not widely available for clinical use. The solution presented in [90], an Army/Navy retractor 3D printed with thermoplastic (polylactic acid, PLA) could be an option. Other alternative to be evaluated, also applicable to the breast cancer cases, would be replacing the incorrect CT values with the corresponding ones from the registered preoperative image or even with the mean CT values of certain regions from the contralateral side.

The dose distributions estimated with the intraoperative images (gold standard) showed differences with respect to those corresponding to water assumption (Table 6). The isodose curves calculated with the intraoperative images were shifted downwards compared to those from $preCT_{water}$ due to the presence of the air gap. The longer the

maximum distance from the applicator bevel to the tumour bed (air gap), the larger the difference in terms of gamma criteria between the gold standard and the dose distribution estimated under the water assumption. Surface irregularities influenced the dose distributions, as displayed in Figure 34 and Figure 36, an expected result in accordance with previous studies [10, 12]. Scatter produced by sharp irregularities in the irradiated surface produce hot or cold spots in the underlying tissues [29]. The hot spot in Figure 36 (axial view) can be explained by this effect. Furthermore, Figure 31 shows a flatter irradiation surface than those of the other IOERT cases. This type of surface is probably related to biological fluid accumulation in that region and also affects the dose distribution (build-up effect, which shifts the dose distribution upwards) [8, 10]. PreCT images did not improve the estimation of the dose distribution compared to water assumption despite those images included the tissue heterogeneities. A better agreement was found when the air gap (and, therefore, the surface irregularities of the irradiated area) was included in the preoperative images. Most of those comparisons yielded a percentage of voxels fulfilling gamma criteria above 95%. A better matching in the chondrosarcoma case might be obtained by enlarging the air gap segmentation to include more volume of the excision cavity. No assessments concerning the tissue inside the applicator can be made as the TPS sets that region to the CT value of air automatically. The registration allowed resembling the patient position during IOERT in each preoperative CT image and placing the applicator in relation to the patient's anatomy as in its corresponding intraoperative image. This step focused on rigidly aligning the bones close to the applicator bevel. The addition of the air gap (and, therefore, the surface irregularities of the irradiated area) provided good enough estimations of the actual IOERT dose distribution. Therefore, the dominant factor in IOERT dose estimation is the air gap and the surface irregularities. This assessment may not be valid, for example, in an IOERT scenario of rectal cancer since the tumour bed is very close to the sacrum or in breast cancer cases since the tumour bed is close to the shielding discs, ribs and the lung. In the evaluated IOERT cases, bones and lungs were not critical tissues as they were at a certain distance from the tumour bed.

In [10], the authors presented in vivo 2D dose distributions for pelvic IOERT. The images obtained from the radiochromic films placed on the irradiation surface showed a partial view of the 3D dose distribution. In our study, 3D dose distributions were obtained using two different methods: pencil beam and Monte Carlo. The gamma pass rates were higher when using the pencil beam estimation than with the Monte Carlo method for most cases. Pencil beam algorithm is subject to limitations with small irradiated volumes owing to the semi-infinite layer approximation and does not model backscatter radiation (for example, that produced by shielding discs) [49] (section 3.7). On the other hand, Monte Carlo algorithm better models electron-tissue interactions and consequently identifies subtle differences between the intraoperative CT images and the rest of images used in this study.

Intraoperative CT images allow inspecting the protection assembly, which is the highest risk in IOERT [91] due to the lack of direct visual disc inspection, as it happened in the case of Patient 3 (Figure 26). However, transferring the patient to the CT simulator room to acquire intraoperative images may not be approved when a dedicated mobile LINAC is available in the OR. Other approaches to check the alignment between the shielding disc and the applicator/tumour bed may be using 2D portal images (MV) [4], ultrasound (US) images [6], X-ray images (acquired with a C-arm) [5], radiochromic films (for a posteriori analysis) [44] or using an applicator system that assures the protection assembly [92].

Our results have showed that the conventional assumption of having a flat irradiation surface of water at the end of the applicator can lead to erroneous assessments in IOERT. In breast cancer cases, this supposition can be valid [12] but not in the case of, for example, soft-tissue sarcomas in distal limbs (air gaps up to 5 cm, [93]) or in rectal cancer (irregular and/or concave surface, [10]). Intraoperative CT images would allow estimating the dose distribution of the actual IOERT scenario just before the radiotherapy treatment to adjust the IOERT settings or afterwards, to assess the outcome of the procedure with the registered IOERT parameters. These images can be acquired with a portable CT inside the OR or even with a LINAC that includes an on-board kV CBCT [94]. The cost of these solutions may limit their use in most institutions. Other intermediate approaches to be further evaluated involve acquiring

2D projections with a C-arm of the whole setting (patient and applicator) [95] or surfaces with a conoscopic holography device [96] to update preoperative CT images with this intraoperative data. In this last solution it would be necessary to know the applicator pose in relation to the patient's anatomy by using a tracking system [71]. All these technologies will allow updating the preoperative planning with actual dose estimation during the real IOERT procedure, facilitating decision making to the radiation oncologist and improving the available information for patient's follow-up.

5.5 CONCLUSIONS

In this specific study, intraoperative CT images of real IOERT scenarios were acquired after transferring the patient from the OR to the CT simulator room before tumour bed irradiation. There were no complications by applying the modified IOERT protocol. The intraoperative images were used to estimate the actual 3D dose distribution in three out of the six evaluated IOERT cases. Those cases were discarded due to the presence of metal artefacts that substantially modified CT values. Gold standard estimations were compared to those calculated with their corresponding preoperative images. Results showed that preoperative CT images can be used to estimate the IOERT dose distribution under two conditions: knowing the applicator pose in relation to the patient's anatomy (specifically to the bones) and incorporating information regarding the air gap between the end of the applicator and the tumour bed (and, therefore, the surface irregularities of the irradiated area). These IOERT dose distributions could be useful for patient follow-up and also for dose accumulation when EBRT is applied after an IOERT boost.

6 ASSESSMENT OF INTRAOPERATIVE 3D IMAGING ALTERNATIVES FOR IOERT DOSE ESTIMATION

This chapter presents the specific study that evaluated several kV CT technologies other than CT simulators to acquire intraoperative images for estimating IOERT dose distribution with the actual condition. This research was related to the third specific objective of this thesis and was published in *Zeitschrift für Medizinische Physik* journal [94].

6.1 INTRODUCTION

Regarding intraoperative imaging in IOERT, relevant recent studies include that of [4], who proposed 2D portal imaging to ensure alignment between the applicator and the shielding disc in breast cancer IOERT. In [97], the authors conducted a preliminary phantom study to evaluate the feasibility of using a C-arm with 3D imaging capability (ARCADIS® Orbic 3D, Siemens, Germany) to acquire images during IOERT, concluding that C-arm image quality was a major limitation. In [85], our group presented the first two clinical cases (Ewing sarcoma and undifferentiated sarcoma) in which intraoperative images were acquired using a CT simulator during IOERT. The patient was transferred from the operating room (OR) to the CT simulator room for acquiring an intraoperative CT image before the radiotherapy delivery in the treatment room. The 3D dose distribution of the actual treatment administered to the patient was calculated from the intraoperative CT image of the whole setting (patient and applicator) after superimposing the virtual applicator of the treatment planning system (TPS) on its actual position displayed in the CT image. Moreover, the dose was also estimated from their preoperative image after removing the tumour and its surrounding area as expected during the surgery and then aligning with the intraoperative CT image using deformable registration. Despite that preprocessing, there were still differences

between the dose distributions estimated with those preoperative images and those obtained from the intraoperative images (average difference of 5%). In [12] the authors pointed out that surface irregularities, simulated with a phantom, can significantly influence the IOERT dose distribution. Nowadays, IOERT is not entirely characterised since no intraoperative images of the actual scenario are routinely acquired during the treatment. This information would be useful not only for intraoperative planning but also for registering and evaluating the treatment administered to the patient. Following the approach of acquiring intraoperative images with CT simulators [85] has the limitation of the additional risks involved in transferring the patient to the CT simulator room. This setup may not be justified if a dedicated mobile electron accelerator is available in the OR.

In external beam radiation therapy (EBRT), imaging is currently used for identifying differences in patient positioning or target position prior to treatment delivery (image-guided setup correction). Many modern LINACs include integrated cone-beam CTs (CBCTs) that enable acquisition of 3D images with the patient in the treatment position that are then registered and compared with the planning CT. Moreover, these images can also be used to adapt the treatment plan depending on anatomical changes (weight loss, and tumour regression and displacement) during the radiotherapy course [98]. Several articles have focused on the feasibility of using CBCT images for dose calculation in EBRT and show that CBCT images cannot be used directly for dose estimation because their quality is lower than that of CT simulator images. For instance, dose calculations for treatment fields that have a larger size and different geometry than the phantom used in the calibration procedure for converting CT values into density resulted in dose errors larger than 5% (photons) [99]. Several approaches have been proposed in order to overcome this problem, including mapping CT values from planning CT to CBCT after rigid alignment [100], treatment field-specific look-up tables that convert CT values to density [99], a density override method based on segmenting water, air and bone [101], and measuring the scatter distributions from the first CBCT scan acquired for patient setup and applying scatter correction on subsequent CBCT scans acquired throughout the radiotherapy course [102].

To our knowledge, no studies have evaluated the use of kV CT technologies other than CT simulators, as is the case of CBCT devices or even portable multislice CT (MSCT) scanners, to acquire intraoperative images for estimating IOERT dose distribution with the actual conditions. In this study, we evaluate the feasibility and potential of using kV CT imaging systems other than CT simulators that can be integrated in the IOERT workflow to calculate radiation doses more accurately.

6.2 METHODS

In this section, we describe the CT imaging systems evaluated in this study and the methodology followed to assess their potential. The devices were selected based on their suitability for imaging during IOERT. The three CT scanners chosen comprised two portable systems and one device integrated in a conventional LINAC. Two commercial phantoms were acquired using the systems under evaluation to simulate two representative IOERT treatments. The same phantoms were also imaged in a conventional CT simulator and the dose distributions calculated from these studies formed the gold standards for our comparisons.

CT imaging systems evaluated

The three scanners with a kV CT imaging facility evaluated in this study were O-arm® Surgical Imaging (Medtronic, USA), TrueBeam™ STx (Varian Medical Systems, USA) and BodyTom® Portable CT Scanner (NeuroLogica Corporation, USA) (Figure 37).

Other commercial C-arms that provide 3D imaging capability include ARCADIS® Orbic 3D (Siemens, Germany), BV Pulsera (Philips, The Netherlands) and Ziehm Vision FD Vario 3D (Ziehm Imaging Inc., USA). However, none of these devices was selected for this study owing to their reduced field of view (FOV). For instance, the reconstructed FOV size of Orbic 3D is 12 x 12 x 12 cm.

The systems studied are described briefly below:

- O-arm is a portable kV cone-beam scanner with a larger FOV than previously mentioned C-arms. Its sliding gantry enables lateral access and is closed for

image acquisition. It incorporates a 30 cm x 40 cm flat panel (Varian model PaxScan 4030 CB, amorphous silicon digital X-ray detector with a 1536 x 2048 pixel matrix and pixel pitch of 0.194 mm). The reconstructed FOV size is 20 cm (diameter) x 15 cm (height), with a matrix size of 512 x 512 x 192 and voxel size of 0.415 x 0.415 x 0.832 mm.

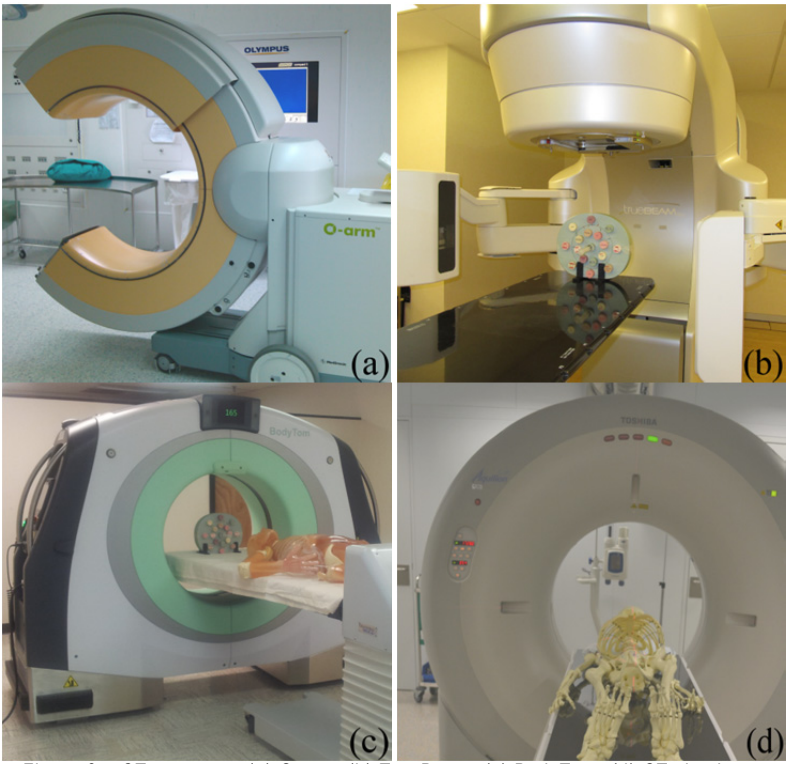

Figure 37. CT scanners: (a) O-arm, (b) TrueBeam, (c) BodyTom, (d) CT simulator.

O-arm has a gantry opening of 96.5 cm and its physical dimensions are 249 x 81.3 x 202.2 cm (length x width x height). It is mainly used in spinal and orthopaedic surgeries.

- TrueBeam combines the features of a LINAC and a kV CBCT. The on-board kV imager has a flat panel with a pixel matrix of 1536 x 2048 and an anti-scatter grid on top of the scintillator layer. The 3D image FOV is 46 x 46 x 16 cm for half-fan mode and 25 x 25 x 17 cm for full-fan mode, with a slice thickness ranging from 1 mm to 10 mm. The source-detector

distance is 150 cm. Its imaging tools are used to verify the patient's position and tumour motion during treatment.

- BodyTom is a portable MSCT scanner (32 slices) with an FOV of 60 cm (slice thickness from 1.25 mm to 10 mm, image matrix 512 x 512). This CT device works in helical or axial mode and moves along the bed to perform acquisitions. BodyTom has a gantry opening of 85 cm and physical dimensions of 256.5 x 104 x 205.7 cm (length x width x height). The device is optimised for use in spinal surgery, tumour removal and interventional radiology.

All three devices fulfil the requirements for radiotherapy planning using scanners with wide apertures (at least 70 cm [103]). Of the three, BodyTom has the smallest gantry opening. Wide apertures are essential in IOERT, since abdominal surgical retractors or patient position (for example, lithotomy position) can prevent the patient from entering the gantry opening.

These devices could be a good solution for intraoperative imaging in IOERT procedures with different workflows. O-arm and BodyTom could be moved into the OR in order to acquire the actual scenario before irradiating the patient with, for example, a mobile electron accelerator also located inside the OR. TrueBeam, on the other hand, enables intraoperative images to be obtained before radiation is delivered with its conventional LINAC. Using the TrueBeam approach, it would be necessary to transfer the patient from the OR to the LINAC room or alternatively the surgery could be performed in the LINAC facility, thus avoiding transportation.

CT simulator

The reference dose distributions were calculated from images acquired on an Aquilion™ Large Bore CT simulator (Toshiba, Japan). This multi-slice helical CT (16 slices) has a 70-cm FOV and a 90-cm gantry opening. This device is located in the Department of Radiation Oncology at Hospital General Universitario Marañón (Madrid, Spain) and its images are used for planning EBRT treatments. This CT simulator fulfilled the image quality tests of the Spanish Society of Medical Physics (http://www.sefm.es; results: noise 0.4%, field uniformity 3.8 HU, CT number for air

–980 HU and for water 3.8 HU [CT number accuracy], contrast resolution [low contrast resolution] 3.5% @ 2.5 mm and absence of artefacts) excepting the spatial resolution (high contrast resolution) test whose result (1 mm) was slightly higher than the manufacturer specification (0.6 mm). The spatial integrity [104] was 0.3 mm x 0.1 mm in the transaxial plane and 0.3 mm along the axial axis.

Phantoms

Two phantoms were used in this study: the model 062 electron density phantom and the model 057 triple modality 3D abdominal phantom, both from CIRS Inc. (USA) (Figure 38).

The model 062 phantom enables conversion from CT number to physical density to calibrate each scanner, since this relationship varies between scanners [105]. Conversion factors were incorporated into the IOERT TPS to take account of tissue heterogeneity in dose calculation. The phantom consists of two nested discs (a head insert and a body disc) made from Plastic Water® (dimensions 33 x 27 x 5 cm) and several plugs (dimensions: 30 mm diameter x 50 mm length) of eight different tissue equivalent epoxy resins (lung inhale, lung exhale, adipose, breast 50% gland/50% adipose, muscle, liver, trabecular bone 200 mg/cc hydroxyapatite [HA] and dense bone 800 mg/cc HA). A vial plug filled with sterilised water was placed at the centre of the phantom.

The model 057 phantom makes it possible to simulate a small adult abdomen approximately from thoracic vertebrae T9/T10 to lumbar vertebrae L2/L3 and includes the liver, part of both kidneys, part of the lung surrounding the liver, portal vein, vena cava, abdominal aorta, spine and six ribs. This phantom was used to simulate two IOERT cases in order to compare dose distributions calculated from images acquired with the devices evaluated and the CT simulator (gold standard). The phantom housing is made from acrylonitrile butadiene styrene (ABS) and the rest of the phantom from proprietary gels. Its dimensions are 28 x 20 x 12.5 cm.

CT acquisitions

Electron density and abdominal phantoms were scanned with each system. All CT acquisition parameters except matrix size were set to the same values for both phantoms in each scanner. Since the acquisition protocols offered a limited number of parameter combinations for each scanner, those selected were as similar as possible between scanners taking account of this restriction (Table 9). Tube voltage was selected according to typical CT protocols for radiotherapy planning.

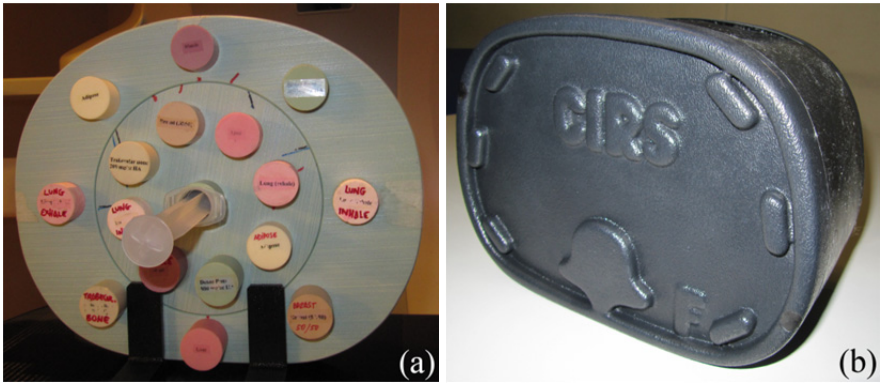

Figure 38. Phantoms: (a) model 062 electron density phantom, (b) model 057 triple modality 3D abdominal phantom.

Table 9. CT acquisition parameters.

	Voltage (kVp)	Exposure (mAs)	Matrix size	Voxel size (mm)
CT simulator	120	300	512 x 512 x 141[a] 512 x 512 x 251[b]	0.6 x 0.6 x 1.0
O-arm	120	298	512 x 512 x 192	0.4 x 0.4 x 0.8
TrueBeam (half-fan mode)	125	262	512 x 512 x 81	0.9 x 0.9 x 2.0
BodyTom (helical, soft tissue filter)	120	295	512 x 512 x 136[a] 512 x 512 x 128[b]	1.2 x 1.2 x 1.3

[a] Electron density phantom.
[b] Abdominal phantom.

Conversion of the CT number to physical density

Electron density phantom images were used to calibrate the conversion from CT number to physical density in each system. Cylindrical regions of interest (ROIs) of 20 mm diameter x 20 mm length were contoured centred on each plug, on the electron density head insert, on the electron density body disc, on the vial plug filled with sterilised water and outside the phantom (air). The region of interest (ROI) selected in the dense bone (800 mg/cc HA) equivalent electron density plug was smaller (6 mm diameter x 20 mm length) because the insert contains a 10-mm core of bone equivalent surrounded by water-equivalent material.

An in-house implementation of the stoichiometric calibration [50] was applied to the data from the electron density phantom to obtain the CT numbers specific for each scanner of seven PENELOPE materials (dry air, lung, adipose tissue, striated muscle, muscle-equivalent liquid with sucrose, B100 and cortical bone) with known physical density and chemical composition (section 3.8). PENELOPE software is used to perform Monte Carlo simulation of coupled electron-photon transport and of electron and positron interactions [106]. The chemical composition of these PENELOPE materials closely follows the International Committee for Radiological Units (ICRU) or the International Commission on Radiological Protection (ICRP) standard chemical composition for biological tissues. B100 is a tissue substitute that has a chemical composition close to that of soft bone. The least squares fit of the stoichiometric calibration assumes that CT numbers are in HU so that X-ray attenuation of distilled water and attenuation of air at standard pressure and temperature are defined as 0 HU and –1000 HU respectively. The physical density and chemical composition of the materials of the electron density phantom were provided by CIRS Inc. The CT numbers of those seven PENELOPE materials and their physical density (calibration curve) were then entered into the IOERT TPS.

In the case of the O-arm scanner, two modifications to the procedure were necessary to convert the CT number to physical density. First, electron density phantom CT image values were linearly transformed, since the CT numbers for air and distilled water were different from –1000 HU and 0 HU respectively. Second, as the FOV acquired by the

O-arm covered only the electron density head insert, eleven ROIs were drawn on that image instead of the twenty ROIs segmented on the images from the other scanners. These adjustments were necessary to perform the stoichiometric calibration.

Several profiles were drawn on the electron density phantom images after rigid alignment of the studies from all the scanners (manual registration using the CT simulator image as a reference) in order to evaluate the variations in CT number within each plug between the CT simulator and each of the CT devices under evaluation.

Dose distribution evaluation

Two IOERT cases were simulated on the images from the abdominal phantom using the TPS radiance (GMV, Spain) [3]: a pancreatic tumour and a soft-tissue sarcoma in paraspinal muscle. Abdominal images were resampled to 1.5-mm isotropic voxel size and then aligned (automatic rigid registration with normalised mutual information as cost function) using the CT simulator image as a reference. This procedure enabled us to place the IOERT applicator in the same position for all of the scanners. Dose distributions were calculated using the Monte Carlo algorithm (error tolerance 1%) [50] and doses were not scaled to a normalised value (section 5.2). The pencil beam algorithm was not used in this study as it is subject to limitations with small irradiated volumes owing to the semi-infinite layer approximation and does not model backscatter radiation (for example, that produced by shielding discs) [49].

In the case of the pancreatic tumour, the pancreas and liver were segmented and the CT numbers of the voxels inside those masks were set to air in order to simulate tumour resection and liver displacement respectively. Surgical access was also simulated in the TPS. Tumour bed (clinical target volume [CTV]) and organs at risk (OARs: aorta, vena cava, left kidney and spinal cord) were also contoured. The IOERT parameters were applicator diameter 50 mm, bevel angle 0º, energy 6 MeV and a prescribed dose of 15 Gy at a 90% isodose (Figure 39(a)).

In the case of the paraspinal muscle sarcoma, the procedure followed was similar, namely, surgical access, tumour resection and segmentation of the CTV and OARs (right kidney and spinal cord). To protect the right kidney, two shielding discs were

placed virtually between the CTV and the right kidney. A brass disc (thickness 3 mm, diameter 60 mm, physical density 8.6 g/cc) was placed close to the right kidney and a Teflon disc (thickness 3 mm, diameter 60 mm, physical density 2.2 g/cc) was positioned above the brass disc and towards the CTV to reduce backscattering radiation from the brass disc. The IOERT parameters were applicator diameter 50 mm, bevel angle 15º, energy 6 MeV and a prescribed dose of 12.5 Gy at a 90% isodose (Figure 39(b)).

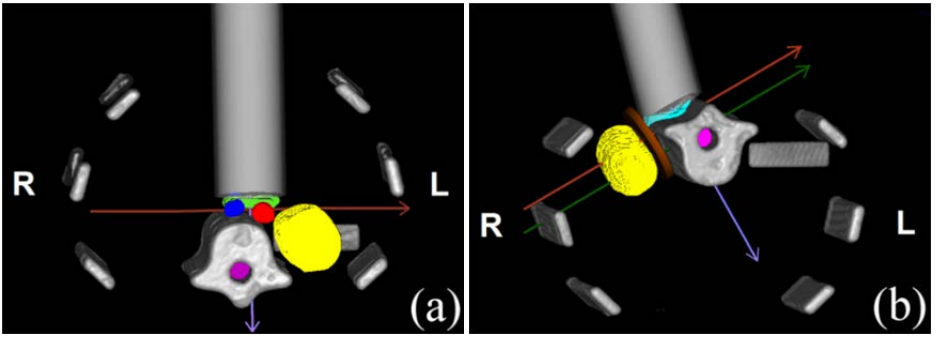

Figure 39. Simulated IOERT cases: (a) pancreatic tumour (CTV in green, aorta in red, vena cava in blue, left kidney in yellow and spinal cord in purple), (b) paraspinal muscle sarcoma (CTV in blue, right kidney in yellow, spinal cord in purple and shielding discs in brown). Clinical axis in purple, transverse axis at depth of 10 mm in red and transverse axis at depth of 25 mm in green. R (right) and L (left).

Dose distributions calculated from images obtained with the devices under evaluation were compared with the gold standard (CT simulator) in terms of the gamma index (section 3.5). An acceptance criteria of 3%/3 mm and also of 5%/2 mm for dose values greater than either 10% or 70% (to focus on high dose regions) were used in the comparisons as in section *IOERT dose distributions* (section 5.2). Cumulative dose-volume histograms (DVHs), percentage of depth dose (PDD) profiles and transverse dose profiles (TDPs) at several depths were also obtained for both IOERT cases and all scanners (Figure 39).

In the case of the O-arm scanner, the CT image of the abdominal phantom was first transformed by applying the same adjustment used with the electron density phantom in order to fix CT numbers.

6.3 RESULTS

Figure 40 illustrates the nonlinear CT number to physical density conversions for all devices. The curves are similar until the inflection point at around 100 HU. For higher CT numbers, the physical density differs between scanners.

Figure 41 shows three different profiles for each CT scanner, two on a transaxial view and one along the axial axis. O-arm intensity values presented an offset (corrected for stoichiometric calibration and dose estimation as explained in section 6.2), and the intensity difference between materials was smaller than with the CT simulator. TrueBeam profiles were closer to the CT simulator profiles than those from the O-arm, although there was a smooth change in homogeneous areas such as Plastic Water (Figure 41(a)) and incorrect CT values in trabecular bone (Figure 41(b)). On the other hand, BodyTom CT numbers were quite similar to those of the CT simulator except for a disagreement in the dense bone values (Figure 41(b)).

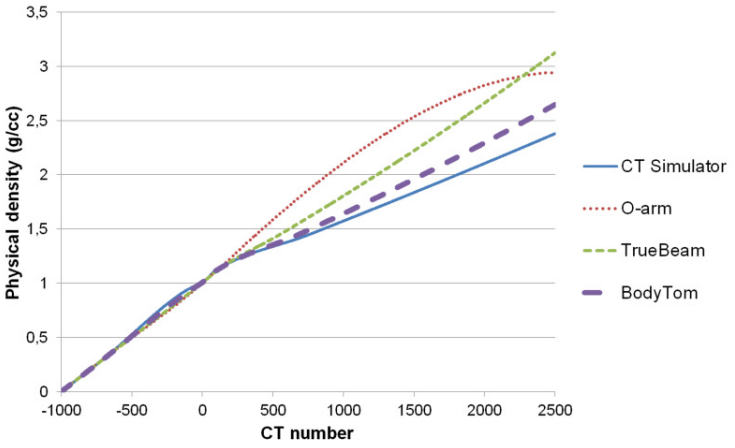

Figure 40. Calibration curves for the transformation of CT number to physical density for each CT scanner.

Two IOERT cases were simulated with the TPS using the images from the abdominal phantom. The registration results for all these CT images were checked by visual inspection. The FOV acquired by the O-arm did not cover the whole abdominal phantom, but the treatment volume and surrounding tissues were sufficiently covered to obtain comparable results. Figure 42 and Figure 43 show the dose distributions and

the cumulative DVHs for both scenarios respectively. In the case of the pancreatic tumour, the results for the different CT devices are quite close to the gold standard except for the O-arm, whose cumulative DVHs differ slightly from the reference. The DVHs of the left kidney and the spinal cord were not displayed since the 10% of the volume of those organs would absorb at least a dose of 33 cGy in all devices. In the case of the paraspinal muscle sarcoma, the disagreement with the gold standard is slightly higher than in the case of the pancreatic tumour for all scanners and is more noticeable in the spinal cord cumulative DVH calculated using the O-arm image. The DVH of the right kidney was not shown since the 10% of the volume of this organ would get at least a dose of 28 cGy in all devices. Figure 44 shows the PDDs corresponding to both IOERT scenarios with the characteristic dose gradient of electron beams. The behaviour of the PDDs is similar to that of the DVHs. Dose differences with respect to the CT simulator increased with depth. On the other hand, the TDPs at 10 mm are similar to the CT simulator TDPs, except for the O-arm TDP from the case of the paraspinal muscle sarcoma (Figure 45). Further analysis of this second IOERT case shows that the TDP at 25 mm went through the spinal cord, the shielding discs and the right kidney (Figure 39(b), Figure 45(c)). The percentage of dose is zero for the O-arm and higher for the TrueBeam and the BodyTom, but lower than the gold standard in all cases. Table 10 and Table 11 include the percentage of voxels fulfilling selected gamma criteria (3%/3 mm and 5%/2 mm) for the pancreas and the paraspinal muscle respectively. Regarding the O-arm, the percentage is below 75% in both IOERT cases. TrueBeam showed values above 95% in all cases except in two comparisons, yielding gamma pass rates of 91.7% and 94.4% in those specific scenarios (in the pancreatic tumour, when voxels with a dose higher than 10% and gamma criteria of 3%/3 mm were selected, and in the paraspinal muscle, when voxels with a dose higher than 10% and gamma criteria of 5%/2 mm were chosen respectively). BodyTom yielded better results with more than 98% of voxels fulfilling the gamma criteria in all comparisons.

Finally, Table 12 shows the CT numbers of the seven PENELOPE materials obtained in the stoichiometric calibration and the CT numbers of several ROIs (circle of radius 3.5 mm) drawn in the abdominal phantom for each scanner. In the case of the O-arm,

the CT numbers of the abdominal phantom do not follow the correspondence with those of PENELOPE materials. For instance, the CT numbers of rib and vertebra ROIs should be below those of B100 for the O-arm device, as is the case for the CT simulator, TrueBeam and BodyTom.

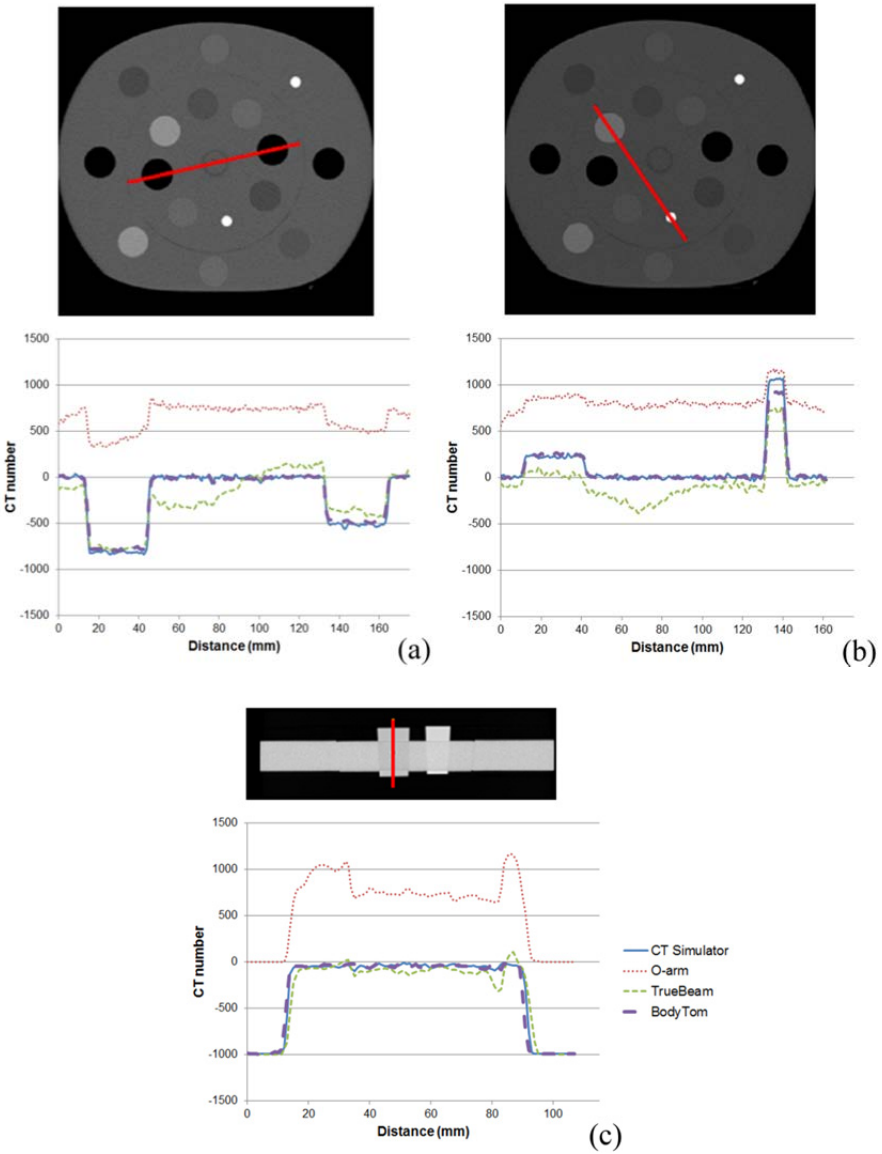

Figure 41. Electron density phantom profiles for each CT scanner: (a) Lung inhale - Plastic Water - Lung exhale, (b) Trabecular bone 200 mg/cc HA - Plastic Water - Dense bone 800 mg/cc HA, (c) Air - Breast 50% gland / 50% adipose - Air. Values shown for O-arm profiles are not corrected.

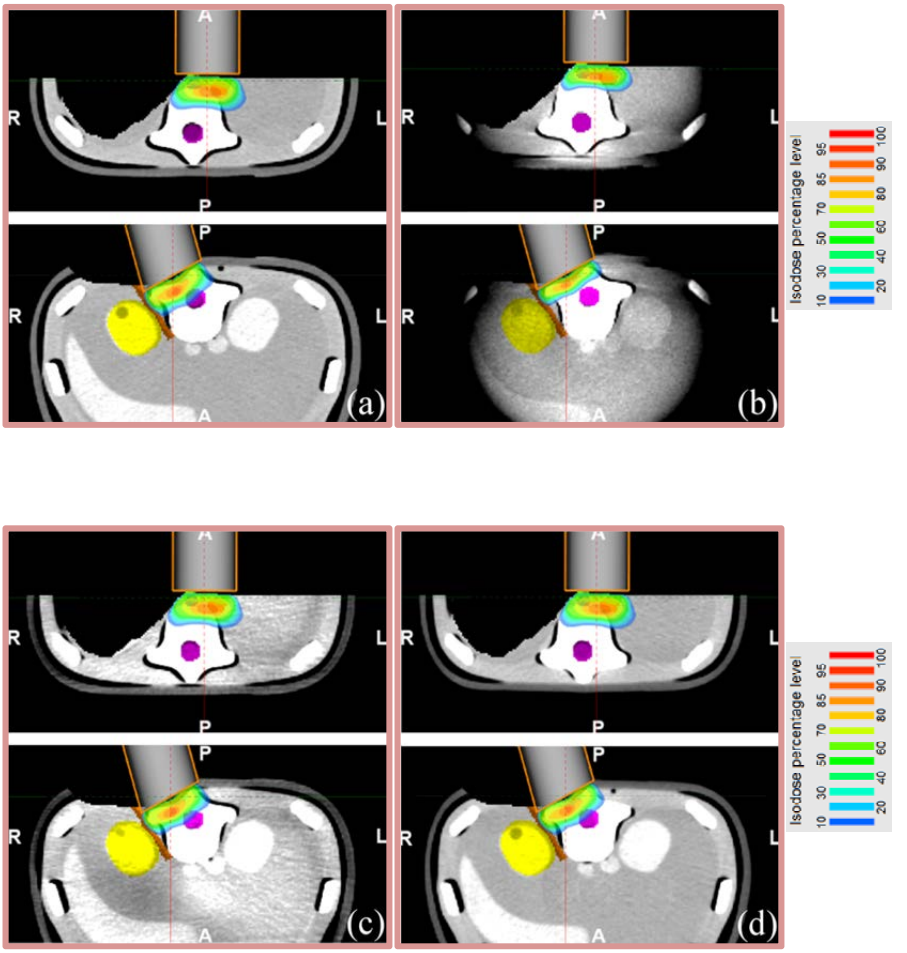

Figure 42. Axial view of dose distributions. (a) CT simulator, (b) O-arm, (c) TrueBeam, (d) BodyTom. Pancreatic tumour (top) and paraspinal muscle sarcoma (bottom). Right kidney (yellow), spinal cord (purple), and shielding discs (brown). R (right) and L (left).

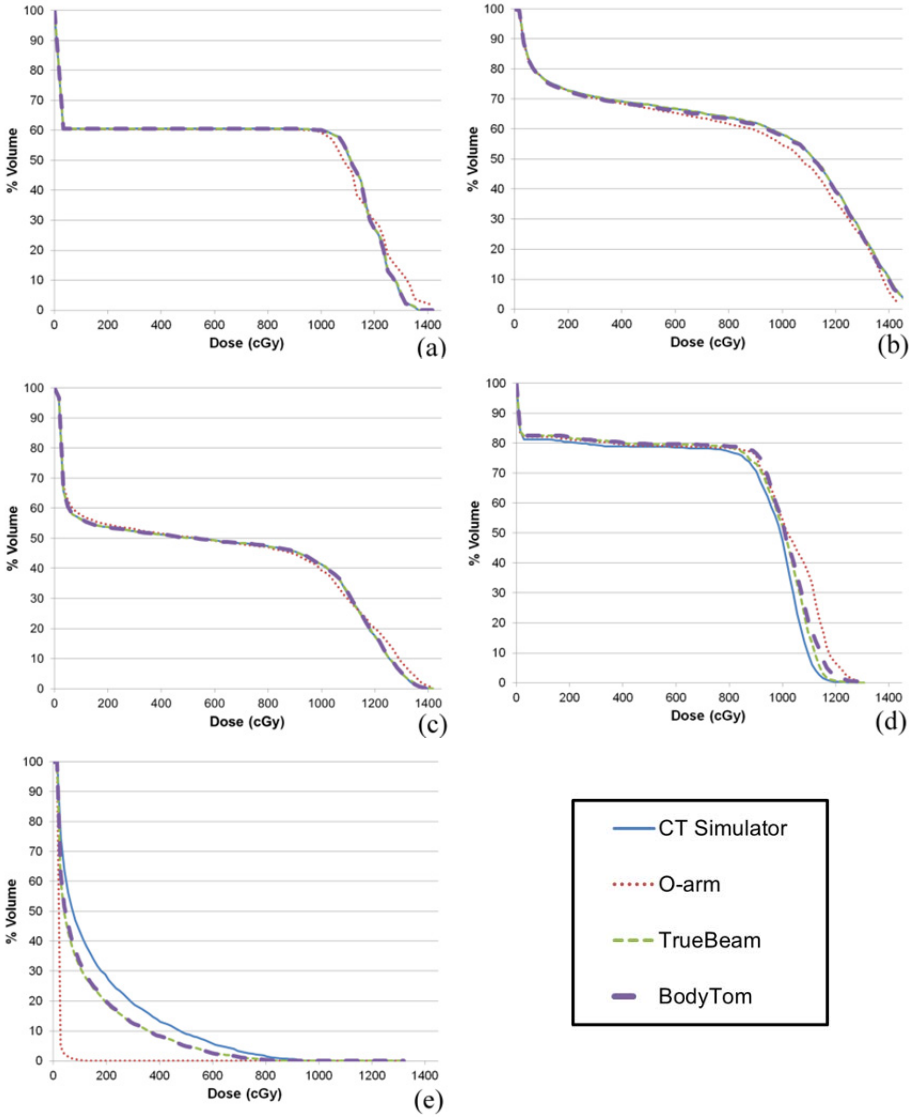

Figure 43. Cumulative DVHs. In the case of pancreatic tumour, (a) tumour bed (CTV), (b) aorta and (c) vena cava. In the case of the paraspinal muscle, (d) CTV and (e) spinal cord.

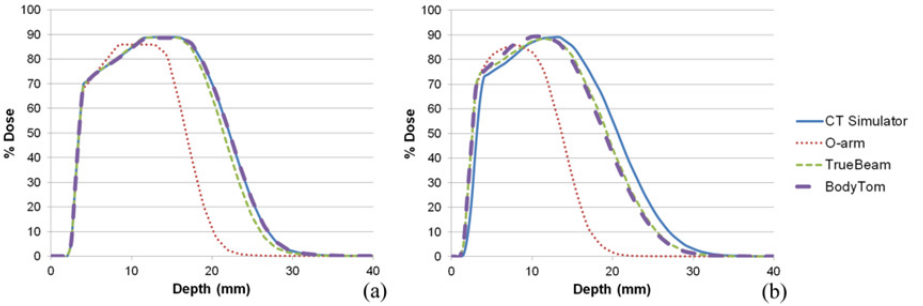

Figure 44. PDDs in the case of the (a) pancreatic tumour and (b) paraspinal muscle sarcoma.

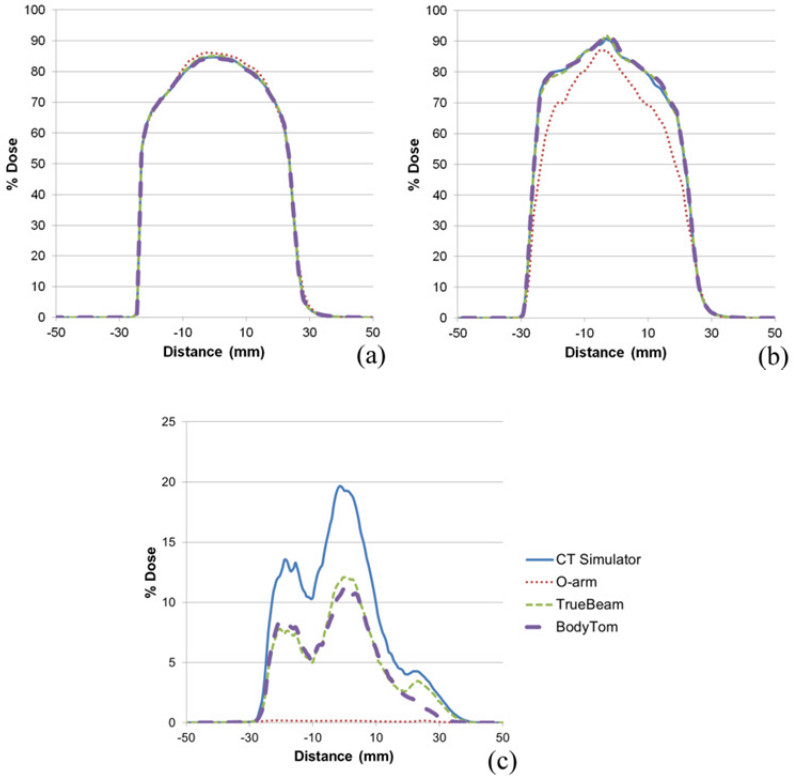

Figure 45. TDPs at a depth of 10 mm in the case of the (a) pancreatic tumour and (b) paraspinal muscle sarcoma. TDPs at a depth of 25 mm in the case of the (c) paraspinal muscle sarcoma (shielding discs were at a position –30 mm).

Table 10. Percentage of voxels fulfilling the gamma criteria for the case of pancreatic tumour.[a]

	3%/3 mm		5%/2 mm	
	Dose > 10%	Dose > 70%	Dose > 10%	Dose > 70%
O-arm	52.3	70.8	45.9	68.7
TrueBeam	91.7	**97.9**	**95.9**	**99.7**
BodyTom	**100.0**	**100.0**	**100.0**	**100.0**

[a] Percentages of voxels fulfilling the gamma criteria higher than 95% are highlighted in bold.

Table 11. Percentage of voxels fulfilling the gamma criteria for the case of the paraspinal muscle sarcoma.[a]

	3%/3 mm		5%/2 mm	
	Dose > 10%	Dose > 70%	Dose > 10%	Dose > 70%
O-arm	43.3	55.6	37.4	47.8
TrueBeam	**98.1**	**97.7**	94.4	**97.0**
BodyTom	**98.7**	**99.9**	**99.1**	**100.0**

[a] Percentages of voxels fulfilling the gamma criteria higher than 95% are highlighted in bold.

Table 12. CT numbers of the seven PENELOPE materials obtained in the stoichiometric calibration and CT numbers of several ROIs drawn in the abdominal phantom for each scanner.

		CT Simulator	O-arm (corrected values)	TrueBeam	BodyTom
PENELOPE materials	Dry air	–998.9	–998.9	–998.9	–998.9
	Lung	–701.7	–702.3	–701.6	–701.4
	Adipose tissue	–131.4	–72.3	–81.7	–102.2
	Striated muscle	32.4	32.8	34.6	34.5
	Muscle-equivalent liquid with sucrose	85.4	98.8	96.2	91.5
	B100	759.7	380.9	550.4	683.9
	Cortical bone	1526.2	741.5	1055.2	1331.0
Abdominal phantom	Soft tissue	43.6	376.0	66.5	43.7
	Liver	98.3	393.7	106.2	101.0
	Rib	495.6	499.5	477.0	471.9
	Vertebra	516.7	820.7	473.9	466.1

6.4 DISCUSSION

This is the first study to assess three kV CT imaging systems other than CT simulators with the ability to acquire intraoperative images in the IOERT framework. Since the evaluation focused on dose distribution rather than imaging performance for CT simulators, parameters such as image noise, contrast resolution, spatial resolution and spatial integrity [104] were not assessed.

TrueBeam and BodyTom showed very good agreement (BodyTom slightly better than TrueBeam) with the reference, with only small differences in terms of DVH, PDD, TDP at a specific depth and specific gamma criteria. This was not the case of the O-arm, which had a lower percentage of voxels fulfilling the gamma criteria. The main applications of O-arm device are spinal and orthopaedic surgeries, not the estimation of dose distributions. As for PDDs, differences were more noticeable at greater depths. This finding is consistent with previously published data for an energy level of 6 MeV [107]. Higher disagreement was observed for the case of the paraspinal muscle sarcoma (Figure 45(c)): no dose is calculated for the O-arm and a lower value than the reference dose is calculated for the TrueBeam and BodyTom. As the spinal cord is centred at 25 mm, the underdosage in the PDDs (Figure 44) and in the TDPs (Figure 45(c)) led to underestimation of the spinal cord DVHs (Figure 43). Nevertheless, that depth was out of the therapeutic range and close to the end of the practical range of all PDDs. The low dose in the spinal cord (paraspinal muscle sarcoma) with the O-arm was due to the wrong correspondence between the CT numbers of the abdominal phantom and those of the PENELOPE materials. In the case of the O-arm, CT numbers of the vertebra were higher than the values of the cortical bone. In the rest of devices, CT numbers of the vertebra were much lower than the values of the cortical bone. The number of electrons that would interact with the spinal cord would be lower in the case of the O-arm than in the rest of devices since physical densities assigned to the vertebra would be higher than the values for the cortical bone, thus reducing the dose in the spinal cord. The gamma criteria were only affected in the O-arm case.

Image artefacts are a major source of error when estimating dose distribution. They imply inconsistency between CT numbers in the reconstructed image and the true attenuation coefficients of the tissues. Two of the devices evaluated in this study are CBCT systems. Although CBCT has a lower imaging dose than MSCT, it has disadvantages such as increased scattered radiation (increased noise, decreased contrast resolution, shadows, streaks and cupping artefacts), truncation artefacts (a rim of high-attenuation values combined with characteristic streaking) and movement artefacts; in addition, it does not provide actual HU [108, 109]. Although [110] established a strong correlation between HU in MSCT and CT numbers in CBCT, their findings were based on the inaccurate assumption of a uniform relationship between X-ray attenuation and CT number through the CBCT image volume. Scattered radiation and beam hardening lead to CT number inhomogeneity [111]. On the other hand, since the electron density phantom and abdominal phantom differ in their dimensions and composition, scatter produced from both phantoms may affect CT numbers differently. In [112], the authors found that adding scatter longitudinally (by increasing phantom length) has a noticeable effect on CT number values (for example, increasing up to approximately 260 HU in high-density materials when modifying phantom length from 5 cm to scan length [16 cm]), although this effect is much less profound than when adding radial scatter (by changing phantom diameter). Once the scan length was covered, the influence of the longitudinal scatter on CT numbers was reduced. These images were acquired using On-Board Imager™ (OBI, Varian Medical Systems) version 1.4 (half-fan mode). In [113], the authors indicated that full scatter condition is necessary when obtaining the conversion from CT numbers to density for a CBCT (OBI, Varian Medical Systems) in order to have a better dose estimation using photon beams, especially in regions with large inhomogeneity. There is an extended version of the electron density phantom used in our study specifically designed for CBCTs (model 062MA). This phantom (dimensions 33 x 27 x 25 cm) contains other slabs of Plastic Water that allow full scatter of cone-beam X-rays. A stoichiometric calibration with this type of phantom together with a reconstruction method that included beam hardening and scatter corrections achieved a better CT number accuracy in CBCT images of head and neck phantoms using OBI version 1.4 (Varian Medical Systems)

[114]. Our study did not include full scatter condition for the CBCTs devices (O-arm and TrueBeam). Nevertheless, TrueBeam results were good enough as the percentage of voxels fulfilling gamma criteria was above to 95% for most cases. In the case of the O-arm, acquiring the extended version of the electron density phantom would not fix its low gamma pass rates since it is not the main cause for that mismatch. Even after the CT number adjustment, O-arm values of analogous tissues in the electron density phantom and abdominal phantom images differ. This mismatch may be associated with the truncation artefact. Neither the electron density phantom (dimensions 33 x 27 x 5 cm) nor the abdominal phantom (28 x 20 x 12.5 cm) was completely scanned with the O-arm owing to its reduced FOV. CT reconstruction algorithms assume that the detector collects projection data of the whole object in all acquisition angles. Incomplete data from the object leads to truncation artefacts. In this situation, true linear attenuation coefficients cannot be calculated and it is not possible to obtain actual HU [115]. In fact, CT numbers from CBCT images of the same object differ depending on the FOV [116]. Any object that does not fit within the scanner FOV (large patients, retractors or the articulated arm that fixes the position of the applicator) can potentially generate truncation artefacts and thus lead to incorrect dose distributions.

While our analysis of imaging possibilities during IOERT is encouraging, several issues still need to be addressed. Firstly, reproducibility and long stability of the CT number to physical density conversion for each evaluated device have not been assessed. In this study, images of the electron density phantom and the abdominal phantom were acquired with the same acquisition parameters (excepting matrix size) and within the same day for each evaluated device. This is important since tube voltage, collimation and filter type affect CT values (Synergy X-ray volume imaging [XVI], Elekta AB, Sweden) [99] while exposure has a small impact (Trilogy system, Varian Medical Systems) [117]. In [118], the authors pointed out that the stability of the calibration curve to transform CT number into density is system-dependent. For example, the XVI system mounted on a Elekta Synergy LINAC should be calibrated periodically because of a possible change in sensitivity of the flat panel detector (1-year evaluation period) [118]. On the other hand, the OBI calibration curve of the

Varian Trilogy LINAC showed very slight changes (6-month evaluation period) [119]. Recommendations from the Task Group 66 (TG–66) AAPM establish that the CT number to density conversion should be evaluated at least annually or after a scanner calibration in the case of CT simulators [104]. Secondly, in the case of the pancreatic tumour, two shielding discs were virtually placed between the CTV and the right kidney. These protections would generate metal artefacts (severe streaking) that will substantially modify CT numbers, so the dose distribution estimated with intraoperative CT images of this IOERT scenario would be incorrect. Surgical retractors also produce this type of artefacts. Some ideas to get through this problem could be replacing the CT numbers that are affected by the metal artefact by their corresponding CT numbers in the preoperative images or, in the case of the retractors, removing these devices from the surgical scenario or replacing them with other surgical instruments that do not generate this artefact just before acquiring the intraoperative image. Despite these drawbacks, intraoperative images would provide useful information about the actual treatment field for radiation oncologists and medical physicists.

6.5 CONCLUSIONS

We assessed three kV CT imaging systems that can be used to acquire intraoperative images and thus update IOERT according to actual conditions. The evaluation was based on the comparison of dose distributions calculated with phantom images obtained for each of the CT devices under evaluation and for a CT simulator (gold standard). The results reveal that a portable CT (BodyTom) and even a LINAC with on-board kV CBCT (TrueBeam) would be suitable for this purpose. Owing to its reduced FOV (leading to truncation artefacts), the O-arm system produced the worst matching. Our results show the ability of the other two intraoperative imaging CT devices (TrueBeam and BodyTom) to estimate the IOERT dose. This information would be useful for intraoperative planning and for registering and evaluating the treatment administered to the patient.

7 DISCUSSION

In this thesis, we have proposed and evaluated new approaches to improve the existing information on the actual IOERT treatment delivered to the patient. Currently, this procedure is based on assumptions such as the irradiated tissue is equivalent to water in both stopping power and scattering power, and the bevel is in contact with the patient's surface (thus the end of the applicator is parallel to the surface). However, surgical access, tumour resection, patient's heterogeneous tissues and IOERT treatment set-up may invalidate these assumptions.

Several studies have pointed out the need of intraoperative imaging to check applicator placement and to calculate 3D dose distributions before radiation delivery, and the need of further research to evaluate the effect of not fulfilling previous IOERT assumptions [43, 52]. In-vivo dosimetry allows point and 2D dose measurements to register the actual treatment administered to the patient. For instance, in vivo 2D dose distributions obtained from radiochromic films have shown results along the irradiated surface in pelvis IOERTs that did not correspond to expected values [10]. However, no data of the actual IOERT 3D scenario is available (for example, the applicator pose in relation to the patient's anatomy or the irregularities in the irradiated surface) and consequently only a rough approximation of the real IOERT treatment administered to the patient can be estimated. This information would be useful for patient follow-up, for dose accumulation when EBRT is applied after an IOERT boost and for prospective trials such as ELIOT trial where the authors pointed out the difficulty when delimiting the suitable coverage of the tumour bed.

Our first specific study focused on assessing the feasibility of using a multi-camera optical tracking system (OTS) to obtain the applicator pose in IOERT scenarios. Results showed that the accuracy of the applicator pose was below 2 mm in position (mean error of the bevel centre) and 2º in orientation (mean error of the bevel axis and the longitudinal axis), which are within the acceptable range proposed in the recommendation of Task Group 147 (TG–147) (commissioned by the Therapy

Committee and the Quality Assurance and Outcomes Improvement Subcommittee of the AAPM to study the localization accuracy with non-radiographic methods such as infrared systems in external beam radiation therapy). This may be considered to be a lower limit as the study was carried out with an idealised and simplified patient. The advantages of this approach are that applicator movements are tracked and 3D dose distributions can be updated taking account of the pose of the applicator before radiation delivery. The multi-camera OTS was also tested in real IOERT scenarios by our group [120]. A preoperative CT image with several radiopaque markers on the patient's surface (for physical-to-image space registration) was acquired just before IOERT. There were no complications related to the integration of applicator tracking into the IOERT protocol. There is another approach to obtain applicator pose as that recently described in [95]. The authors (in collaboration with our group) presented a phantom study where the applicator pose was estimated from C-arm projections of the IOERT scenario (applicator placed on an extremity phantom). The limitation of our multi-camera OTS solution is that the actual pose of applicator is superimposed on a patient's preoperative image, thus influencing applicator pose accuracy. The solution with C-arm projections would allow updating the preoperative image with intraoperative data but another applicator pose would need extra projections, thus more radiation exposure to the patient/medical personnel. Our solution could be combined with an intraoperative CT image and that data would also be used to estimate 3D dose distributions. Hence, the rest of the thesis focused on intraoperative CT imaging in IOERT scenarios.

Regarding the second specific objective of this thesis, there were no complications in the whole procedure related to the transport step using the subtable and its stretcher, or the acquisition of intraoperative CT images in the CT simulator room (for example, anaesthetic stability or other clinical relevant observations). The 3D dose distributions estimated with the intraoperative images (*gold standard*) showed differences with respect to those corresponding to water assumption (for example, gamma pass rates of 38.9% in the worst case [Monte Carlo, 3D gamma criteria of 5%/2 mm and dose values greater than 70%]). From all the presented experiments we concluded that preoperative CT images can be used to estimate the IOERT dose distribution under two conditions:

knowing the applicator pose in relation to the patient's anatomy (specifically to the bones) and incorporating information regarding the air gap between the end of the applicator and the tumour bed (and, therefore, the surface irregularities of the irradiated area). Moreover, the dominant factor in IOERT dose estimation is the air gap and the surface irregularities, not tissue heterogeneities. This assessment may not be valid, for example, in rectal cancer IOERT since the tumour bed is very close to the sacrum or in breast cancer cases where the tumour bed is close to the shielding discs, ribs and lung. In the evaluated IOERT cases, bones and lungs were not critical tissues as they were at a certain distance from the tumour bed. The limitations of acquiring intraoperative CT images for estimation 3D dose distributions are metal artefacts caused by shielding discs (breast cancer cases) or surgical retractors that substantially modified HU. A solution would be replacing the incorrect CT values with the corresponding ones from the registered preoperative image.

Our third specific study focused on assessing several kV CT technologies other than CT simulators to acquire intraoperative images for estimating IOERT dose distribution. That would be necessary when a mobile electron LINAC was available in the OR as transferring the patient to the CT simulator room could not be approved. Our results with an abdominal phantom revealed that a portable CT (BodyTom) and even a LINAC with on-board kV CBCT (TrueBeam) would be suitable for this purpose. Using the TrueBeam approach, it would be necessary to transfer the patient from the OR to the LINAC room or alternatively the surgery could be performed in the LINAC facility, thus avoiding transportation. Intraoperative CT images could be used to register the actual treatment administered to the patient or combined with an OTS when the applicator is not acquired in those images. The cost of these devices is the variable that may limit their use in most institutions. Other intermediate approach would be acquiring the irradiation surface to update preoperative CT images with this intraoperative data or even, looking at the results of the second specific study, to estimate dose distributions from a new image that is set to air above that surface (–1000 HU) and to water below that surface (0 HU). This surface could be acquired with a structured-light 3D scanner [121] (phantom study with a torso and several objects) or with a conoscopic holography device [96] (phantom study done by our

group with a breast phantom, a container with bloody fluid and other phantoms). In these solutions it would be necessary to know the applicator pose in relation to the patient's anatomy by using a tracking system.

In IOERT, there is not a general approach that allows registering the whole radiotherapy procedure in all scenarios. As previously mentioned, intraoperative CT images are considered to be the *gold standard* to estimate dose distributions but CT images that include shielding discs (for example, in breast IOERT) or retractors cannot be directly used for dose estimation due to metal artefacts. For instance, in those breast cancer cases, an applicator system that assures the alignment of applicator/target/shielding discs [92] would reduce the air gap between the end of the applicator and the tumour bed. However, this approach would not provide data regarding dose distribution. Research is necessary in IOERT to know the actual treatment administered to the patient and put IOERT and EBRT at the same level in terms of planning and dose recording.

8 CONCLUSIONS

The main contributions and conclusions of this thesis are as follows:

- A multi-camera optical tracking system was proposed to obtain the applicator pose in IOERT since this complex clinical scenario obstructs the required line-of-sight between the tracked objects and the cameras. Errors when testing this solution in an end-to-end phantom study were 1.8 mm in position (mean error of the bevel centre), 1.6º in rotation around the bevel axis (mean error) and 0.7º in rotation around the longitudinal axis (mean error). These values were within the acceptable range proposed in the TG–147 recommendation.
- We have demonstrated that acquiring intraoperative CT images with a CT simulator when transferring the patient from the OR to the LINAC room was feasible. These intraoperative images, when metal artefacts were not present, allowed estimating 3D dose distributions.
- We found that gamma pass rates improved from 38.9% to 96.2% (worst case) mainly when adding the air gap between the end of the applicator and the tumour bed (and, therefore, the surface irregularities of the irradiated area) to the preoperative images.
- In IOERT scenarios where bones and lungs are at a certain distance from the tumour bed, we also demonstrated that the dominant factor in dose estimation is the air gap between the bevel and the irradiated surface, not tissue heterogeneities.
- We proposed three kV CT imaging systems other than CT simulators to acquire intraoperative images in the IOERT framework. A portable CT (BodyTom) and even a LINAC with on-board kV CBCT (TrueBeam) showed gamma pass rates greater than 95% in most comparisons. On the other hand, an O-arm system revealed worst results (below 75% in both simulated IOERT cases) due to its reduced FOV (leading to truncation artefacts). Therefore, the first two devices would be suitable for estimating 3D dose distributions in IOERT scenarios.

9 FUTURE LINES

Possible future lines of research derived from this thesis are as follows:

- To include a figure of merit of the tracking process for the interactive assessment of the data collected by the multi-camera OTS.
- To explore correcting intraoperative images that are affected by metal artefacts to estimate 3D dose distributions. One approach is to replace uncorrected CT values with the corresponding ones from the registered preoperative image or even with the mean CT values of certain regions from the contralateral side.
- To carry out a phantom study to evaluate the error when estimating the 3D dose distribution with an image created from the surface of the tumour bed. This is an intermediate solution between the conventional assumption of having just water at the end of the applicator and acquiring an intraoperative CT image.
- To assess the influence of adding scatter to the images of the on-board kV CBCT (TrueBeam) and its effect on IOERT doses.
- To assess the reproducibility and long stability of the CT number to physical density conversion for the portable CT (BodyTom) and the on-board kV CBCT (TrueBeam).

10 PUBLICATIONS

10.1 DIRECTLY RELATED TO THIS THESIS

Articles

García-Vázquez V, Marinetto E, Santos-Miranda JA, Calvo FA, Desco M, Pascau J. Feasibility of integrating a multi-camera optical tracking system in intra-operative electron radiation therapy scenarios. *Physics in Medicine and Biology*, 2013. 58(24):8769–8782.

García-Vázquez V. Review of article "Feasibility of integrating a multi-camera optical tracking system in intra-operative electron radiation therapy scenarios". *Revista de Física Médica*, 2014. 15(1):65–66.

Valdivieso-Casique MF, Rodríguez R, Rodríguez-Bescós S, Lardíes D, Guerra P, Ledesma MJ, Santos A, Ibáñez P, Vidal M, Udías JM, Otaduy MA, Calama JA, López-Tarjuelo J, Santos-Miranda JA, Desco M, **García-Vázquez V**, Marinetto E, Pascau J, Calvo F, Illana C. RADIANCE – A planning software for intra-operative radiation therapy. *Translational Cancer Research*, 2015. 4(2):196–209.

García-Vázquez V, Marinetto E, Guerra P, Valdivieso-Casique MF, Calvo FA, Alvarado-Vásquez E, Solé CV, Vosburgh KG, Desco M, Pascau J. Assessment of intraoperative 3D imaging alternatives for IOERT dose estimation. *Zeitschrift für Medizinische Physik*, 2016. In press, corrected proof.

Brudfors M, **García-Vázquez V**, Sesé-Lucio B, Marinetto E, Desco M, Pascau J. ConoSurf: open-source 3D scanning system based on a conoscopic holography device for acquiring surgical surfaces. *The International Journal of Medical Robotics and Computer Assisted Surgery*, 2016. Version of record online: 21 November 2016.

Conferences

García-Vázquez V, Marinetto E, Santos-Miranda JA, Calvo FA, Camacho-Márquez A, Desco M, Pascau J. Estudio de la viabilidad de la integración de un sistema de posicionamiento óptico en el entorno de la radioterapia intraoperatoria. *Libro de actas del XXIX Congreso Anual de la Sociedad Española de Ingeniería Biomédica (CASEIB)*, 2011. 307–310.

Pascau J, Santos-Miranda J, González San-Segundo C, Illana C, Valdivieso M, **García-Vázquez V**, Marinetto E, Calvo F, Desco M. Intraoperative imaging in IOERT sarcoma treatment: initial experience in two clinical cases. *International Journal of Radiation Oncology*, 2011. 81(2):S90.

García-Vázquez V, Marinetto E, Santos-Miranda JA, Calvo F, Camacho-Márquez L, Illana C, Desco M, Pascau J. Towards a real scenario in intra-operative electron radiation therapy. *International Journal of Computer Assisted Radiology and Surgery*, 2012. 7(Supplement 1):S64–S65.

García-Vázquez V, San José Estépar R, Colen RR, Jayender J, Walsh CR, Lapidus M, Pascau J, Desco M, Raut CP, Vosburgh KG. Toward optimum resection margins: preliminary studies in soft-tissue sarcoma surgery. *International Journal of Computer Assisted Radiology and Surgery*, 2012. 7(Supplement 1):S436–S437.

Marinetto E, **García-Vázquez V**, Santos-Miranda JA, Calvo F, Valdivieso M, Illana C, Desco M, Pascau J. Optical tracking system integration into IORT treatment planning system. *International Federation for Medical and Biological Engineering Proceedings*, 2013. 41:37–40.

Calvo FA, Marinetto E, **García-Vázquez V**, Santos-Miranda JA, Solé C, Desco M, Pascau J. Stereotactic image-guided intraoperative electron irradiation: proof of concept and clinical feasibility. *Radiotherapy & Oncology*, 2014. 111(Supplement 1):377.

García-Vázquez V, Marinetto E, Calvo FA, Alvarado E, Santos-Miranda JA, Desco M, Pascau J. Evaluation of intraoperative imaging alternatives for IOERT. *8th International Conference of Intraoperative Radiotherapy (ISIORT)*, 2014.

Marinetto E, **García-Vázquez V**, Santos-Miranda JA, Calvo FA, Desco M, Pascau J. Image-guided intraoperative electron irradiation: clinical set-up and feasibility. *8th International Conference of Intraoperative Radiotherapy (ISIORT)*, 2014.

Calvo FA, Alvarado-Vásquez E, Gómez-Espí M, Alvarez A, Serrano J, Blanco JA, González C, Calin A, Muñoz M, Salas B, Araque J, **Garcia V**, Lozano MA. Promoting quality and safety in intraoperative radiotherapy: lessons learned with the use of innovative technology. *8th International Conference of Intraoperative Radiotherapy (ISIORT)*, 2014.

Calvo FA, Alvarado-Vásquez E, Gómez-Espí M, Alvarez A, Serrano J, Blanco JA, González C, Calin A, Muñoz M, Araque J, Salas B, **Garcia V**, Pascau J, Lozano MA. Concordance between PRE and POST procedure parameters using a virtual planning system in clinical practice: the use of Radiance. *8th International Conference of Intraoperative Radiotherapy (ISIORT)*, 2014.

Marinetto E, **García-Vázquez V**, Santos-Miranda JA, Calvo FA, Sanz-Díaz L, Solé CV, Desco M, Pascau J. Radioterapia intraoperatoria guiada por imagen: entorno clínico y viabilidad. *Libro de actas del XXXII Congreso Anual de la Sociedad Española de Ingeniería Biomédica (CASEIB)*, 2014.

García-Vázquez V, Marinetto E, Guerra P, Valdivieso MF, Calvo FA, Alvarado-Vásquez E, Santos-Miranda JA, Sole CV, Desco M, Pascau J. Alternatives for intraoperative imaging in IOERT. *International Journal of Computer Assisted Radiology and Surgery*, 2015. 7(Supplement 1):S38–S39.

Goswami SS, Ortuño Fisac JE, Wollny G, **García-Vázquez V**, Marinetto E, Santos Lleó A, Pascau J, Ledesma Carbayo MJ. A new workflow for image guided intraoperative radiotherapy using fluoroscopy based pose tracking. *International Journal of Computer Assisted Radiology and Surgery*, 2015. 7(Supplement 1):S201–S203.

Sesé-Lucio B, **García-Vázquez V**, Sanz-Díaz L, Desco M, Pascau J. Desarrollo de un sistema de escaneado 3D a partir de un dispositivo de holografía conoscópica.

Libro de actas del XXXIII Congreso Anual de la Sociedad Española de Ingeniería Biomédica (CASEIB), 2015.

García-Vázquez V, Rodríguez-Lozano G, Pérez-Mañanes R, Calvo JA, García-Mato D, Cuervo-Dehesa M, Desco M, Pascau J, Vaquero J. Desktop 3D printing in medicine to improve surgical navigation in acral tumors. *International Journal of Computer Assisted Radiology and Surgery*, 2016. 11(Supplement 1):S262–S263.

10.2 OTHER PUBLICATIONS

Articles

Janssen J, Reig S, Parellada M, Moreno D, Graell M, Fraguas D, Zabala A, **García Vázquez V**, Desco M, Arango C. Regional gray matter volume deficits in adolescents with first-episode psychosis. *Journal of the American Academy of Child and Adolescent Psychiatry*, 2008. 47(11):1311–1320.

Janssen J, Díaz-Caneja A, Reig S, Bombín I, Mayoral M, Parellada M, Graell M, Moreno D, Zabala A, **García-Vázquez V**, Desco M, Arango C. Brain morphology and neurological soft signs in adolescents with first-episode psychosis. *British Journal of Psychiatry*, 2009. 195(3):227–233.

Higuera-Matas A, Soto-Montenegro ML, Montoya GL, **García-Vázquez V**, Pascau J, Miguéns M, Del Olmo N, Vaquero JJ, García-Lecumberri C, Desco M, Ambrosio E. Chronic cannabinoid administration to periadolescent rats modulates the metabolic response to acute cocaine in the adult brain. *Molecular Imaging and Biology*, 2011. 13(3):411–415.

Abella M, Vaquero JJ, Sisniega A, Pascau J, Udías A, **García V**, Vidal I, Desco M. Software architecture for multi-bed FDK-based reconstruction in X-ray CT scanners. *Computer Methods and Programs in Biomedicine*, 2012. 107(2):218–232.

Martino ME, Guzmán de Villoria J, Lacalle-Aurioles M, Olazarán J, Cruz I, Navarro E, **García-Vázquez V**, Carreras JL, Desco M. Comparison of different

methods of spatial normalization of FDG-PET brain images in the voxel-wise analysis of MCI patients and controls. *Annals of Nuclear Medicine*, 2013. 27(7):600–609.

Cussó L, Mirones I, Peña-Zalbidea S, **García-Vázquez V**, García-Castro J, Desco M. Combination of single-photon emission computed tomography and magnetic resonance imaging to track 111In-oxine-labeled human mesenchymal stem cells in neuroblastoma-bearing mice. *Molecular Imaging*, 2014. 13(10).

Chavarrías C, **García-Vázquez V**, Alemán-Gómez Y, Montesinos P, Pascau J, Desco M. fMRat: an extension of SPM for a fully automatic analysis of rodent brain functional magnetic resonance series. *Medical & Biological Engineering & Computing*, 2016. 54(5):743–752.

Conferences

García-Vázquez V, Reig S, Janssen J, Pascau J, Rodríguez-Ruano A, Udías A, Chamorro J, Vaquero JJ, Desco M. Use of IBASPM atlas-based automatic segmentation toolbox in pathological brains: effect of template selection. *IEEE Nuclear Science Symposium Medical Imaging Conference and 16th Room-Temperature Semiconductor Detector Workshop Conference Record*, 2008. 4270–4272.

García-Vázquez V, Chamorro-Servent J, Rodríguez-Ruano A, Benito M, Tejedor Fraile J, Carrillo Salinas FJ, Montoliu L, Desco M. Mouse eyeball's axial length measurement with MRI. *Abstract Book of the 4th European Society for Molecular Imaging Meeting*, 2009. 164.

García-Vázquez V, Montoya GL, Soto-Montenegro ML, Pascau J, Higuera-Matas A, Benito M, Ambrosio E, Desco M. Análisis de imágenes PET utilizando SPM: aplicación en estudios sobre drogas. *Libro de actas del XXVIII Congreso Anual de la Sociedad Española de Ingeniería Biomédica (CASEIB)*, 2010. 245.

García-Vázquez V, Reig S, Seijas-Leal O, Gómez de Liaño P, Merino P, Franco Iglesias G, Guzmán de Villoria J, Pascau J, Cortés C, Desco M. Software toolbox to assist surgical planning of oculomotor dysfunctions by biometric analysis of ocular muscles in MR images. *International Journal of Computer Assisted Radiology and Surgery*, 2010. 5(Supplement 1):S31–S33.

García-Vázquez V, Cussó L, Chamorro-Servent J, Mirones I, García-Castro J, López-Sánchez L, Peña-Zalbidea S, Montesinos P, Chavarrías C, Pascau J, Desco M. Registration of small-animal SPECT/MRI studies for tracking human mesenchymal stem cells. *International Federation for Medical and Biological Engineering Proceedings*, 2013. 41:399–402.

11 REFERENCES

[1] Calvo FA, Meirino RM, Orecchia R. Intraoperative radiation therapy – First part: rationale and techniques. *Critical Reviews in Oncology/Hematology*, 2006. **59**(2):106–115.

[2] Pascau J, Santos Miranda JA, Calvo FA, Bouché A, Morillo V, González-San Segundo C, Ferrer C, López Tarjuelo J, Desco M. An innovative tool for intraoperative electron beam radiotherapy simulation and planning: description and initial evaluation by radiation oncologists. *International Journal of Radiation Oncology • Biology • Physics*, 2012. **83**(2):e287–e295.

[3] Valdivieso-Casique MF, Rodríguez R, Rodríguez-Bescós S, Lardíes D, Guerra P, Ledesma MJ, Santos A, Ibáñez P, Vidal M, Udías JM, Otaduy MA, Calama JA, López-Tarjuelo J, Santos-Miranda JA, Desco M, García-Vázquez V, Marinetto E, Pascau J, Calvo F, Illana C. RADIANCE – A planning software for intra-operative radiation therapy. *Translational Cancer Research*, 2015. **4**(2):196–209.

[4] Hanna SA, de Barros ACSD, de Andrade FEM, Bevilacqua JLB, Piato JRM, Pelosi EL, Martella E, da Silva JLF, Carvalho HdA. Intraoperative radiation therapy in early breast cancer using a linear accelerator outside of the operative suite: an "image-guided" approach. *International Journal of Radiation Oncology • Biology • Physics*, 2014. **89**(5):1015–1023.

[5] Schlager B, Harris JM, Reiland J, Fastner G, Sedlmayer F. Image guided quality assurance technique for intraoperative electron beam radiotherapy (IOERT) as a boost dose in early stage breast cancer treated with breast conserving therapy. *8th International Conference of Intraoperative Radiotherapy*, 2014.

[6] Severgnini M, Urbani M, Bortul M, Vidali C, Aslian H, Beorchia A, de Denaro M. The role of intraoperative ultrasound in improving quality and reducing risk in breast IOERT. *European Journal of Cancer*, 2016. **57**(Supplement 2):S50.

[7] Ciocca M, Orecchia R, Garibaldi C, Rondi E, Luini A, Gatti G, Intra M, Veronesi P, Lazzari R, Tosi G, Veronesi U. In vivo dosimetry using radiochromic films during intraoperative electron beam radiation therapy in early-stage breast cancer. *Radiotherapy and Oncology*, 2003. **69**(3):285–289.

[8] Consorti R, Petrucci A, Fortunato F, Soriani A, Marzi S, Iaccarino G, Landoni V, Benassi M. In vivo dosimetry with MOSFETs: dosimetric characterization and first clinical results in intraoperative radiotherapy. *International Journal of Radiation Oncology • Biology • Physics*, 2005. **63**(3):952–960.

[9] Lemanski C, Azria D, Gourgou-Bourgade S, Ailleres N, Pastant A, Rouanet P, Fenoglietto P, Dubois JB, Gutowski M. Electrons for intraoperative radiotherapy in selected breast-cancer patients: late results of the Montpellier phase II trial. *Radiation Oncology*, 2013. **8**:191.

[10] Costa F, Sarmento S, Gomes D, Magalhães H, Arrais R, Moreira G, Cruz MF, Silva JP, Santos L, Sousa O. In vivo dosimetry using Gafchromic films during pelvic intraoperative electron radiation therapy (IOERT). *The British Journal of Radiology*, 2016. **89**(1063):20160193.

[11] López-Tarjuelo J, Morillo-Macías V, Bouché-Babiloni A, Boldó-Roda E, Lozoya-Albacar R, Ferrer-Albiach C. Implementation of an intraoperative electron radiotherapy in vivo dosimetry program. *Radiation Oncology*, 2016. **11**:41.

[12] Costa F, Sarmento S, Sousa O. Assessment of clinically relevant dose distributions in pelvic IOERT using Gafchromic EBT3 films. *Physica Medica: European Journal of Medical Physics*, 2015. **31**(7):692–701.

[13] Global status report on noncommunicable diseases 2014: World Health Organization. Available from: http://www.who.int.

[14] Wyatt D, Hulbert-Williams N. Cancer and cancer care. SAGE Publications, 2015.

[15] Washington CM, Leaver DT. Principles and practice of radiation therapy. Elsevier - Health Sciences Division, 2015.

[16] Chen X, Wong S. Cancer Theranostics. Elsevier Science, 2014.

[17] Nag S, Willett CG, Gunderson LL, Harrison LB, Calvo FA, Biggs P. IORT with electron-beam, high-dose-rate brachytherapy or low-kV/electronic brachytherapy: methodological comparisons. Editors: Gunderson LL, Willett CG, Calvo FA, Harrison LB. *Intraoperative Irradiation: Techniques and Results.* New York: Humana Press, 2011. 99–115.

[18] Gunderson LL, Calvo FA, Willett CG, Harrison LB. Rationale and historical perspective of intraoperative irradiation. Editors: Gunderson LL, Willett CG, Calvo FA, Harrison LB. *Intraoperative Irradiation: Techniques and Results.* New York: Humana Press, 2011. 3–26.

[19] Hershko D, Abdah-Bortnyak R, Nevelsky A, Gez E, Fried G, Kuten A. Breast-conserving surgery and intraoperative electron radiotherapy in early breast cancer: experience at the Rambam health care campus. *Israel Medical Association Journal*, 2012. **14**(9):550–554.

[20] Biggs P, Willett CG, Rutten H, Ciocca M, Gunderson LL, Calvo FA. Intraoperative electron beam irradiation: physics and techniques. Editors: Gunderson LL, Willett CG, Calvo FA, Harrison LB. *Intraoperative Irradiation: Techniques and Results.* New York: Humana Press, 2011. 51–72.

[21] Palta JR, Biggs PJ, Hazle JD, Huq MS, Dahl RA, Ochran TG, Soen J, Dobelbower RR Jr, McCullough EC. Intraoperative electron beam radiation therapy: technique, dosimetry, and dose specification: report of task force 48 of the radiation therapy committee, American Association of Physicists in Medicine. *International Journal of Radiation Oncology • Biology • Physics*, 1995. **33**(3):725–746.

[22] Krengli M, Calvo FA, Sedlmayer F, Sole CV, Fastner G, Alessandro M, Maluta S, Corvò R, Sperk E, Litoborski M, Pisani C, Fillini C, Fusconi F, Osti MF, Tomio L, Marsiglia H, Ciabattoni A, Polkowski W, Di Grazia A, Gava A, Kuten A, Iotti C, Gonzalez C, Sallabanda M, Dubois JB, Catalano G, Valentini V. Clinical and technical characteristics of intraoperative radiotherapy. Analysis of the ISIORT-Europe database. *Strahlentherapie und Onkologie*, 2013. **189**(9):729–737.

[23] Istituto Superiori di Sanità. Guidelines for quality assurance in intra-operative radiation therapy. *Oncología*, 2004. **27**(7):442–475.

[24] Calvo FA, Sole CV, González ME, Tangco ED, López-Tarjuelo J, Koubychine I, Santos JA, Pascau J, Herranz R, Ferrer C. Research opportunities in intraoperative radiation therapy: the next decade 2013–2023. *Clinical and Translational Oncology*, 2013. **15**(9):683–690

[25] Maluta S, Dall'Oglio S, Marciai N, Gabbani M, Franchini Z, Pietrarota P, Meliadò G, Guariglia S, Cavedon C. Accelerated partial breast irradiation using only intraoperative electron radiation therapy in early stage breast cancer. *International Journal of Radiation Oncology • Biology • Physics*, 2012. **84**(2):e145–e152.

[26] Veronesi U, Orecchia R, Maisonneuve P, Viale G, Rotmensz N, Sangalli C, Luini A, Veronesi P, Galimberti V, Zurrida S, Leonardi MC, Lazzari R, Cattani F, Gentilini O, Intra M, Caldarella P, Ballardini B. Intraoperative radiotherapy versus external radiotherapy for early breast cancer (ELIOT): a randomised controlled equivalence trial. *The Lancet Oncology*, 2013. **14**(13):1269–1277.

[27] Silverstein MJ, Fastner G, Maluta S, Reitsamer R, Goer DA, Vicini F, Wazer D. Intraoperative radiation therapy: a critical analysis of the ELIOT and TARGIT trials. Part 1 – ELIOT. *Annals of Surgical Oncology*, 2014. **21**(12):3787–3792.

[28] Pawlicki T, Scanderbeg DJ, Starkschall G. Hendee's radiation therapy physics. Wiley, 2016.

[29] Khan FM, Gibbons JP. Khan's the physics of radiation therapy. Wolters Kluwer Health, 2014.

[30] Podgorsak EB. Radiation physics for medical physicists. Springer Berlin Heidelberg, 2010.

[31] Lax I, Brahme A. Collimation of high energy electron beams. *Acta Radiologica: Oncology*, 1980. **19**(3):199–207.

[32] Strydom W, Parker W, Olivares M. Electron beams: physical and clinical aspects. Editor: Podgorsak EB. *Radiation Oncology Physics: a Handbook for Teachers and Students.* Vienna: International Atomic Energy Agency, 2005. 273–299.

[33] Biggs PJ. Radiotherapy, intraoperative. Editor: Webster JG. *Encyclopedia of Medical Devices and Instrumentation, Volume 6.* Hoboken: Wiley, 2006. 13–29.

[34] Valentini V, Balducci M, Tortoreto F, Morganti AG, De Giorgi U, Fiorentini G. Intraoperative radiotherapy: current thinking. *European Journal of Surgical Oncology*, 2002. **28**(2):180–185.

[35] Catalano M, Agosteo S, Moretti R, Andreoli S. Montecarlo simulation code in optimisation of the intraoperative radiation therapy treatment with mobile dedicated accelerator. *Journal of Physics: Conference Series*, 2007. **74**(1):012002.

[36] Khan FM, Doppke KP, Hogstrom KR, Kutcher GJ, Nath R, Prasad SC, Purdy JA, Rozenfeld M, Werner BL. Clinical electron-beam dosimetry: report of AAPM radiation therapy committee task group no. 25. *Medical Physics*, 1991. **18**(1):73–109.

[37] Baghani HR, Aghamiri SMR, Mahdavi SR, Akbari ME, Mirzaei HR. Comparing the dosimetric characteristics of the electron beam from dedicated intraoperative and conventional radiotherapy accelerators. *Journal of Applied Clinical Medical Physics*, 2015. **16**(2):62-72.

[38] Low DA, Harms WB, Mutic S, Purdy JA. A technique for the quantitative evaluation of dose distributions. *Medical Physics*, 1998. **25**(5):656–661.

[39] Ezzell GA, Burmeister JW, Dogan N, LoSasso TJ, Mechalakos JG, Mihailidis D, Molineu A, Palta JR, Ramsey CR, Salter BJ, Shi J, Xia P, Yue NJ, Xiao Y. IMRT commissioning: multiple institution planning and dosimetry comparisons, a report from AAPM task group 119. *Medical Physics*, 2009. **36**(11):5359–5373.

[40] Bak J, Choi JH, Kim JS, Park SW. Modified dose difference method for comparing dose distributions. *Journal of Applied Clinical Medical Physics*, 2012. **13**(2):73–80.

[41] Gunderson LL, Ashman JB, Haddock MG, Petersen IA, Moss A, Heppell J, Gray RJ, Pockaj BA, Nelson H, Beauchamp C. Integration of radiation oncology with surgery as combined-modality treatment. *Surgical Oncology Clinics of North America*, 2013. **22**(3):405–432.

[42] Gerbi BJ, Antolak JA, Deibel FC, Followill DS, Herman MG, Higgins PD, Huq MS, Mihailidis DN, Yorke ED, Hogstrom KR, Khan FM. Recommendations for clinical electron beam dosimetry: supplement to the recommendations of task group 25. *Medical Physics*, 2009. **36**(7):3239–3279.

[43] Beddar AS, Biggs PJ, Chang S, Ezzell GA, Faddegon BA, Hensley FW, Mills MD. Intraoperative radiation therapy using mobile electron linear accelerators: report of AAPM radiation therapy committee task group no. 72. *Medical Physics*, 2006. **33**(5):1476–1489.

[44] Russo G, Casarino C, Arnetta G, Candiano G, Stefano A, Alongi F, Borasi G, Messa C, Gilardi MC. Dose distribution changes with shielding disc misalignments and wrong orientations in breast IOERT: a Monte Carlo – GEANT4 and experimental study. *Journal of Applied Clinical Medical Physics*, 2012. **13**(5):74–92.

[45] Calandrino R, Del Maschio A, Cattaneo GM, Castiglioni I. Imaging in radiotherapy. *Nuclear Instruments & Methods in Physics Research Section A, Accelerators, Spectrometers, Detectors and Associated Equipment*, 2009. **608**(1, supplement):S11–S14.

[46] Xing L, Lee L, Timmerman R. Image-guided adaptive radiation therapy and practical perspectives. Editors: Timmerman R, Xing L. *Image-Guided and Adaptive Radiation Therapy.* Philadelphia: Lippincott Williams and Wilkins, 2012. 16–40.

[47] Parker W, Patrocinio H. Clinical treatment planning in external photon beam radiotherapy. Editor: Podgorsak EB. *Radiation Oncology Physics: a Handbook for Teachers and Students.* Vienna: International Atomic Energy Agency, 2005. 219–272.

[48] López-Tarjuelo J, Lardiés M, García-Romero A, Ruiz Rodriguez J, Lavado-Rodríguez E, Calama-Santiago J, Infante-Utrilla M, Ferrer-Albiach C, Sanfeliu-Lucas E. SU-GG-T-98: pencil beam for electron intraoperative radiotherapy. Early results from profile and percentage depth dose modelling. *Medical Physics*, 2010. **37**(6):3206–3207.

[49] Calama Santiago JA, Garcia-Romero A, Lardiés Fleta D, Infante Utrilla MA, Lopez Tarjuelo J, Ferrer Albiach C, Serrano Navarro C, Lavado Rodriguez E. Pencil beam for electron intraoperative radiotherapy. Results of dose calculations in heterogeneous media. *Radiotherapy and Oncology*, 2011. **99**(Supplement 1):S13.

[50] Guerra P, Udías JM, Herranz E, Santos-Miranda JA, Herraiz JL, Valdivieso MF, Rodríguez R, Calama JA, Pascau J, Calvo FA, Illana C, Ledesma-Carbayo MJ, Santos A. Feasibility assessment of the interactive use of a Monte Carlo algorithm in treatment planning for intraoperative electron radiation therapy. *Physics in Medicine and Biology*, 2014. **59**(23):7159–7179.

[51] Nahum A. Patient dose computation for electron beams. Editors: Mayles P, Nahum A, Rosenwald JC. *Handbook of Radiotherapy Physics: Theory and Practice.* CRC Press, 2007. 587–601.

[52] Trifiletti DM, Jones R, Showalter SL, Libby BB, Brenin DR, Schroen A, Morris MM, Reardon KA, Showalter TN. Techniques for intraoperative radiation therapy for early-stage breast carcinoma. *Future Oncology*, 2015. **11**(7):1047–1058.

[53] Showalter SL, Petroni G, Trifiletti DM, Libby B, Schroen AT, Brenin DR, Dalal P, Smolkin M, Reardon KA, Showalter TN. A novel form of breast intraoperative radiation therapy with CT-guided high-dose-rate brachytherapy: results of a prospective phase 1 clinical trial. *International Journal of Radiation Oncology • Biology • Physics*, 2016. **96**(1):46–54.

[54] Verhaegen F, Devic S. Sensitivity study for CT image use in Monte Carlo treatment planning. *Physics in Medicine and Biology*, 2005. **50**(5):937–946.

[55] Schneider U, Pedroni E, Lomax A. The calibration of CT Hounsfield units for radiotherapy treatment planning. *Physics in Medicine and Biology*, 1996. **41**(1):111–124.

[56] Schneider W, Bortfeld T, Schlegel W. Correlation between CT numbers and tissue parameters needed for Monte Carlo simulations of clinical dose distributions. *Physics in Medicine and Biology*, 2000. **45**(2):459–478.

[57] Linte CA. Virtual and augmented medical imaging environments: applications to simulation, training, surgical planning and interventional guidance. Editors: Tavares JMRS, Natal Jorge RM. *Computational Vision and Medical Image Processing V: Proceedings of the 5th Eccomas Thematic Conference on Computational Vision and Medical Image Processing.* CRC Press, 2015. 33–38.

[58] Dewi DEO, Fadzil MM, Faudzi AAM, Supriyanto E, Lai KW. Position tracking systems for ultrasound imaging: a survey. Editors: Lai KW, Dewi DEO. *Medical Imaging Technology: Reviews and Computational Applications.* Springer, 2015. 57–90.

[59] Ahmad N, Ghazilla RAR, Khairi NM. Reviews on various inertial measurement unit (IMU) sensor applications. *International Journal of Signal Processing Systems*, 2013. **1**(2):256–262.

[60] Birkfellner W, Hummel J, Wilson E, Cleary K. Tracking devices. Editors: Peters T, Cleary K. *Image-Guided Interventions: Technology and Applications.* New York: Springer, 2008. 23–44.

[61] Stevens F, Conditt MA, Kulkarni N, Ismaily SK, Noble PC, Lionberger DR. Minimizing electromagnetic interference from surgical instruments on electromagnetic surgical navigation. *Clinical Orthopaedics and Related Research*, 2010. **468**(8):2244–2250.

[62] Seeberger R, Kane G, Hoffmann J, Eggers G. Accuracy assessment for navigated maxillofacial surgery using an electromagnetic tracking device. *Journal of Cranio-Maxillofacial Surgery*, 2012. **40**(2):156–161.

[63] Sarbolandi H, Lefloch D, Kolb A. Kinect range sensing: structured-light versus time-of-flight Kinect. *Computer Vision and Image Understanding*, 2015. **139**:1–20.

[64] Image-Guided Interventions: Technology and Applications. Peters T, Cleary K editors. New York: Springer, 2008.

[65] Spadea MF, Baroni G, Riboldi M, Tagaste B, Garibaldi C, Orecchia R, Pedotti A. Patient set-up verification by infrared optical localization and body surface sensing in breast radiation therapy. *Radiotherapy and Oncology*, 2006. **79**(2):170–178.

[66] Langen KM, Willoughby TR, Meeks SL, Santhanam A, Cunningham A, Levine L, Kupelian PA. Observations on real-time prostate gland motion using electromagnetic tracking. *International Journal of Radiation Oncology • Biology • Physics*, 2008. **71**(4):1084–1090.

[67] Smith RL, Lechleiter K, Malinowski K, Shepard DM, Housley DJ, Afghan M, Newell J, Petersen J, Sargent B, Parikh P. Evaluation of linear accelerator gating with real-time electromagnetic tracking. *International Journal of Radiation Oncology • Biology • Physics*, 2009. **74**(3):920–927.

[68] Alnowami MR, Hagi SK. The battle against respiration-induced organ motion in external beam radiotherapy *Saudi Medical Journal*, 2014. **35**(7):651–662.

[69] Glide-Hurst CK, Chetty IJ. Improving radiotherapy planning, delivery accuracy, and normal tissue sparing using cutting edge technologies. *Journal of Thoracic Disease*, 2014. **6**(4):303–318.

[70] Watanabe Y, Anderson LL. A system for nonradiographic source localization and real-time planning of intraoperative high dose rate brachytherapy. *Medical Physics*, 1997. **24**(12):2014–2023.

[71] García-Vázquez V, Marinetto E, Santos-Miranda JA, Calvo FA, Desco M, Pascau J. Feasibility of integrating a multi-camera optical tracking system in intra-operative electron radiation therapy scenarios. *Physics in Medicine and Biology*, 2013. **58**(24):8769–8782.

[72] Glossop ND. Advantages of optical compared with electromagnetic tracking. *The Journal of Bone and Joint Surgery – American Volume*, 2009. **91**(Supplement 1):23–28.

[73] Willoughby T, Lehmann J, Bencomo JA, Jani SK, Santanam L, Sethi A, Solberg TD, Tome WA, Waldron TJ. Quality assurance for nonradiographic radiotherapy localization and positioning systems: report of task group 147. *Medical Physics*, 2012. **39**(4):1728–1747.

[74] Taylor II RM, Hudson TC, Seeger A, Weber H, Juliano J, Helser AT. VRPN: a device-independent, network-transparent VR peripheral system. *Proceedings of the ACM Symposium on Virtual Reality Software and Technology*, 2001.55–61.

[75] Jansen C, Steinicke F, Hinrichs K, Vahrenhold J, Schwald B. Performance Improvement for Optical Tracking by Adapting Marker Arrangements. *IEEE VR Workshop on Trends and Issues in Tracking for Virtual Environments*, 2007.28–33.

[76] Cleary K, Cheng P, Enquobahrie A, Yaniv Z. IGSTK: the book. http://www.igstk.org, 2009. Accessed August 2011.

[77] Arun KS, Huang TS, Blostein SD. Least-squares fitting of two 3-D point sets. *IEEE Transactions on Pattern Analysis and Machine Intelligence*, 1987. **9**(5):698–700.

[78] Vidal R, Ma Y, Sastry SS. Generalized principal component analysis. Springer New York, 2016.

[79] Maini ES. Enhanced direct least square fitting of ellipses. *International Journal of Pattern Recognition and Artificial Intelligence*, 2006. **20**(6):939–953.

[80] Fitzpatrick JM, West JB, Maurer CR Jr. Predicting error in rigid-body point-based registration. *IEEE Transactions on Medical Imaging*, 1998. **17**(5):694–702.

[81] McNamara JE, Pretorius PH, Johnson K, Mukherjee JM, Dey J, Gennert MA, King MA. A flexible multicamera visual-tracking system for detecting and correcting motion-induced artifacts in cardiac SPECT slices. *Medical Physics*, 2009. **36**(5):1913–1923.

[82] Li HS, Kong LL, Zhang J, Li BS, Chen JH, Zhu J, Liu TH, Yin Y. Evaluation of the geometric accuracy of anatomic landmarks as surrogates for intrapulmonary tumors in image-guided radiotherapy. *Asian Pacific Journal of Cancer Prevention*, 2012. **13**(5):2393–2398.

[83] Ueno K, Shiga K, Morita S. A mathematical gift, II: the interplay between topology, functions, geometry, and algebra. Providence: American Mathematical Society, 2004.

[84] Nemoto K, Seiji K, Sasaki K, Kasamatsu N, Fujishima T, Ogawa Y, Ariga H, Takeda K, Kimura T, Yamada S. A novel support system for patient immobilization and transportation for daily computed tomographic localization of target prior to radiation therapy. *International Journal of Radiation Oncology • Biology • Physics*, 2003. **55**(4):1102–1108.

[85] Pascau J, Santos-Miranda J, González San-Segundo C, Illana C, Valdivieso M, García-Vazquez V, Marinetto E, Calvo F, Desco M. Intraoperative imaging in IOERT sarcoma treatment: initial experience in two clinical cases. *International Journal of Radiation Oncology • Biology • Physics*, 2011. **81**(2):S90.

[86] Siewerdsen JH. Cone-beam CT with a flat-panel detector: from image science to image-guided surgery. *Nuclear Instruments & Methods in Physics Research Section A: Accelerators, Spectrometers, Detectors and Associated Equipment*, 2011. **648**:S241–S250.

[87] Sorensen S, Mitschke M, Solberg T. Cone-beam CT using a mobile C-arm: a registration solution for IGRT with an optical tracking system. *Physics in Medicine and Biology*, 2007. **52**(12):3389–3404.

[88] Santos Miranda JA, Pascau J, Lardies MD, Desco M, Calvo F. Initial clinical experience of pencil beam dose modelling for intraoperative electron radiation therapy (IOERT). *Radiotherapy and Oncology*, 2011. **99**(Supplement 1):S246.

[89] Oshima T, Aoyama Y, Shimozato T, Sawaki M, Imai T, Ito Y, Obata Y, Tabushi K. An experimental attenuation plate to improve the dose distribution in intraoperative electron beam radiotherapy for breast cancer. *Physics in Medicine and Biology*, 2009. **54**(11):3491–3500.

[90] Rankin TM, Giovinco NA, Cucher DJ, Watts G, Hurwitz B, Armstrong DG. Three-dimensional printing surgical instruments: are we there yet? *Journal of Surgical Research*, 2014. **189**(2):193–197.

[91] López-Tarjuelo J, Bouché-Babiloni A, Santos-Serra A, Morillo-Macías V, Calvo FA, Kubyshin Y, Ferrer-Albiach C. Failure mode and effect analysis oriented to risk-reduction interventions in intraoperative electron radiation therapy: the specific impact of patient transportation, automation, and treatment planning availability. *Radiotherapy and Oncology*, 2014. **113**(2):283–289.

[92] Dries WJF, Koiter E, van 't Schip S, van den Berg H, van Riet Y. The Eindhoven intra operative radiotherapy applicator system for breast carcinoma. *8th International Conference of Intraoperative Radiotherapy*, 2014.

[93] Soriani A, Iaccarino G, Felici G, Ciccotelli A, Pinnarò P, Giordano C, Benassi M, D'Andrea M, Bellesi L, Strigari L. Development and optimization of a beam shaper device for a mobile dedicated IOERT accelerator. *Medical Physics*, 2012. **39**(10):6080–6089.

[94] García-Vázquez V, Marinetto E, Guerra P, Valdivieso-Casique MF, Calvo FA, Alvarado-Vásquez E, Sole CV, Vosburgh KG, Desco M, Pascau J. Assessment of intraoperative 3D imaging alternatives for IOERT dose estimation. *Zeitschrift für Medizinische Physik*, 2016. In press, corrected proof.

[95] Goswami SS, Ortuño Fisac JE, Wollny G, García-Vázquez V, Marinetto E, Santos Lleó A, Pascau J, Ledesma Carbayo MJ. A new workflow for image guided intraoperative radiotherapy using fluoroscopy based pose tracking. *International Journal of Computer Assisted Radiology and Surgery*, 2015. **10**(Supplement 1):S201–S203.

[96] Brudfors M, García-Vázquez V, Sesé-Lucio B, Marinetto E, Desco M, Pascau J. ConoSurf: open-source 3D scanning system based on a conoscopic holography device for acquiring surgical surfaces. *The International Journal of Medical Robotics and Computer Assisted Surgery*, 2016. Version of record online: 21 November 2016.

[97] Roeder F, Schramm O, Schwahofer A, Timke C, Habl G, Tanner M, Huber P, Debus J, Krempien R, Hensley F. Postplanning of a three-dimensional dose distribution for intraoperative electron radiation therapy (IOERT) using intraoperative C-arm based 3D-imaging: a phantom study. *International Journal of Computer Assisted Radiology and Surgery*, 2011. **99**(Supplement 1):S246–S247.

[98] Srinivasan K, Mohammadi M, Shepherd J. Applications of linac-mounted kilovoltage cone-beam computed tomography in modern radiation therapy: a review. *Polish Journal of Radiology*, 2014. **79**:181–193.

[99] Richter A, Hu Q, Steglich D, Baier K, Wilbert J, Guckenberger M, Flentje M. Investigation of the usability of conebeam CT data sets for dose calculation. *Radiation Oncology*, 2008. **3**:42.

[100] van Zijtvetd M, Dirkx M, Heijmen B. Correction of conebeam CT values using a planning CT for derivation of the "dose of the day". *Radiotherapy and Oncology*, 2007. **85**(2):195–200.

[101] Fotina I, Hopfgartner J, Stock M, Steininger T, Lüetgendorf-Caucig C, Georg D. Feasibility of CBCT-based dose calculation: comparative analysis of HU adjustment techniques. *Radiotherapy and Oncology*, 2012. **104**(2):249–256.

[102] Zhu L, Xie Y, Wang J, Xing L. Scatter correction for cone-beam CT in radiation therapy. *Medical Physics*, 2009. **36**(6):2258–2268.

[103] Lecchi M, Fossati P, Elisei F, Orecchia R, Lucignani G. Current concepts on imaging in radiotherapy. *European Journal of Nuclear Medicine and Molecular Imaging*, 2008. **35**(4):821–837.

[104] Mutic S, Palta JR, Butker EK, Das IJ, Huq MS, Loo LND, Salter BJ, McCollough CH, Van Dyk J. Quality assurance for computed-tomography simulators and the computed-tomography-simulation process: report of the AAPM radiation therapy committee task group no. 66. *Medical Physics*, 2003. **30**(10):2762–2792.

[105] Constantinou C, Harrington JC, Dewerd LA. An electron-density calibration phantom for CT-based treatment planning computers. *Medical Physics*, 1992. **19**(2):325–327.

[106] Salvat F, Fernandez-Varea JM, Sempau J. PENELOPE-2011: a code system for Monte Carlo simulation of electron and photon transport. *Proceedings of a Workshop/Training Course, OECD/NEA* 2011.

[107] Nobah A, Moftah B, Tomic N, Devic S. Influence of electron density spatial distribution and X-ray beam quality during CT simulation on dose calculation accuracy. *Journal of Applied Clinical Medical Physics*, 2011. **12**(3):80–89.

[108] De Vos W, Casselman J, Swennen GRJ. Cone-beam computerized tomography (CBCT) imaging of the oral and maxillofacial region: a systematic review of the literature. *International Journal of Oral and Maxillofacial Surgery*, 2009. **38**(6):609–625.

[109] Strobel N, Meissner O, Boese J, Brunner T, Heigl B, Hoheisel M, Lauritsch G, Nagel M, Pfister M, Rührnschopf EP, Scholz B, Schreiber B, Spahn M, Zellerhoff M, Klingenbeck-Regn K. Imaging with flat-detector C-arm systems. Editors: Reiser MF, Becker CR, Nikolaou K, Glazer G. *Multislice CT*. Berlin Heidelberg: Springer, 2009. 33–51.

[110] Mah P, Reeves TE, McDavid WD. Deriving hounsfield units using grey levels in cone beam computed tomography. *Dentomaxillofacial Radiology*, 2010. **39**(6):323–335.

[111] Oliveira ML, Tosoni GM, Lindsey DH, Mendoza K, Tetradis S, Mallya SM. Influence of anatomical location on CT numbers in cone beam computed tomography. *Oral Surgery, Oral Medicine, Oral Pathology and Oral Radiology*, 2013. **115**(4):558–564.

[112] Hatton J, McCurdy B, Greer PB. Cone beam computerized tomography: the effect of calibration of the hounsfield unit number to electron density on dose calculation accuracy for adaptive radiation therapy. *Physics in Medicine and Biology*, 2009. **54**(15):N329–N346.

[113] Ahn BS, Wu HG, Yoo SH, Park JM. Improvement of dose calculation accuracy on kV CBCT images with corrected electron density to CT number curve. *Journal of Radiation Protection and Research*, 2015. **40**(1):17–24.

[114] Elstrøm UV, Olsen SRK, Muren LP, Petersen JBB, Grau C. The impact of CBCT reconstruction and calibration for radiotherapy planning in the head and neck region – a phantom study. *Acta Oncologica*, 2014. **53**(8):1114–1124.

[115] Jaju PP, Jain M, Singh A, Gupta A. Artefacts in cone beam CT. *Open Journal of Stomatology*, 2013. **3**:292–297.

[116] Parsa A, Ibrahim N, Hassan B, Motroni A, van der Stelt P, Wismeijer D. Influence of cone beam CT scanning parameters on grey value measurements at an implant site. *Dentomaxillofacial Radiology*, 2013. **42**(3):79884780.

[117] Rong Y, Smilowitz J, Tewatia D, Tomé WA, Paliwal B. Dose calculation on kV cone beam CT images: an investigation of the HU-density conversion stability and dose accuracy using the site-specific calibration. *Medical Dosimetry*, 2010. **35**(3):195–207.

[118] Takemura A, Tanabe S, Tokai M, Ueda S, Noto K, Isomura N, Kojima H. Long-term stability of the Hounsfield unit to electron density calibration curve in cone-beam computed tomography images for adaptive radiotherapy treatment planning. *Journal of Radiotherapy in Practice*, 2015. **14**(4):410–417.

[119] Yadav P, Ramasubramanian V, Paliwal BR. Feasibility study on effect and stability of adaptive radiotherapy on kilovoltage cone beam CT. *Radiology and Oncology*, 2011. **45**(3):220–226.

[120] Marinetto E, García-Vázquez V, Santos-Miranda JA, Calvo FA, Desco M, Pascau J. Image-guided intraoperative electron irradiation: clinical set-up and feasibility. *8th International Conference of Intraoperative Radiotherapy*, 2014.

[121] Portalés C, Gimeno J, Vera L, Fernández M. Towards a guidance system to aid in the dosimetry calculation of intraoperative electron radiation therapy. *Journal of Imaging*, 2015. **1**(1):180–192.